Title: How respiratory complexes and ATP synthase co-assemble to build cristae

Authors: Mengchen Wu[1]†, Zhongqiu Li[2]†, Zhuru Hou[3]†, Hongtao Tian[1], Ruizhe Zhang[1], Fangzhu Han[1], Yiqi Hu[1], Jiancang Zhou[4], Shizhu Li[2], Alexey Amunts[5,6]*, Yue Liu[3]*, Long Zhou[1]*

Affiliations:

[1]Department of Biophysics and Department of Critical Care Medicine of Sir Run Run Shaw Hospital, Zhejiang University School of Medicine, Hangzhou, China.
[2]National Institute of Parasitic Diseases, Chinese Center for Disease Control and Prevention (Chinese Center for Tropical Diseases Research); NHC Key Laboratory of Parasite and Vector Biology, National Key Laboratory of Intelligent Tracking and Forecasting for Infectious Diseases, Shanghai, China.
[3]Department of Microbiology and State Key Laboratory for Diagnosis and Treatment of Infectious Diseases of the First Affiliated Hospital, Zhejiang University School of Medicine, Hangzhou, China.
[4]Department of Critical Care Medicine of Sir Run Run Shaw Hospital, Zhejiang University School of Medicine, Hangzhou, China.
[5]University of Münster, Schlossplatz 8, Münster, Germany.
[6]Institute of Bio-Architecture and Bio-Interactions, Shenzhen Medical Academy of Research and Translation, Shenzhen, Guangdong, China.

*Corresponding author. Email: alexey.amunts@gmail.com, yuel@zju.edu.cn, longzhou@zju.edu.cn
†These authors contributed equally to this work.

Abstract:

Mitochondrial oxidative phosphorylation (OXPHOS) is often organized into spatially segregated domains, with ATP synthase (complex V, CV) oligomers shaping highly curved cristae rims and respiratory chain complexes I-IV (CI-CIV) occupying flatter membrane regions[1,2]. Building on our recent identification of a *bona fide* ETC-ATP synthase supercomplex (see accompanying manuscript), here we determine how such assemblies are deployed into long-range, periodic OXPHOS arrays on native membranes. By integrating cryo-electron microscopy (cryo-EM) and cryo-electron tomography (cryo-ET),

we resolve multiple CIICIV$_2$CV-based supercomplexes that act as endcaps for ATP synthase dimer (CV$_2$) rows from the mitochondria of the kinetoplastid parasite *Leishmania tarentolae*. We show that repeating units of endcapped-rows stack with defined registers to tile the discoidal cristae rim, establishing a membrane-scale architectural program that couples respiratory-chain organization to cristae morphology. Subtomogram averaging validates these assemblies *in situ* and reveals their characteristic orientation and spacing on the crista rim. Together, these data extend the CIICIV$_2$CV framework from molecular mechanism to mesoscale architecture and suggest that kinetoplastids achieve stable discoidal cristae by constraining ATP synthase row growth through CIICIV$_2$CV-mediated endcapping and ordered packing.

Main Text:

The OXPHOS system converts redox energy into ATP through a membrane-based circuit in which the electron transport chain (ETC) generates a proton motive force (PMF)[3,4] and the ATP synthase consumes it[5,6]. A recurring organizational theme across eukaryotes is spatial patterning on the cristae membrane[1]: ATP synthase dimers (CV$_2$) and their higher-order rows accumulate at regions of high curvature, most prominently along cristae rims, where they contribute directly to membrane bending[7–16], whereas ETC CI-CIV and their supercomplexes tend to populate flatter membrane regions and are often viewed as laterally mobile assemblies[2,17–25]. This arrangement provides an intuitive physical complement to Mitchell's chemiosmotic concept, in which boundary conditions and membrane geometry help shape and confine the proton circuit[26–29].

However, this canonical picture also leaves fundamental gaps. If ATP synthase oligomers sculpt cristae rims while the respiratory chain supplies protons from elsewhere, how are the sources and sinks of the proton circuit coordinated at the membrane scale? A wealth of functional and computational studies have suggested the kinetic advantages of keeping the PMF generator and consumer in spatial proximity to encourage the establishment of lateral

proton gradient and near-membrane proton diffusion[30–36]. Moreover, it remains elusive that whether ETC complexes can directly participate in long-range crista architecture rather than acting as diffuse, independent modules. Biochemical observations have hinted that ETC components can form higher-order clusters or "respiratory strings/patches" in specific lineages[37–41]. More recent *in situ* studies suggested stacked respiratory assemblies in species with tubular cristae, including mammals and ciliates[14,22,42,43]. In parallel, transient co-localization of respirasomes alongside ATP synthase rows was also reported in mammalian mitochondria[25,44]. However, these models either remain structure-based conjectures or reflect dynamic juxtaposition of stable modules, yet a definitive structural description of long-range, periodic OXPHOS arrays integrating ATP synthase with respiratory-chain assemblies has been missing.

In our companion work in *Trypanosoma brucei*, we establish a *bona fide* ETC-ATP synthase supercomplex, CIICIV$_2$CV, and define its mechanistic basis for assembly: a kinetoplastid-specific module repurposes the ATP synthase dimerization interface to accommodate the dimeric cytochrome *c* oxidase, CIV$_2$, without sterically compromising rotary catalysis (see accompanying manuscript). Disrupting this linkage remodels discoidal cristae and reduces maximal polarization capacity, implicating CIICIV$_2$CV as an architectural constraint that safeguards cristae integrity and bioenergetic reserve. These findings raise the next question: how is this co-assembly based ETC-ATP synthase coupling deployed *in situ* to build the long-range organization characteristic of kinetoplastid cristae?

Here, we address this architectural layer in the related kinetoplastid *Leishmania tarentolae*[45], a non-pathogenic model for the Leishmania genus[46]. Combining single particle cryo-EM with cryo-ET and subtomogram averaging (STA), we resolve multiple ETC-CV assemblies centered on the CIICIV$_2$CV supercomplex and determine how they integrate with ATP synthase rows on native membranes. We show that CIICIV$_2$CV serves as an endcap for short CV$_2$ rows and that repeating endcapped-row units pack with defined registers to tile the

discoidal cristae rim. By linking atomic interfaces to mesoscale packing rules and *in situ* membrane architecture, our work extends the ETC-ATP synthase framework to long-range OXPHOS arrays, thereby providing a structural blueprint for the intricate tripartite relationship of OXPHOS supramolecular organization, crista morphology and mitochondrial energy metabolism.

Purification and cryo-EM structure determination of ETC-CV supercomplexes

Digitonin-solubilized mitochondrial membrane proteins of the wild-type (WT) *L. tarentolae* promastigotes were purified by sequential anion exchange and size-exclusion chromatography, yielding multiple high-molecular-weight assemblies with both CIV and CV activities (Supplementary Fig. 1). To examine whether $CIII_2$ is integrated into these OXPHOS supercomplexes, we additionally generated a C-terminal Strep-tagged copy of the conserved $CIII_2$ subunit mitochondrial processing peptidase α (MPPα/UQCRC2), enabling affinity purification of $CIII_2$ and associated assemblies (Supplementary Fig. 2). The obtained complexes displayed CIV activity but no detectable CV activity, indicating that $CIII_2$ forms supercomplexes with CIV, but not CV. In both purification schemes, the highest molecular weight fractions were selected for cryo-EM data collection (Supplementary Figs. 1 and 2, Supplementary Tables 1 and 2).

Cryo-EM classification of particles from the WT dataset revealed three well-resolved ETC-CV assemblies: $CII_2CIV_2CV_2$, the $CIICIV_2CV_3$ and the $CII_2CIV_4CV_{10}$ (Extended Data Fig. 1 and 2a, Supplementary Tables 1 and 3 and Supplementary Video 1). The C2-symmetric $CII_2CIV_2CV_2$ map reached the highest overall resolution of 2.7 - 4.7 Å (Extended Data Fig. 2a and 3c). $CIICIV_2CV_3$ comprises one $CIICIV_2CV$ ETC-ATP synthase supercomplex plus one ATP synthase dimer (CV_2). It corresponds to a subassembly of the larger, again C2 symmetric $CII_2CIV_4CV_{10}$ with each asymmetric unit containing one $CIICIV_2CV$ and two CV_2 copies (Fig. 1a,b). Refinement of the $CIICIV_2CV_3$ achieved 2.9 - 3.9 Å resolution for most regions, with lower local resolution in the rotationally flexible *c*-ring and peripheral

stalk (PS) of CV (Extended Data Fig. 1a and 3a). The $CII_2CIV_4CV_{10}$ reconstructions reached 2.9 Å to 5.5 Å and displayed modest anisotropy (Extended Data Fig. 1b and 3b). In the $CIII_2$ affinity dataset, classification yielded two oligomeric states, namely $(CIII_2)_2$ and $(CIII_2)_4$, with local resolutions of 2.6 - 4.3 Å (Extended Data Fig. 2b and 3d,e, Supplementary Tables 2 and 4 and Supplementary Video 2).

Architectures of the three types of ETC-CV supercomplexes

The above cryo-EM structures confirm the existence of $CIICIV_2CV$, a stoichiometrically defined supercomplex that integrates ETC complexes with ATP synthase (see accompanying manuscript). They further reveal how higher order OXPHOS assemblies are organized at the rim of discoidal cristae (Fig. 1, Extended Data Fig. 4 and Supplementary Video 1). First, the CV_4 portion within $CII_2CIV_4CV_{10}$ represents a structural depiction of how CV_2 dimers associate laterally to form short, left-handed helical CV_2 rows, as proposed for euglenid mitochondria[16]. In this arrangement, the F_1 headpiece of the preceding CV_2 dimer wedges into the V-shaped inter-F_1 cleft of the succeeding CV_2, generating a ~33° rotational offset between adjacent dimers, resembling a fanned deck of cards (Fig. 1a). Notably, the resulting CV_4 architecture fits well into the *in situ* cryo-ET map from *T. brucei*[16], supporting the previously proposed left-handed helix model of kinetoplastid/euglenid CV oligomerization[47] (Extended Data Fig. 4a,b).

More importantly, the $CIICIV_2CV_3$ and $CII_2CIV_4CV_{10}$ structures demonstrate how the primary ETC-CV assembly, $CIICIV_2CV$, associates with a CV_2 row. $CIICIV_2CV$ docks its monomeric CV into the inter-protomer space of an endmost CV_2 unit, using the same geometric principle by which two CV_2 dimers interact within CV_4 tetramer (Fig. 1a,b). This interaction is supported on the side of the monomeric CV and the adjacent CIV protomer (CIV_P hereafter), whereas the opposite end of $CIICIVCV_2$ formed by CII and the distal CIV protomer (CIV_D) does not support addition of another CV_2 unit (Fig. 1b). Thus, $CIICIV_2CV$ function as an endpiece that defines row termini. Together with our previous study (see

accompanying manuscript), these data support a model in which CII_2CIV_2CV endpieces constrain CV_2-row growth and thereby prevent uncontrolled membrane bending that would otherwise drive discoidal rims toward self-enclosed tubular morphologies (Extended Data Fig. 4c).

In $CII_2CIV_4CV_{10}$, two closely interacting $CIICIV_2CV_5$ asymmetric units correspond to fragments of two adjacent $CIICIV_2CV$-capped CV_2 rows. This indicates that unlike *T. brucei*[16], *L. tarentolae* packs its CV_2 rows densely with little free membrane space between neighboring rows (Fig. 1a and Extended Data Fig. 4d). When viewed azimuthally along the crista circumference, the continuous membrane surface of $CII_2CIV_4CV_{10}$ spans ~130° of curvature (Fig. 1a). A curvature gradient is evident: strong bending is concentrated in the CV_2 multimer region, whereas the flanking $CIICIV_2CV$ endpieces exhibit shallower curvature. This organization is consistent with $CIICIV_2CV$ endpieces terminating both CV_2 row growth and locally excessive curvature at the crista rim. Viewed perpendicular to the discoid plane, a modest curvature of ~45° is observed, corresponding to an estimated crista radius of ~600 Å (Extended Data Fig. 4e).

Lastly, the C2-symmetric $CII_2CIV_2CV_2$ structure shows that CIV_2 serves as the central coupler to connect two CIICV modules (Fig. 1c). This is reflected by two copies of the kinetoplastid-specific CII linkage domain, which connect CII to the adjacent CIV protomer on the matrix side (see accompanying manuscript). Viewed parallel to the inner mitochondrial membrane (IMM), the central CII_2CIV_2 region is nearly flat, while the two flanking monomeric CVs each impose ~36° curvature (Fig. 1c). How this assembly integrates into the tightly stacked, $CIICIV_2CV$-capped CV_2 rows defined by $CII_2CIV_4CV_{10}$ remains clear. One possibility is that $CII_2CIV_2CV_2$ extends the $CIICIV_2CV$ endpiece by adding an additional CIICIV module, thereby stabilizing the arch-like rim of the discoidal cristae (Extended Data Fig. 4f). Alternatively, it may cap two neighbouring CV_2 rows simultaneously via its two

CIICIVCV asymmetric units, providing a mechanism to accommodate local curvature fluctuations in the crista membrane.

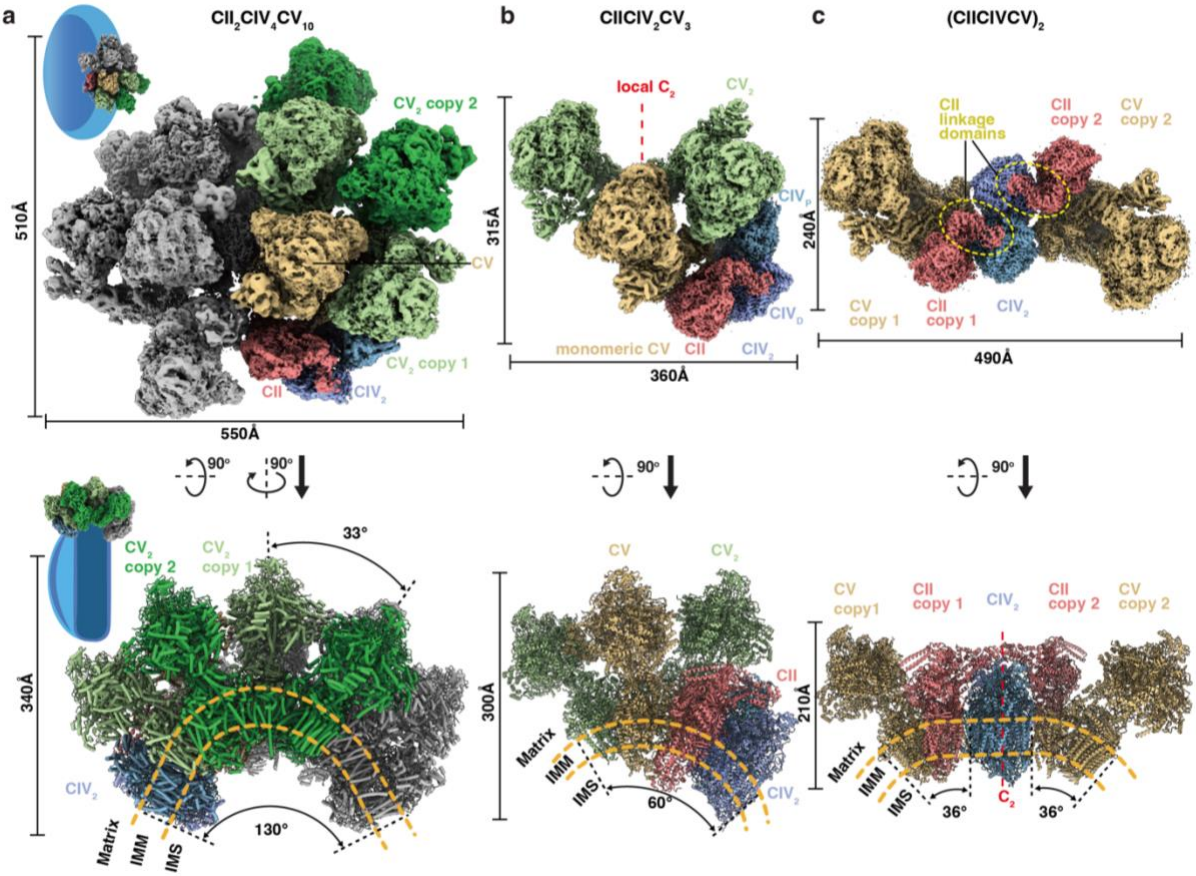

Fig. 1 | Overall architectures of the supercomplexes $CII_2CIV_4CV_{10}$, $CIICIV_2CV_3$ and $CII_2CIV_2CV_2$. a-c, Cryo-EM density maps (top panels) and structural models (bottom panels) of the supercomplexes $CII_2CIV_4CV_{10}$ (**a**), $CIICIV_2CV_3$ (**b**) and $CII_2CIV_2CV_2$ (**c**). The maps and models are viewed perpendicular and parallel to the IMM, respectively. The supercomplexes are colored by individual complexes, except for (**a**) where only one asymmetric unit of $CIICIV_2CV_5$ is colored for clarity. Dimensions of and membrane curvatures (dashed orange curves) adapting to the supercomplexes are labeled. The CII linkage domains are circled (yellow dashes) and labelled in (**c**). Note that structural model of the supercomplex $CII_2CIV_4CV_{10}$ is shown as cylindrical cartoons to reflect its resolutions.

Spatial register between adjacent CV_2 rows is manifested by PS-PS pairing

Dimerization of two $CIICIV_2CV_5$ fragments within the $CII_2CIV_4CV_{10}$ supercomplex demonstrates how adjacent $CIICIV_2CV$-capped CV_2 rows are positioned relative to one another and how they interact laterally (Fig. 2a). Notably, the interfacial ATP synthase complexes, either CV_2 units within a row or the monomeric CVs within $CIICIV_2CV$

192 endpieces, pair via the interaction between the tips of their peripheral stalks. This repeating
193 pairing pattern defines the spatial register between tightly packed rows. In the arrangement
194 captured by $CII_2CIV_4CV_{10}$, three PS-PS pairs are formed between the two asymmetric units,
195 which represent fragments of two adjacent capped rows (Fig. 2a). We refer to this
196 configuration as a '+3 register'. Specifically, the central PS-PS pair denotes CV_2-CV_2
197 interaction, whereas the two flanking pairs link an internal CV_2 unit in one row to a
198 $CIICIV_2CV$ endpiece in the neighbouring row, thereby marking the two ends of the inter-row
199 overlap. Whether the +3 register represents the prevalent packing mode on *L. tarentolae*
200 cristae will be resolved by *in-situ* structural investigations (see below).
201
202 At higher resolution, the $CIICIV_2CV_3$ structure visualizes multiple interfaces, both within the
203 $CIICIV_2CV$ endpiece and at its junction with the CV_2 row (Fig. 1b). Within $CIICIV_2CV$, the
204 most prominent inter-complex interface is formed between the monomeric CV and the CIV_P
205 protomer. In canonical ATP synthase dimers, this same topological region is organized around
206 the $(e/g)_2$ module found at the dimer center, which links the two protomers (Fig. 2b). In
207 $CIICIV_2CV$, this dimerization module is repurposed to connect CV to CIV by replacing the
208 canonical subunit *g* pair with two structurally homologous, kinetoplastid-conserved
209 paralogues *g'* and *g''* (see accompanying manuscript). The resulting *e*/*g'*/*e*/*g''* module
210 preserves the overall interlocking architecture of the $(e/g)_2$ scaffold while specifying
211 assembly of $CIICIV_2CV$ (Fig. 2b).
212
213 The *e*/*g'*/*e*/*g''* module also contributes to the binding of $CIICIV_2CV$ onto CV_2 by forming
214 hydrophobic interactions with the adjacent subunit *c* within the CIV_P-facing *c*-ring of CV_2
215 (Fig. 2b,d). Together with additional contacts, these transient hydrophobic interfaces between
216 the rotating *c*-ring and neighboring stationary membrane components provide major cohesive
217 forces within $CIICIV_2CV_3$. For example, from COX5C of CIV_P and the adjacent *c* subunit of
218 CV_2 form an interdigitated, multi-layer π-π stack (Fig. 2c). As the *c*-ring rotates, this zipper-
219 like π-π stack is expected to break and reforms subsequently as one *c* subunit moves away

and the next approaches, allowing stable association without sterically compromising rotary catalysis.

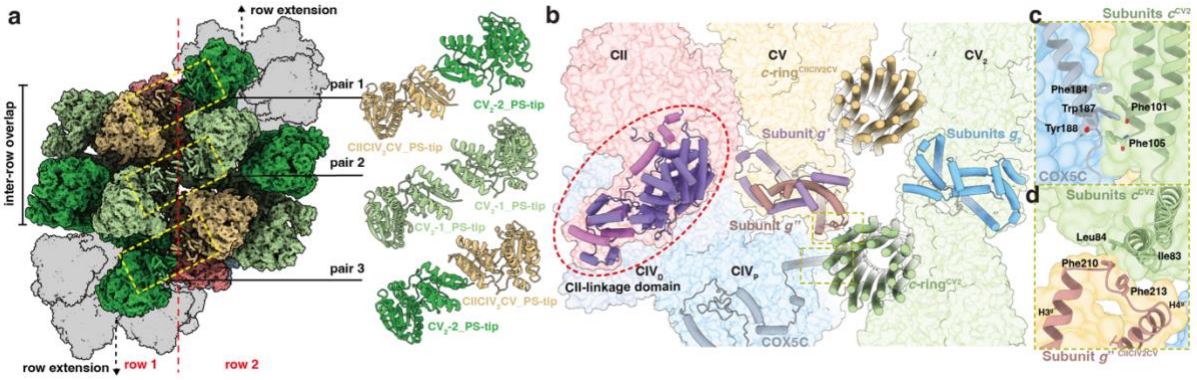

Fig. 2 | Spatial registers and interactions within the ETC-CV supercomplexes. a, The two asymmetric units of $CIICIV_2CV_5$ within $CII_2CIV_4CV_{10}$ represent neighbouring $CIICIV_2CV$-capped CV_2 rows, with respective extending directions labelled. The overlapping region and the interface between rows is mediated by three pairs of PS tip-PS tip interactions (yellow rectangles in left panel and zoom-in views in right panel). The two flanking PS-PS pairs 1 and 3 are from CVs of CV_2 (dark green) and $CIICIV_2CV$ (sand), while the central PS-PS pair 2 is from adjacent CVs of two CV_2 units (light green). **b**, An overview of the interfaces in $CIICIV_2CV_3$, viewed perpendicular to IMM. The interacting subunits are shown as cylindrical cartoons, including the interlocking *g'* (lavender) and *g''* (salmon) between CIV_P and CV, the canonical *g*/*g* (blue) module within CV_2 and the CII linkage domain (purple and orchid) connecting CII and CIV_D (red circle). In addition, subunits *g''* of CV and COX5C (gray) of CIV_P interact hydrophobically with the CIV_P-facing *c*-ring (light green) of CV_2. **c**, Zoom-in view of the COX5C-subunit *c* interaction, showing the multi-layer π-π stack formed by several nearby aromatic residues. **d**, Zoom-in view of the *g''*-subunit *c* interaction. Key residues are shown as sticks.

Cryo-ET validates in situ $CIICIV_2CV_3$ and its end-of-row association

To avoid potential detergent-induced destabilization and to visualize long-range OXPHOS organization in a native lipid environment, we imaged mitochondrial cristae directly by cryo-ET (Extended Data Fig. 5, Supplementary Table 5 and Supplementary Video 3). Because ATP synthase was the only membrane-embedded complex readily visible in the reconstructed tomograms, we performed Cryo-EM derived template matching to detect ATP synthase particles (Fig. 3a). Initial STA revealed a recurrent cluster of three F_1 headpieces, two corresponding to a CV_2 and a third CV positioned between them (Extended Data Fig. 5). At this stage, the absence of clearly resolved additional density next to the third CV left two

plausible interpretations: either a second CV_2 (i.e. CV_4) or a $CIICIV_2CV$ associated with a CV_2 unit (i.e. $CIICIV_2CV_3$).

To distinguish these alternatives, we performed subtomogram classification using a mask targeting the region expected to contain $CIICIV_2$. This analysis identified a minor $CIICIV_2CV_3$ class, distinguished from CV_4 by the presence of the characteristic CII linkage density connecting CII to the distal protomer CIV_D (see accompanying manuscript). Further rounds of classification and refinement yielded a $CIICIV_2CV_3$ reconstruction at ~21 Å overall resolution, in which major features, including the CII linkage domain, the CIV_2 dimer, the $\alpha_3\beta_3$ headpiece, and the central and peripheral stalks of ATP synthase clearly discernable (Fig. 3b and Extended Data Fig. 5). In parallel, the more abundant CV_4 class was refined to ~17 Å resolution (Fig. 3d and Extended Data Fig. 5).

The $CIICIV_2CV_3$ map thus confirms that CII and CIV can assemble with ATP synthase into a structurally defined $CIICIV_2CV$-based supercomplex *in situ*, and that this endpiece associates with a CV_2 unit at the crista rim (Fig. 3b and Supplementary Video 4). Although α-helices are not resolved at this resolution, the cryo-EM structures of $CIICIV_2CV_3$ and CV_4 fit the corresponding cryo-ET densities as rigid bodies with good map-model correlations (Fig. 3b,d, Supplementary Video 4 and Supplementary Table 5). Both STA reconstructions contain clear membrane density, allowing us to compare local membrane curvature associated with different modules. Consistent with ATP synthase being the dominant curvature generator, the membrane underlying the CV-multimer region is strongly bent (~41° per CV dimer), whereas the membrane adjacent to the $CIICIV_2$ region of $CIICIV_2CV_3$ is comparatively flat (Fig. 3b,d,c and Extended Data Fig. 5). Quantification across subtomograms supports this divergence in curvature between $CIICIV_2$-proximal membrane and CV_2-proximal membrane (Fig. 3c). Importantly, the *in situ* maps also define preferred orientations of both $CIICIV_2CV_3$ and CV_4: in both assemblies, the long axis of the CV_2 unit(s) aligned nearly perpendicularly

to the circumference of the discoidal cristae (Fig. 3b,d). This shared geometric alignment is compatible with further lateral packing into larger arrays along the crista edge.

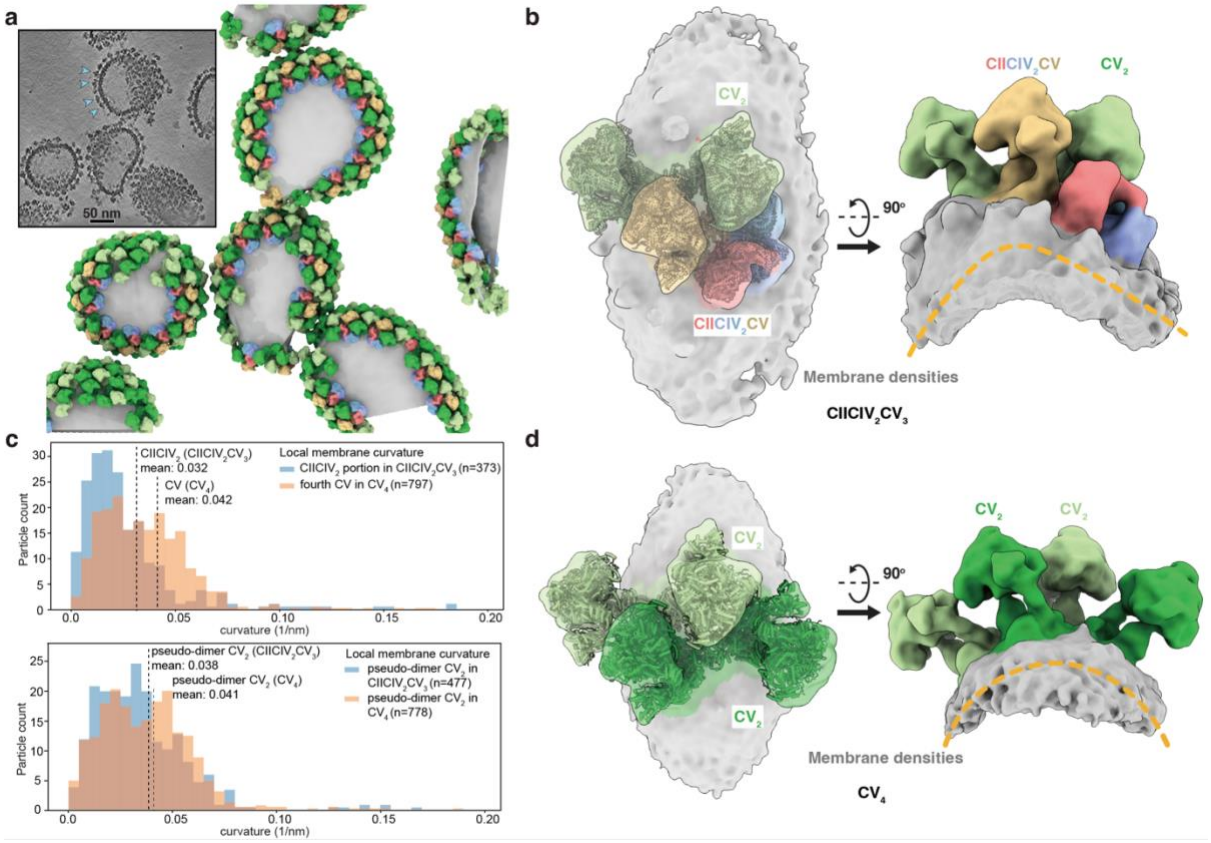

Fig. 3 | Cryo-ET structures of the supercomplexes CIICIV$_2$CV$_3$ and CV$_4$. a, Tomographic slice (inserted panel, CV marked by arrows) and membrane segmentation (gray surfaces) of the same tomogram with STA maps mapped back to their particle positions. Complex maps, shown as surfaces, are colored as in Fig. 1. Alternating CV$_2$ units are colored dark and light greens. **b**,**d**, STA maps of supercomplexes CIICIV$_2$CV$_3$ (**b**) and CV$_4$ (**d**), viewed perpendicular (left panels) or parallel (right panels) to IMM. The cryo-EM structures of CIICIV$_2$CV$_3$ and the CV$_4$ portion of the CII$_2$CIV$_4$CV$_{10}$ are docked into respective STA maps. The membrane densities (gray) are traced by orange dashes. **c**, Distributions of local membrane curvatures of CIICIV$_2$CV$_3$ (slate) and CV$_4$ (sand). Curvatures were quantified at the mass centers of the shared CV2 pseudo-dimer in both assemblies (top panel), or at the mass center of the CIICIV$_2$ portion in CIICIV$_2$CV$_3$ and of the positionally equivalent fourth CV in CV$_4$ (bottom panel). Data points are binned by 0.005 nm^{-1}. Statistical means and subtomogram numbers (n) are labelled. Curvature calculation was based on seven typical tomograms where the cristae integrity is best preserved during sample preparation. CIICIV$_2$ are found at less curved positions than CV$_4$.

CIICIV$_2$CV endpieces define a periodic belt at the discoidal crista rim

Mapping the averaged subtomograms of $CII_2CIV_2CV_3$ and CV_4 back onto segmented cristae membranes enabled visualization of the long-range OXPHOS architecture on kinetoplastid mitochondria (Figs. 3a and 4a and Supplementary Video 3). The most frequently observed configuration consists of two CII_2CIV_2CV endpieces flanking a short row of four CV_2 dimers, forming a $(CII_2CIV_2CV)_2(CV_2)_4$ unit that spans 182° of membrane curvature when viewed azimuthally (Fig. 4c). The long axis of the CV_2 row intersects the circumference at an angle of 49° (Fig. 4b). Multiple copies of this repeat unit pack laterally through PS tips, such that four PS-PS pairs are kept with the inter-row overlap and one unpaired PS remains as the offset between adjacent units, defining a +4 register (Fig. 4d). Repetition of this packing rule generates a belt-like assembly that wraps around the cristae circumference to form a discoid of ~1,200 Å diameter and ~260 Å thickness (Fig. 4a). The bulged crista rim displays a curvature radius of 130 Å, while the central regions of the two discoidal faces appear comparatively flat (Fig. 4a,b). Overall, alignment of $(CII_2CIV_2CV)_2(CV_2)_4$ units in a +4 register represents the prevalent long-range organization in our tomograms and yields dimensions consistent with prior morphological estimates[48] (see accompanying manuscript). The resultant dense packing of CV F_1 headpieces, also reported for several green algae[2,13], suggests the potential for mechanical coupling between the rotary catalysis of neighboring ATP synthase complexes, although this will require direct functional testing.

While the +4 register dominates *in situ*, we also detected less frequent deviations. The purified $CII_2CIV_4CV_{10}$ assembly adopts a +3 register (Fig. 2a), which does not conform to the prevalent +4 periodicity. Consistently, inspection of our tomograms identified alternative configurations in which the number of CV_2 dimers between two CII_2CIV_2CV endpieces varies, producing $(CII_2CIV_2CV)_2(CV_2)_n$ assemblies with n=1-3 in addition to the dominant n=4 (Extended Data Fig. 6a). We also observed +3 and +2 registers *in situ* (Extended Data Fig. 6a-c), indicating that the +3 register captured in $CII_2CIV_4CV_{10}$ reflects a genuine, albeit less frequent, native packing mode rather than a purification artifact. Unlike the dominant +4 organization, these minor registers do not extend into long-range periodic order. Instead, they

appear to act locally as defects that disrupt +4 periodicity, accommodating gradients or fluctuations in rim curvature (Extended Data Fig. 6d). For example, within a cluster of four CV_2 rows, we observed a transition from +3 to +4 register accompanied by the gradual emergence of the unpaired PS offset as the rim locally flattens. Thus, deviations from the dominant register likely provide a geometrical accommodation mechanism within the otherwise perfectly periodic belt (Extended Data Fig. 6d,f).

It's worth noting that we did not detect CV_2 row longer than $(CIICIV_2CV)_2(CV_2)_4$ in our tomograms. Consistent with this limit, an artificial $(CIICIV_2CV)_2(CV_2)_5$ model aligned on +4 register produces severe steric clashes between the two $CIICIV_2CV$ endpieces and the terminal CV_2 unit (Extended Data Fig. 6e). In other words, in the dominant architecture there is always a one-PS offset between adjacent rows (Fig. 4d), which constrains both row length and permissible inter-row register. Geometrically, extending overlap beyond these constraints either by longer rows aligned in +4 register, or by mis-registering $(CIICIV_2CV)_2(CV_2)_4$ units would yield rim curvature exceeding 180° (Extended Data Fig. 6g), which is incompatible with a flat-faced discoid and would instead favor alternative morphologies, such as the biconcave cristae described in *Euglena gracilis*[23].

Comparison with *T. brucei* highlights an alternative solution within the same architectural framework. *In situ* analysis of *T. brucei* discoidal cristae reported CV_2 rows containing up to six dimers[16]. Unlike *L. tarentolae*, these rows are more loosely packed, leaving substantial free membrane space between neighboring rows and thereby reducing the need for a well-defined inter-row register (Fig. 5a,b). This open arrangement likely relaxes steric constrains and allows longer rows to adjust posture while preserving flat discoidal faces. Therefore, *L. tarentolae* and *T. brucei* appear to achieve the same morphological outcome through distinct mesoscale strategies: the former through tight packing with strict register/length constraints, and the latter through looser packing that permits autonomous local adaptation. This is contrasted by *E. gracilis*, where the presence of canonical CI and respirasomes has been

proposed to impose the negative membrane curvature, consistent with its biconcave cristae morphology among other discobids[23,49] (Fig. 5c).

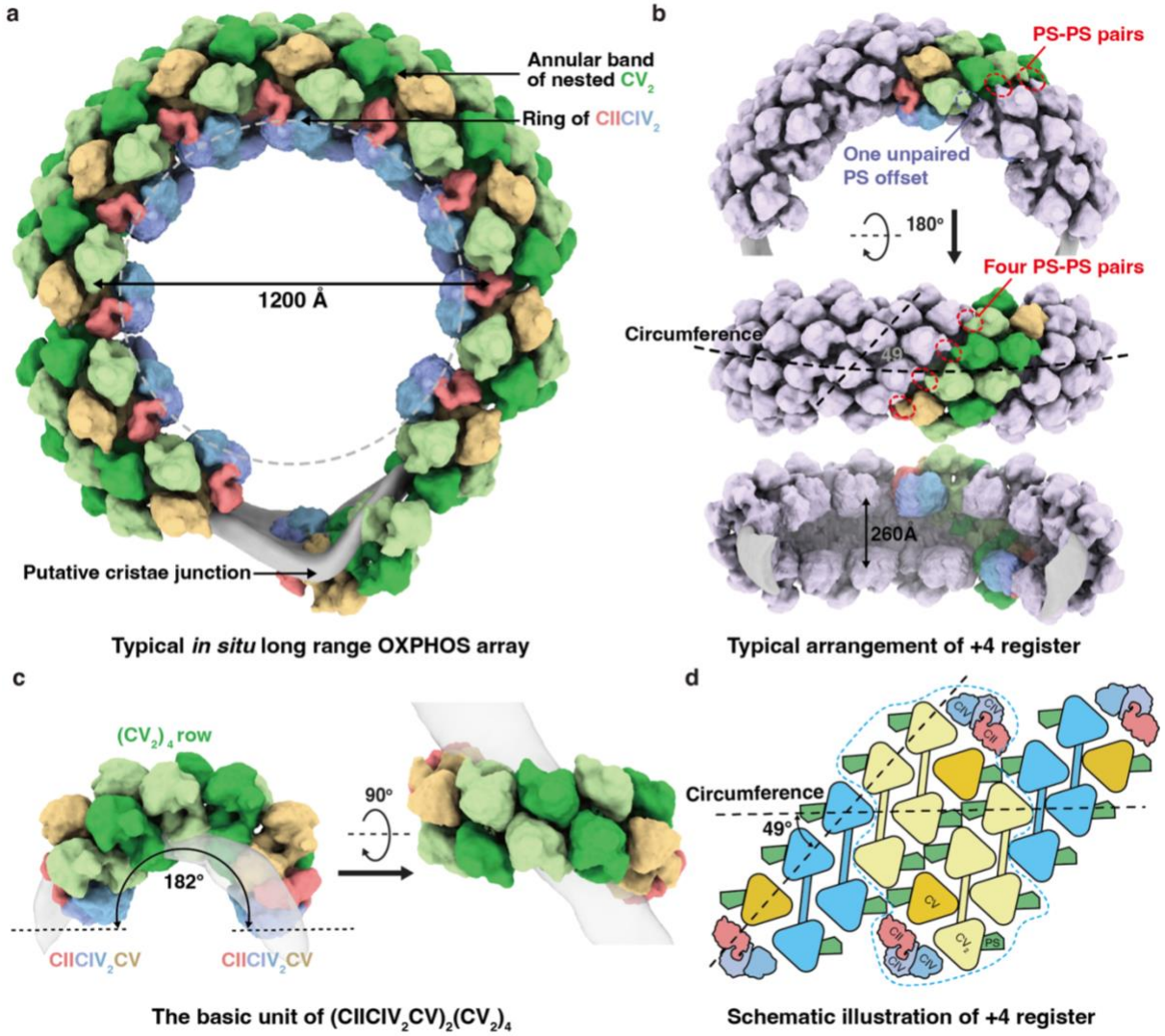

Fig. 4 | Structures of the long-range OXPHOS arrays *in situ*. **a**, A typical discoidal crista nearly fully tiled by the most common pattern of long-range OXPHOS arrays. The estimated cristae diameter and the position of putative cristae junction are labelled. **b**, Architectural details of the +4 register with one unit of the $(CIICIV_2CV)_2(CV_2)_4$ assembly colored as in Fig. 1, with the remaining units colored gray. Structures are shown in three orientations: perpendicular-to-discoid, parallel-to-discoid and from the cristae lumen. The register-defining PS-PS pairs (red dash) and unpaired PS offsets (blue dash) are circled. Intersection of $(CIICIV_2CV)_2(CV_2)_4$ and the circumferential line of cristae discoid and the discoid thickness are labelled. **c**, The basic repetitive unit of $(CIICIV_2CV)_2(CV_2)_4$ in two viewing directions with its curvature span labelled (left panel). Cristae membrane is shown as transparent gray surface. **d**, Cartoon representation of the +4 register. The 49° angle between individual CV_2 row and discoidal cristae circumference line is labelled. $CIICIV_2CV$, CV_2 and the register-defining PS-PS pairs are also labelled.

Discussion

ATP synthase dimerization and multimerization into higher-order rows are a conserved driver of cristae curvature and in many systems this has supported the view that cristae rims are shaped primarily by CV_2 oligomers[1,8,11–13,15,16,50–53]. What has remained unresolved is how the respiratory chain is integrated into membrane scale architecture in lineages such as the euglenids with discoidal cristae. In our recent study in *T. brucei*, we establish a *bona fide* ETC-ATP synthase supercomplex with a repurposed dimerization interface and suggest its role in safeguarding the discoidal shaped cristae (see accompanying manuscript). The present work extends that mechanistic framework to the mesoscale: in *L. tarentolae*, we resolve how $CIICIV_2CV$-based endpieces are deployed *in situ* to build long-range, periodic OXPHOS arrays that tile the discoidal crista rim.

This organization has immediate bioenergetic implications. It fixes the lateral spacing and relative orientation of proton sources (ETC) and sinks (ATP synthase), creating a geometry that can enrich and compartmentalize PMF at the rim[34–36,51]. In this view, cristae morphology is not a by-product of OXPHOS packing, it is part of the design principle that supports robust coupling and bioenergetic reserve[28,54,55]. First of all, the long-range ordered arrangement of OXPHOS complexes can ensure maximal utilization of the available surface of cristae, whose invagination from the inner boundary membrane (IBM) increases OXPHOS-covered area in the first place[54]. In *L. tarentolae* mitochondria, when OXPHOS arrangement deviates from the regular pattern, such as where the +3 register-representing $CII_2CIV_4CV_{10}$ supercomplex appears, densities of surrounding CV_2, CIV_2 and CII decrease due to this disruption (Extended Data Fig. 6c,d). It is conceivable that if the $CIICIV_2CV$ endpiece is knocked out and uncontrolled extensions of CV_2 rows re-shape discoidal cristae into the aberrant tubular form, its uniform high membrane curvature would dismiss flat membrane dwellers such as the ETC complexes, thereby decreasing their total expressions (see accompanying manuscript) (Extended Data Fig. 4c). Together, these data establish a multi-scale principle: a lineage-specific molecular interface builds an ETC-ATP synthase

supercomplex, and that supercomplex is then re-used as an architectural module to impose row boundaries and thereby stabilize a particular crista geometry.

Why do these OXPHOS arrays place ATP synthase at the tightest curvature, while positioning respiratory modules nearby but off the sharpest bend? A gradual curvature decrease is observed from the circumferential CV_2 multimers to the transitional $CIICIV_2CV$, then to the central $CIII_2$ oligomers and/or supercomplexes (Fig. 5d and Extended Data Fig. 7). Our structures suggest a practical answer: beyond the endpiece itself, the long-range packing rules revealed for *L. tarentolae* convert local interfaces into a membrane-scale lattice. The discoidal rim is tiled by repeating units in which short CV_2 rows are flanked by $CIICIV_2CV$ endpieces, and these units pack with defined registers, effectively a periodic 'tiling grammar' for rim assembly. This register is not a trivial consequence of steric crowding, it defines how neighboring units share curvature, minimize clashes and maintain a consistent rim diameter. In this sense, the arrays represent a coherent OXPHOS architecture rather than a by-chance accumulation of complexes at a curved boundary. The finding provides a structural instantiation of the long-speculated respiratory strings/patches and explains how respiratory complexes can achieve long-range order by adhering to a pre-formed ATP synthase scaffold.

A bioenergetic advantage is the establishment of lateral proton gradient from the source of ETC to the sink of CV[31–33]. Such gradient does exist in respiring opisthokont cristae[34,35] and can drive faster ATP synthesis in both artificial proteoliposome systems[33] and, with the aid of CV regulator IF_1, *in vivo*[36]. Moreover, another benefit from locating ATP synthases to highly curved regions is their geometry-derived high electric capacities which, under a uniform mitochondrial potential ($\Delta\Psi_m$), would allow hosting more positively charged protons to generate a higher cross-IMM ΔpH[51] (Fig. 5d). In yeasts, acidic mitochondrial p-side and high percentage of ΔpH in total PMF have been demonstrated to be crucial for meaningful ATP production, suggesting that ΔpH is somehow more effective than $\Delta\Psi_m$ in driving phosphorylation[35]. Thus, it can be inferred that for ETC complexes, a flatter membrane would

confer a lower electric capacity, such that fewer protons are required to be translocated to achieve a standard $\Delta\Psi_m$. It is worth noting that the tubular cristae from ciliates seem to be an exception, as the uniform membrane curvature would equalize the electric capacities experienced by ETC complexes and ATP synthases[14,15,42,43]. The architecture of long range OXPHOS arrays and its possible unique implications in ciliate bioenergetics remain unknown at the moment.

Taken together, our cryo-EM and cryo-ET turn the long-speculated 'respiratory string/patch'[37–41] into a structural reality. The arrays we visualize integrate ETC complexes and ATP synthase into a single, repeating architecture that is tuned to discoidal cristae. Thus, in kinetoplastids, the discoidal rim is not simply a passive consequence of ATP synthase dimerization, it is actively maintained by an integrated OXPHOS architecture in which respiratory complexes serve as structural endpieces and together with ATP synthase build long-range arrays adapted to the local curvature of the energized membrane. In a broader context, our studies define a multi-scale blueprint for kinetoplastid crista morphogenesis, from atomic interfaces to supercomplex assembly to membrane-scale packing rules, and suggest that robust bioenergetic function can be achieved by evolving not only efficient catalysts, but also architectures that reliably host and organize them *in vivo*.

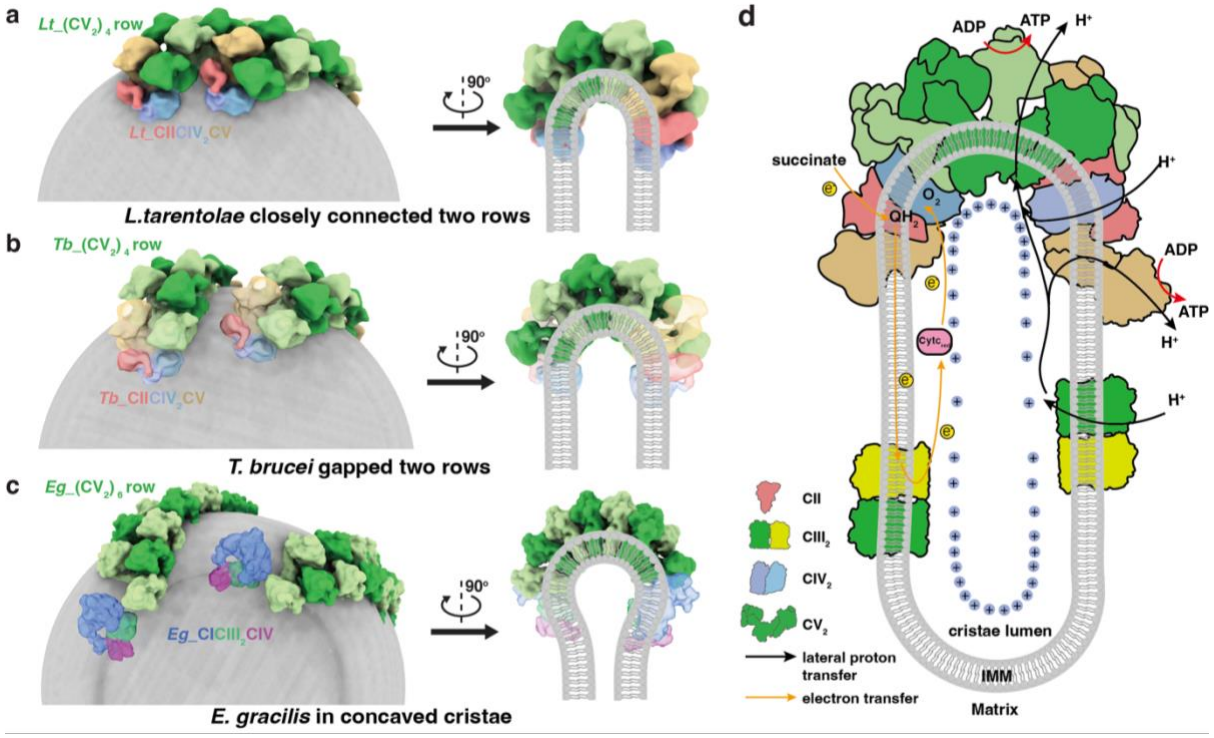

Fig. 5 | Cristae shaping and bioenergetic strategies by Discoba OXPHOS. a-c, Different strategies of discoidal cristae shaping by long range OXPHOS arrangements. *L. tarentolae* (**a**) and *T. brucei* (**b**) respectively use strictly aligned and flexibly adapted CIICIV$_2$CV-capped CV$_2$ rows to form disk-shaped cristae, while *E. gracilis* (**c**) possibly involves canonical respirasomes at its CV$_2$ row termini to shape biconcave cristae. **d**, Schematic representation of *L. tarentolae*'s discoidal cristae and the OXPHOS arrays and complexes. The proton density varies in accordance with the membrane curvature-induced electric capacity gradient. The electron transport (yellow arrows) coupled lateral proton transfer (black arrows) is in the direction from CIII$_2$ populated cristae center to CV$_2$ nested rim.

Methods

Leishmania tarentolae culture and mitochondria isolation - WT *L. tarentolae* promastigotes (ATCC 30143) was purchased from the American Type Culture Collection and cultured at 27 °C with constant agitation at 100 rpm, in SDM79 medium supplemented with 10% (v/v) heat-inactivated (56 °C, 30 min) fetal bovine serum (FBS) and 7.5 µg/ml hemin[56–58]. Unless otherwise specified, all the following procedures were carried out at 4 °C.

For mitochondria isolation[59], ~5 × 10^{10} cells at mid-log phase were harvested by centrifugation at 11,000 × g for 10 minutes. The cell pellet was immediately weighed and resuspended in Wash buffer (20 mM sodium phosphate pH 7.9, 150 mM NaCl, 20 mM

glucose) at a ratio of 8 ml/g wet weight. Following centrifugation at 11,000 × g for 10 minutes, the cell pellet was resuspended in Hypotonic buffer (1 mM Tris-HCl pH 8.0, 1 mM EDTA) and disrupted by 100 strokes in a 40ml Dounce homogenizer. The cell lysis was stopped by dropwise addition of 1 M sucrose to a final sucrose concentration of 0.25 M. Crude mitochondria were pelleted by centrifugation at 16,000 × g for 15 minutes and resuspended in Isotonic buffer (20 mM Tris-HCl pH 8.0, 250 mM sucrose, 5 mM $MgCl_2$, 0.3 mM $CaCl_2$). The final volume of the resuspension was measured by pipette and DNase I was added to a final concentration of 5 μg/ml (1/2600 vol of 13 mg/ml stock). The mixture was incubated on ice for 60 min, followed by the addition of an equal volume of STE buffer (20 mM Tris-HCl pH 8.0, 250 mM sucrose, 2 mM EDTA). The crude mitochondria were pelleted by centrifugation at 4 °C and 16,000 × g for 15 minutes, resuspended in minimal volume of STE buffer and loaded on a discontinuous sucrose gradient with 30%, 45%, and 60% (w/v) in buffer containing 10 mM Tris-HCl, pH 7.4, 2 mM EDTA, and 0.002% PMSF. Loaded gradients were centrifuged at 29,000 rpm for 2 hours in an Optima XPN ultracentrifuge equipped with an SW32 Ti rotor (Beckman Coulter). The resulting fine mitochondria were harvested from the 45–60% sucrose interface, further diluted with an equal volume of sucrose-free STE buffer (20 mM Tris-HCl pH 8.0, 2 mM EDTA) and pelleted again by centrifugation at 20,000 × g for 15 minutes. The fine mitochondria pellet was labeled by its measured mass and stored at -80 °C until use.

Plasmid construction and generation of $CIII_2$-affinity tagged cell line - The plasmid pLEXSY-hyg2.1_LtIFT43_Flag[60,61] was obtained from Addgene (catalog no. 194433). The coding sequence of the *L. tarentolae* CIII subunit MPPα, with a Strep tag at its C-terminus, was synthesized by General Biol. The synthesized sequences were inserted between the BglII and KpnI restriction sites to generate pLEXSY-hyg2.1_LtMPPα_Strep. For a cloning and transfection control, the enhanced green fluorescent protein (EGFP) sequence was amplified by polymerase chain reaction (PCR) from a laboratory-available template and a pLEXSY-hyg2.1_EGFP vector was constructed by the same procedure.

After amplification in *E. coli* DH5α, approximately 10 μg of each expression vector was digested by SwaI to produce two fragments: a 2.9 kbp plasmid backbone and a larger linear expression cassette. The latter fragment was purified by agarose gel electrophoresis and gel extraction and was used for chromosome integration at the 18S locus of the ribosomal DNA subunit (ssu). Electroporation was performed following the manufacturer's instructions for the LEXSYcon2.1 Expression Kit (Jena Bioscience). Wild-type *L. tarentolae* cells, grown in brain-heart infusion-based (BHI) medium (BHI powder 38g/L, Qingdao Hope Bio-Technology Co., Ltd. 10% FBS, 7.5 μg/ml hemin) supplemented with 10% (v/v) heat-inactivated FBS and 7.5 μg/ml hemin, was concentrated by 10 fold via centrifugation and resuspension in the electroporation buffer (10 mM K_2HPO_4 pH 7.6, 120 mM KCl, 0.15 mM $CaCl_2$, 25 mM HEPES pH 7.6, 2 mM EGTA pH 7.6, 5 mM $MgCl_2$, 0.5% glucose (w/v), 10% BSA (w/v),1 mM hypoxanthine). The cells and the purified expression cassette fragments were first pre-cooled on ice for 10 min before mixing. Electroporation was carried out using an Amaxa Nucleofector II with program X-001[62,63]. pLEXSY-hyg2.1_EGFP and empty vector were electroporated in parallel as positive and negative controls respectively. 20 hours post-electroporation, 50 μg/ml hygromycin B was added for selection. After 12 days, green fluorescence was observed in the EGFP-positive control under a fluorescence microscope with green channel, whereas all cells in the negative control were non-viable. Cells in the experimental groups showed active proliferation and their genomic DNA was extracted for PCR verification of correct chromosome integration, using both primer pairs of F3001+A1715 and F3002+A3804 (Table S6). Single clones were subsequently isolated in 96-well plates and expanded to obtain the $CIII_2$-tagged cell line.

Mitochondrial supercomplex purification - All the following biochemical steps were performed at 4 °C unless otherwise stated. To isolate the mitochondrial membrane fraction, the fine mitochondria pellet was thawed and homogenized in milli-Q water at 10 ml per gram of mitochondria mass using a KIMBLE Dounce tissue grinder. The homogenate was added

by 3 M KCl to a final KCl concentration of 150 mM and homogenized again to dissociate the peripheral membrane proteins. The homogenate was pelleted by centrifugation at 32,000 × g for 45 minutes, resuspended by homogenization in M10 buffer (20 mM Tris pH 7.4, 50 mM NaCl, 1 mM EDTA, 2 mM DTT, 0.002% PMSF (w/v) and 10% glycerol (v/v)) at 18 ml per gram of mitochondria mass as a washing step and pelleted again by centrifugation at 32,000 × g for 45 minutes. The resulting mitochondrial membrane pellet was weighed and resuspended in buffer MX (30 mM HEPES pH 7.7, 150 mM KOAc, 10% glycerol, 0.002% PMSF) at 1.5 ml per gram of membrane mass by homogenization. Total protein concentration was determined using a bicinchoninic acid (BCA) assay kit (Beijing LABLEAD Trading Co., Ltd.) following the manufacturer's instructions.

For purification of ETC-CV supercomplexes, the obtained mitochondrial membrane containing ~150 mg total protein was solubilized in buffer MX (30 mM HEPES pH 7.7, 150 mM potassium acetate, 0.002% PMSF, 10% (v/v) glycerol) supplemented with 1% digitonin at a detergent-to-protein ratio of 3:1 (w/w) for 1 hours with gentle agitation. After removal of insoluble materials by centrifugation at 16,000 × g for 45 minutes, the supernatant was filtered through a 0.45-µm filter and loaded onto a 5-ml Q-Sepharose HP column (Cytiva) equilibrated in Q-A buffer (30 mM Tris pH 7.4, 50 mM NaCl, 2 mM $MgCl_2$, 0.002% PMSF (w/v), 10% glycerol (v/v), 0.015% glyco-diosgenin (GDN) (w/v)) for anion exchange chromatography (ANX). The column was first washed with 25 ml Q-A buffer and then eluted with a 70 ml linear gradient from 5% to 70% Q-B buffer (Q-A buffer with 1 M NaCl) mixed in Q-A buffer. Fractions were checked by Tris-glycine blue-native polyacrylamide gel electrophoresis (BN-PAGE) and in-gel ATP synthase/CV activity assay using CV buffer (50mM glycine pH 8.5, 5mM $MgCl_2$, 5mM ATP, 2mM $Pb(CH3COO)_2$) and in-gel CIV activity assay using CIV buffer (50mM sodium phosphate pH 7.2, 0.05% 3,3-diaminobenzidine tetrahydrochloride and 50 µM commercial porcine heart cytochrome *c* (cyt *c*, (Macklin)). Fractions exhibiting highest CIV and CV activity bands were pooled and concentrated to ~500 µl using a 100 kDa molecular weight cutoff (MWCO) centrifugal

concentrator. The concentrated sample was then loaded onto a Superose 6 Increase 10/300 GL column (Cytiva) for size-exclusion chromatography (SEC) purification using SEC buffer (20 mM Tris pH 7.4, 50 mM NaCl, 5 mM $MgCl_2$, 0.002% PMSF (w/v), 0.015% GDN (w/v)). SEC fractions were again subjected to BN-PAGE and CIV and CV activity staining. Fractions containing supercomplexes $CII_2CIV_2CV_2$, $CIICIV_2V_3$ and $CII_2CIV_4CV_{10}$ eluted at ~9 ml with a peak concentration of approximately 0.3 mg/ml and were used directly for cryo-EM grid preparation before snap freezing and storage in liquid N_2.

For purification of $CIII_2$-containing supercomplexes, C-terminal strep-tagged MPPα expressing cell line was cultured on large scales, and mitochondria were isolated following the procedures described above. Membrane proteins were extracted with digitonin and sequentially purified using a combination of Strep-affinity chromatography, ANX and SEC. For membrane extraction, mitochondrial membrane fractions were resuspended in MX buffer and solubilized with 1% digitonin at a detergent-to-protein ratio of 3:1 (w/w) with gentle agitation for 1 hour. The sample was centrifuged at 16,000 × g for 45 minutes and filtered through a 0.45-µm membrane. For strep-affinity chromatography, the supernatant was loaded onto a 5 ml StrepTrap XT column (Cytiva) pre-equilibrated with Strep-A buffer (100 mM Tris pH 8.0, 150 mM NaCl, 1 mM EDTA, 0.015% GDN (w/v)). After washing with 25 ml Strep-A buffer, bound proteins were eluted with 40 ml 100% Strep-B buffer (Strep-A buffer with 150 mM biotin). Affinity-purified peak fractions were pooled and further purified by ANX and SEC with the same procedure as above. After BN-PAGE and in-gel CIV and CV activity staining, no CV activity was found. Fractions exhibiting CIV activity were pooled and concentrated to ~0.5 mg/ml using a 100 kDa MWCO centrifugal concentrator, before cryo-EM grid preparation.

Spectroscopic activity assays - CII, CIV and ATP synthase activities[64] were determined spectroscopically as 2,6-dichlorophenol-indophenol (DCPIP) reduction[65], NADH oxidation[66] and reduced cyt *c* oxidation rates in the presence or absence of CII (malonate), CIV (KCN)

and CV (oligomycin A) inhibitors (Aladdin). All activities were measured in triplicates in 384-well plates at room temperature (RT) using a Multiskan SkyHigh plate reader (ThermoFisher Scientific) with a total reaction volume of 20 µl per well. The reaction master mixture used for all activity assays consisted of 20 mM Tris-HCl pH 7.4, 50 mM NaCl, 0.015% GDN (w/v) and 0.002% PMSF. The protein sample used was the same as that for the grid preparation of the ETC-CV supercomplex cryo-EM dataset, concentrated to ~3 mg/ml. The molar extinction coefficients of 6.22, 19.1 and 6.5 $mM^{-1}cm^{-1}$ were used for NADH, DCPIP and porcine cyt *c* in activity calculations[64].

For CII activity, 1 µl protein sample, 20 mM succinate and 75 µM DCPIP were added to the master mixture, with or without 10 mM malonate. 25 µM decylubiquinone (DQ) was then added to start the reaction. The mixture was rocked in the spectrophotometer for 5 s and 600 nm absorbance was recorded every 6 s for 10 min. CII activities were calculated as the DCPIP reduction rates, based on the slope of the initial linearly decreasing phase in the 600 nm kinetic curve.

For CIV activity, 50 µM porcine reduced cyt *c* (Macklin) was added to the master mixture, with or without 750 µM KCN. 1 µl protein sample was then added to start the reaction. The mixture was rocked in the spectrophotometer for 5 s and recorded every 6 s for ~10 min at 550 nm. CIV activities were calculated as the cyt *c* oxidation rates, based on the slopes of the initial linearly decreasing phase in the 550 nm kinetic curves.

For CV ATP hydrolytic activity, 1 µl protein sample, 5 mM $MgCl_2$, 300 µM NADH, 2.5 mM phosphoenolpyruvate, 50 mg/ml pyruvate kinase and 50 mg/ml lactate dehydrogenase were added with or without 200 µM oligomycin A. 2.5mM ATP, pH 7.0 was then added to start the reaction. The mixture was rocked in the spectrophotometer for 5 s and then recorded every 6 s for ~20 min at 340 nm. CV ATP hydrolytic activities were calculated as the NADH oxidation rates, based on the slopes of the initial linearly decreasing phase in the 340 nm

603 kinetic curves.

604

605 *Cryo-EM grid preparation and data collection* - The cryo-EM grid preparation and data
606 collection were carried out at the Center of Cryo-Electron Microscopy at Zhejiang University.
607 For all datasets, 3.5 µl sample was applied to pre-glow discharged Quantifoil R1.2/1.3 300
608 mesh copper grid with 2 nm continuous carbon layer before blotting for 2 s under 100%
609 humidity at 4 °C and vitrification in liquid ethane by Vitrobot Mark IV (ThermoFisher
610 Scientific). Grids were transferred to liquid N_2 for storage before data collection. Cryo-EM
611 micrographs were collected on a Titan Krios G2 microscope (ThermoFisher Scientific)
612 operating at 300 kV, equipped with a Falcon 4i detector operating at 320 frames/s and a
613 Selectris energy filter. EPU software was used for automated data collection following
614 standard procedures. For all datasets, the grids were imaged at a calibrated magnification of
615 ×105,000 with a physical pixel size of 1.2 Å and a defocus range from -0.8 to -2.0 µm. A total
616 dose of 45 $e^-/Å^2$ with 5.21 s exposure time was fractionated into 1667 frames. A total of
617 24693 and 6602 raw micrographs were collected for the dataset of ETC-CV supercomplexes
618 and the dataset of $CIII_2$-containing supercomplexes.

619

620 *Cryo-EM image processing* - Raw micrographs of all collected datasets were imported into
621 cryoSPARC (v4.6.2)[67] for patch motion correction and contrast transfer function (CTF)
622 estimation. Particles were initially picked and extracted using boxsize 720 for both the ETC-
623 CV supercomplex and the $CIII_2$-containing supercomplex datasets.

624

625 For the ETC-CV supercomplex dataset, a total of 4,048,443 particles were picked from
626 24,693 micrographs. After 2D classification, *ab initio* reconstruction of the initial reference
627 volumes and subsequent heterogeneous refinement classified out supercomplexes
628 $CII_2CIV_2CV_2$, $CIICIV_2CV_3$, $CII_2CIV_4CV_{10}$, $CIICIV_2CV$ and CV_2.

629

630 For the $CII_2CIV_2CV_2$ class, 111,613 particles were used for overall homogeneous refinement

and non-uniform refinement[68] with global[69] and local[70] CTF corrections under C2 symmetry, yielding an overall resolution of 2.7 Å. Local refinement of CII was first performed to generate a consensus CII map using all the $CII_2CIV_2CV_2$ particles, at near-Nyquist resolution (2.5 Å). However, the *c*-ring and F_1 regions of CV were barely visible, indicating mixing of different CV rotational states. To distinguish rotational states, the $\alpha_3\beta_3$+central stalk (CV_$\alpha_3\beta_3$+CS) region of F_1 and membrane-embedded, stator region of the CV (CV_F_o_stator) were respectively local refined to resolutions of 2.5 Å and 3.2 Å. Focused 3D classifications masking the $\alpha_3\beta_3$+CS region or the F_o+ peripheral stalk and the bottom parts of the central stalk (CV_F_o+PS+CS_{bottom}) both revealed three distinct rotational states, albeit with different particle number distributions. For the former, CV_$\alpha_3\beta_3$+CS masked classification, local refinements of the *c*-ring and the PS regions did not improve their resolutions compared to overall refinement. This suggested the presence of sub-states. The CV_$\alpha_3\beta_3$+CS masked classification was not pursued further due to limited F_o resolutions.

On the other hand, for the CV_F_o+PS+CS_{bottom} masked classification, systematic local refinements of at least the rotational state 1 (36,870 particles) gave uniform, sub-4.0 Å resolutions for nearly all the different regions, apart from the PS (4.7 Å). The local refinements performed included regions of CII, CII linkage domain, CIV_2, CV_F_o_stator, CV_$\alpha_3\beta_3\gamma_{top}$, CV_*c*-ring+$CS_{bottom}$ and CV_PS. To reveal sub-states and improve resolutions of the *c*-ring and PS regions under this classification scheme, local 3D classification focusing on the CV_*c*-ring+CS_{bottom} and the CV_PS regions were performed and resolved several sub-states, differing in the rotational positions of the *c*-ring and the wobbling positions of the PS, respectively. Such procedures indeed improved resolutions of the *c*-ring (best at 3.6 Å) and the PS (best at 4.2 Å), both with much enhanced structural features. However, the CV_*c*-ring+CS_{bottom} classified and the CV_PS classified sub-states did not strictly correlated to each other, in a sense that particles belonging to a certain *c*-ring sub-state could be spread across different PS sub-states. Due to the limit of total available $CII_2CIV_2CV_2$ particles, local refinements of the intersects of these two types of sub-states were not pursued further. In the

end, composite map of $CII_2CIV_2CV_2$ was generated using local refinements of the 36,870 rotational state 1 particles, with the Combine Focused Maps program in Phenix-1.20.1[71]. The improved *c*-ring and PS maps were separately deposited to ensure the particle consistency of the composite map.

For the $CIICIV_2CV_3$ class, 128,401 particles were used for overall homogeneous refinement and non-uniform refinement[68] with global[69] and local[70] CTF corrections under C1 symmetry, yielding an overall resolution of 3.3 Å. Both the $CIICIV_2CV$ and CV_2 regions locally refined to 3.2 Å. For CV_2, C2 symmetry expansion improved the resolution to 3.0 Å. Direct local refinement of the CV_F_o_stator reported resolution of 3.2 Å. For the CV_$\alpha_3\beta_3\gamma_{top}$, CV_PS and CV_*c*-ring+$CS_{bottom}$ regions, additional steps of local 3D classification improved the resolutions to 3.6 Å, 5.0 Å and 4.3 Å. These local refinements were combined with the Combine Focused Maps program in Phenix-1.20.1[71] to generate a composite CV_2 map. Note that local refinements of the CV_$\alpha_3\beta_3\gamma_{top}$, CV_PS and CV_*c*-ring+$CS_{bottom}$ regions were from a subset of the 256,802 C2 expanded $CIICIV_2CV_3$ particles. For $CIICIV_2CV$, direct local refinements of CII, CIV_2 and CV_F_o_stator reported resolutions of 3.0 Å, 3.1 Å and 2.9 Å. The same procedure was performed for CV_$\alpha_3\beta_3\gamma_{top}$, CV_PS and CV_*c*-ring+$CS_{bottom}$ regions, reporting resolutions of 3.9 Å, 6.6 Å and 5.8 Å, respectively. Composite map of supercomplex $CIICIV_2CV$ were similarly generated. In the end, a composite $CIICIV_2CV_3$ map was generated using the composite maps of $CIICIV_2CV$ and CV_2.

For the $CII_2CIV_4CV_{10}$ class, 71,177 particles were used for overall homogeneous refinement and non-uniform refinement[68] with both global[69] and local[70] CTF corrections under C2 symmetry, yielding an overall resolution of 4.9 Å. Initial local refinement of the asymmetric unit $CIICIV_2CV_5$ improved the resolution to 3.5 Å. Further local refinements of $CIICIV_2CV$ region and the first and second CV_2 copies (CV_2-1 and CV_2-2) yielded resolutions of 3.5 Å, 3.1 Å and 3.5 Å, respectively. More local refinements of all the different regions in $CIICIV_2CV$, CV_2-1 and CV_2-2 were directly performed, since local 3D classification

wouldn't help too much with either the resolution or the structural features under the current particle number and orientation distribution. A composite map of supercomplex $CII_2CIV_4CV_{10}$ was generated as above described using these local refinements[71]. The spIsoNet[72] program was used to alleviate the map anisotropy due to the preferred top-view orientation of such massive complex particle on the grid compared to side views.

For the $CIII_2$-containing supercomplex dataset, a total of 1,267,679 particles were picked from 6,602 micrographs and extracted using boxsize 600. Following 2D classification, 3D *ab-initio* reconstruction and subsequent heterogeneous refinement, 85,890 $(CIII_2)_2$ particles were subjected to homogeneous refinement and non-uniform refinement[68] with both global[69] and local[70] CTF corrections under C1 symmetry, yielding an overall resolution of 2.7 Å. Local refinements of the first and second $CIII_2$ copies yielded resolutions of 2.6 Å and 2.9 Å, respectively. Composite map of supercomplex $(CIII_2)_2$ were generated as above[71].

25,042 $(CIII_2)_4$ particles were re-extracted with boxsize 720 and subjected to homogeneous refinement and non-uniform refinement[68] with both global[69] and local[70] CTF corrections under C1 symmetry, yielding an overall resolution of 3.5 Å. Local refinement of the first $(CIII_2)_2$ copy yielded resolution of 3.1 Å. Further local refinements of its two $CIII_2$ copies yielded resolutions of 2.8 Å and 3.0 Å. However, the second $(CIII_2)_2$ copy was barely visible. To separate $(CIII_2)_4$ from $(CIII_2)_2$, local refinement was first performed on the second $(CIII_2)_2$ copy using these 25,042 particles, yielding a resolution of 7.7 Å. These locally refined particles were then exported to Relion-4.0[73] for subsequent 3D classification without alignment. 16,071 particles with improved density of the second $(CIII_2)_2$ copy was classified, which refined to an overall resolution of 4.3 Å. Composite map of supercomplex $(CIII_2)_4$ were generated as above[71]. All map resolutions were determined using the gold standard Fourier shell correlation (FSC) between two half maps, generated by refinement jobs, at a cutoff of 0.143[74].

Model building - All manual model building was performed in Coot-0.9.6[75]. Mainchain backbones for conserved subunits were built by first rigid-body fitting published structures into respective local refinement maps in ChimeraX-1.5[76–78], then manually adjust in Coot according to densities. Reference models used to facilitate model building included porcine CII (PDB 1ZOY)[79], *T. thermophila* CII, $CIII_2$ and CIV_2 (PDB 8B6G, 8B6J and 8B6H)[42], *E. gracilis* $CIII_2$ and CIV (PDB 8IUF)[23] and *T. brucei* CV (PDB 8APA)[47]. Mainchain backbones of non-CV *L. tarentolae*-specific subunits were built *de novo* according to density. Sequences of each subunit were identified according to published methods[80]. Briefly, side chains of above built backbones were added *de novo* according to density and the generated query sequences were used in BLAST searches against the *L. tarentolae* proteome either from UniProt (UP000419144)[81] or from the TriTrypDB website[82,83]. For several sequences that were difficult to identify, we employed the tblastn approach from protein to translated nucleotide. The manually built CII, $CIII_2$, CIV_2 and CV subunits were rigid-body fitted into the composite $CII_2CIV_2CV_2$, $CIICIV_2CV_3$, $CII_2CIV_4CV_{10}$, $(CIII_2)_2$ and $(CIII_2)_4$ maps with chain ID adjusted as in tables S4 and S5. Automatic model refinements were performed using the phenix.refine[84] and phenix.real_space_refine[85] programs, initially using automatically generated secondary structure restraints, custom bond linkage and custom ligand description file by Phenix-1.20.1[71]. The output models were then manually edited according to refinement outcome in Coot[75], with assistance from secondary structure information predicted by AlphaFold[86]. The next round of automatic refinements were then performed and this iterative process continues until the refined model reported high model-map correlation and good geometric statistics[87]. Side chains in the $CII_2CIV_4CV_{10}$ model were truncated to C_β before automatic refinement to better reflect the map resolution and quality. A total of 13, 13, 17 and 27 subunits were built for CII, CIII, CIV and CV, among which 8, 2, 4 and 6 subunits were *L. tarentolae*-specific.

Cryo-ET sample preparation and data collection - Fine mitochondria pellets from the 45%-60% interface of the sucrose gradient were resuspended in 100 µl of TE buffer (20 mM Tris-

HCl pH 8.0, 2 mM EDTA) at 8 mg/ml protein concentration, measured by 280 nm absorbance in the Multiskan SkyHigh plate reader (ThermoFisher Scientific)[88]. The resuspension was mixed 3:1 with 20× concentrated 10 nm gold fiducial markers (Aurion). 3 µl of this mixture was applied to a glow-discharged R2/1 Cu 300-mesh grid (Quantifoil) and blotted by Vitrobot Mark IV (ThermoFisher Scientific) for 7 s under 100% humidity at 8 °C before plunge freezing in liquid ethane. Grids were transferred to liquid N_2 for storage before data collection. Cryo-ET data were collected at the Shuimu BioSciences for Cryo-EM facility at Hangzhou, China. Tilt-series data were collected as dose-fractionated movies in EER format, using a Titan Krios G4 transmission electron microscope operating at 300 kV equipped with a Selectris X energy filter set to 10 eV slit width and a Falcon 4 direct electron detector (ThermoFisher Scientific). The grids were imaged at a calibrated magnification of ×64,000, corresponding to a pixel size of 1.972 Å at the specimen level and a nominal dose of 3.5 $e^-/Å^2$ per tilt image. Tilt series were acquired in a dose-symmetric scheme[89] with a tilt range of -51° to 51° and with 3° increments grouped by three tilts, using the TEM Tomography 5 software (ThermoFisher Scientific). The nominal defocus ranged from -2 µm to -4 µm in 0.25 µm steps.

Cryo-ET processing and subtomogram averaging - The raw movies of 92 tilt-series were imported into Warp (v2.0.0)[90] for movie frame alignment, CTF estimation, tilt series alignment, and tomographic reconstruction. Subtomograms of individual CVs were selected from three typical tomograms using a neural-net based particle picker in EMAN2[91] and extracted in Warp. Using the aforementioned SPA-derived monomeric CV 3D model as initial model, these subtomograms were refined in RELION-5.0.1[92]. The resultant data-derived monomeric CV map was subsequently employed as a template for template matching in PyTom[93], leading to the extraction of 423,200 candidate particles from all 92 tomograms. All subsequent classification steps were performed in RELION. These subtomograms were subjected to 3D classification into six classes with global alignment using a spherical mask of 280 Å in diameter, yielding a subset of 63,396 CV-containing particles. These particles were

771 then shifted to re-center on the CV pseudo-dimer and re-extracted for 3D classification
772 without alignment using a mask that focuses on a region that corresponds to $CIICIV_2$, as
773 determined by the aforementioned SPA map of $CIICIV_2CV_3$. This led to the identification of
774 4,358 $CIICIV_2$-containing particles, which were refined in RELION and M[94] to generate a
775 $CIICIV_2CV_3$ map at 19 Å resolution. Nevertheless, the local resolution of $CIICIV_2$ and an
776 adjacent CV were not as good as those of the remaining CVs. To improve map quality,
777 $CIICIV_2CV_2$ was masked out and used as a template for another round of PyTom template
778 matching, yielding 574,200 particles using the same 92 tomograms. These particles were
779 classified into four classes with global alignment and a spherical mask of 400 Å in diameter,
780 resulting in 114,961 particles with CV pseudo-dimer densities. Two major, compositionally
781 distinct species were obtained upon further 3D classification without alignment using a
782 $CIICIV_2$-focused mask. One species contained 2,526 particles that were refined in RELION
783 and M to produce a $CIICIV_2CV_3$ reconstruction at approximately 21 Å resolution, but with
784 improved structural features than the previous round of $CIICIV_2CV_3$ refinement. The second
785 species comprised 11,580 particles with similar occupancies for all four CV subunits, of
786 which 7,143 particles were kept based on an inter-particle distance threshold of 160 Å. These
787 particles were then refined in RELION and M to generate a CV_4 map at approximately 17 Å
788 resolution. Map resolutions were determined using the gold standard FSC between two half
789 maps at a cutoff of 0.143[74]. Subtomograms were mapped back to original tomograms using
790 the ArtiaX[95] plugin in ChimeraX. Membrane segmentation was performed automatically
791 using MemBrain-V2[96,97], and membrane curvatures were computed using PyCurv[98] and
792 Surface Morphometrics[99].
793
794 **Data availability:** The composite maps and structural models and for *L. tarentolae*
795 mitochondrial supercomplexes are available from the Electron Microscopy Database
796 (EMDB) and the Protein Data Bank (PDB) and with the following accession codes.
797 $CII_2CIV_2CV_2$: EMD-67545 and PDB-21BE; $CIICIV_2CV_3$: EMD-67546 and PDB-21BF;
798 $CII_2CIV_4CV_{10}$: EMD-67544 and PDB-21BD; $CIII_4$: EMD-67547 and PDB-21BG; $CIII_8$:

799 EMD-69165 and PDB-23QD; CII: EMD-68897 and PDB-23DZ. Maps for consensus and
800 local refinements are available from the EMDB with the following accession codes.
801 $CII_2CIV_2CV_2$: consensus map EMD-67652, CII region EMD-67641, CIV region EMD-
802 67645, CV_F_o_stator region EMD-67647, CV_$\alpha_3\beta_3$+CS region EMD-67649, CV_*c*-
803 ring+CS_{bottom} region EMD-67650, CV_peripheral_stalk region EMD-67651, CV_*c*-
804 ring+CS_{bottom}_state 1a EMD-69268, CV_*c*-ring+CS_{bottom}_state 1b EMD-69275, CV_*c*-
805 ring+CS_{bottom}_state 2a EMD-69276, CV_*c*-ring+CS_{bottom}_state 2b EMD-69269, CV_*c*-
806 ring+CS_{bottom}_state 2c EMD-69277, CV_*c*-ring+CS_{bottom}_state 3a EMD-69270, CV_*c*-
807 ring+CS_{bottom}_state 3b EMD-69278, CV_peripheral_stalk_state 1 EMD-69273,
808 CV_peripheral_stalk_state 2 EMD-69271, CV_peripheral_stalk_state 3 EMD-69272,
809 CV_peripheral_stalk_state 4 EMD-69274; $CIICIV_2CV_3$: consensus map EMD-67643, CII
810 region EMD-67615, CIV_2 region EMD-67614, CV_F_o_stator region EMD-67617,
811 CV_$\alpha_3\beta_3$+CS region EMD-67567, CV_*c*-ring+CS_{bottom} region EMD-67619,
812 CV_peripheral_stalk region EMD-67637, CV_2_F_o_stator region EMD-67638, CV_2_$\alpha_3\beta_3$+CS
813 region EMD-67639, CV_2_*c*-ring+CS_{bottom} region EMD-67640, CV_2_peripheral_stalk region
814 EMD-67644; $CII_2CIV_4CV_{10}$: consensus map EMD-67695, CII region EMD-67680, CIV_2
815 region EMD-67681, CV_F_o_stator region EMD-67682, CV_$\alpha_3\beta_3\gamma_{top}$ region EMD-67683,
816 CV_*c*-ring+CS_{bottom} region EMD-67685, CV_peripheral_stalk region EMD-67686,
817 CV_2_F_o_stator region EMD-67688, CV_2_$\alpha_3\beta_3$+CS-1 region EMD-67689, CV_2_*c*-ring-1
818 region EMD-67690, CV_2_peripheral_stalk-1 region EMD-67691, CV_2_$\alpha_3\beta_3$+CS-2 region
819 EMD-67692, CV_2_*c*-ring-2 region EMD-67693, CV_2_peripheral_stalk-2 region EMD-67694;
820 $(CIII_2)_2$: consensus map EMD-67674, $CIII_2$-1 region EMD-67653, $CIII_2$-2 region EMD-
821 67654; $(CIII_2)_4$: consensus map EMD-69041, $CIII_2$-1 region EMD-69037, $CIII_2$-2 region
822 EMD-69038; $(CIII_2)_2$-1 region EMD-69045; $(CIII_2)_2$-2 region EMD-69040. For
823 subtomogram averaging maps, $CIICIV_2CV_3$: EMD-68795; CV_4: EMD-68796.
824

References

1. Davies, K. M., Strauss, M., Daum, B., Kief, J. H., Osiewacz, H. D., Rycovska, A., Zickermann, V. & Kühlbrandt, W. Macromolecular organization of ATP synthase and complex I in whole mitochondria. *Proceedings of the National Academy of Sciences of the United States of America* **108**, 14121–6 (2011).
2. Waltz, F., Righetto, R. D., Lamm, L., Salinas-Giegé, T., Kelley, R., Zhang, X., Obr, M., Khavnekar, S., Kotecha, A. & Engel, B. D. In-cell architecture of the mitochondrial respiratory chain. *Science (New York, N.Y.)* **387**, 1296–1301 (2025).
3. Vercellino, I. & Sazanov, L. A. The assembly, regulation and function of the mitochondrial respiratory chain. *Nature reviews. Molecular cell biology* **23**, 141–161 (2022).
4. Wikström, M., Sharma, V., Kaila, V. R. I., Hosler, J. P. & Hummer, G. New perspectives on proton pumping in cellular respiration. *Chemical reviews* **115**, 2196–221 (2015).
5. Walker, J. E. The ATP synthase: the understood, the uncertain and the unknown. *Biochemical Society transactions* **41**, 1–16 (2013).
6. Kühlbrandt, W. Structure and Mechanisms of F-Type ATP Synthases. *Annual review of biochemistry* **88**, 515–549 (2019).
7. Gu, J., Zhang, L., Zong, S., Guo, R., Liu, T., Yi, J., Wang, P., Zhuo, W. & Yang, M. Cryo-EM structure of the mammalian ATP synthase tetramer bound with inhibitory protein IF1. *Science (New York, N.Y.)* **364**, 1068–1075 (2019).
8. Davies, K. M., Anselmi, C., Wittig, I., Faraldo-Gómez, J. D. & Kühlbrandt, W. Structure of the yeast F1Fo-ATP synthase dimer and its role in shaping the mitochondrial cristae. *Proceedings of the National Academy of Sciences of the United States of America* **109**, 13602–7 (2012).
9. Guo, H., Bueler, S. A. & Rubinstein, J. L. Atomic model for the dimeric FO region of mitochondrial ATP synthase. *Science* **358**, 936–940 (2017).
10. Spikes, T. E., Montgomery, M. G. & Walker, J. E. Structure of the dimeric ATP

853 synthase from bovine mitochondria. *Proceedings of the National Academy of Sciences*
854 *of the United States of America* **117**, 23519–23526 (2020).
855 11. Blum, T. B., Hahn, A., Meier, T., Davies, K. M. & Kühlbrandt, W. Dimers of
856 mitochondrial ATP synthase induce membrane curvature and self-assemble into rows.
857 *Proceedings of the National Academy of Sciences of the United States of America* **116**,
858 4250–4255 (2019).
859 12. Mühleip, A., Kock Flygaard, R., Ovciarikova, J., Lacombe, A., Fernandes, P., Sheiner,
860 L. & Amunts, A. ATP synthase hexamer assemblies shape cristae of Toxoplasma
861 mitochondria. *Nature communications* **12**, 120 (2021).
862 13. Dietrich, L., Agip, A.-N. A., Kunz, C., Schwarz, A. & Kühlbrandt, W. In situ structure
863 and rotary states of mitochondrial ATP synthase in whole Polytomella cells. *Science*
864 *(New York, N.Y.)* **385**, 1086–1090 (2024).
865 14. Allen, R. D., Schroeder, C. C. & Fok, A. K. An investigation of mitochondrial inner
866 membranes by rapid-freeze deep-etch techniques. *The Journal of cell biology* **108**,
867 2233–40 (1989).
868 15. Mühleip, A. W., Joos, F., Wigge, C., Frangakis, A. S., Kühlbrandt, W. & Davies, K.
869 M. Helical arrays of U-shaped ATP synthase dimers form tubular cristae in ciliate
870 mitochondria. *Proceedings of the National Academy of Sciences of the United States of*
871 *America* **113**, 8442–7 (2016).
872 16. Mühleip, A. W., Dewar, C. E., Schnaufer, A., Kühlbrandt, W. & Davies, K. M. In situ
873 structure of trypanosomal ATP synthase dimer reveals a unique arrangement of
874 catalytic subunits. *Proceedings of the National Academy of Sciences of the United*
875 *States of America* **114**, 992–997 (2017).
876 17. Letts, J. A., Fiedorczuk, K. & Sazanov, L. A. The architecture of respiratory
877 supercomplexes. *Nature* **537**, 644–648 (2016).
878 18. Davies, K. M., Blum, T. B. & Kühlbrandt, W. Conserved in situ arrangement of
879 complex I and III2 in mitochondrial respiratory chain supercomplexes of mammals,
880 yeast, and plants. *Proceedings of the National Academy of Sciences of the United*

States of America **115**, 3024–3029 (2018).

19. Wu, M., Gu, J., Guo, R., Huang, Y. & Yang, M. Structure of Mammalian Respiratory Supercomplex I1III2IV1. *Cell* **167**, 1598-1609.e10 (2016).

20. Guo, R., Zong, S., Wu, M., Gu, J. & Yang, M. Architecture of Human Mitochondrial Respiratory Megacomplex I2III2IV2. *Cell* **170**, 1247-1257.e12 (2017).

21. Zhang, L., Guo, R., Xiao, C., Li, J., Gu, J. & Yang, M. Structural basis for the regulatory mechanism of mammalian mitochondrial respiratory chain megacomplex-I2III2IV2. *hLife* **2**, 189–200 (2024).

22. Zheng, W., Chai, P., Zhu, J. & Zhang, K. High-resolution in situ structures of mammalian respiratory supercomplexes. *Nature* **631**, 232–239 (2024).

23. He, Z., Wu, M., Tian, H., Wang, L., Hu, Y., Han, F., Zhou, J., Wang, Y. & Zhou, L. Euglena's atypical respiratory chain adapts to the discoidal cristae and flexible metabolism. *Nature communications* **15**, 1628 (2024).

24. MacLean, A. E., Shikha, S., Ferreira Silva, M., Gramelspacher, M. J., Nilsen, A., Liebman, K. M., Pou, S., Winter, R. W., Meir, A., Riscoe, M. K., Doggett, J. S., Sheiner, L. & Mühleip, A. Structure, assembly and inhibition of the Toxoplasma gondii respiratory chain supercomplex. *Nature structural & molecular biology* **32**, 1424–1433 (2025).

25. Nakano, A., Masuya, T., Akisada, S., Ishikawa-Fukuda, M., Mitsuoka, K., Miyoshi, H., Murai, M. & Yokoyama, K. Structures of respiratory supercomplexes and ATP synthase oligomers in mammalian mitochondrial inner membrane. *Nature communications* (2026) doi:10.1038/s41467-026-70578-x.

26. MITCHELL, P. Coupling of phosphorylation to electron and hydrogen transfer by a chemi-osmotic type of mechanism. *Nature* **191**, 144–8 (1961).

27. Mitchell, P. Chemiosmotic coupling in oxidative and photosynthetic phosphorylation. 1966. *Biochimica et biophysica acta* **1807**, 1507–38 (2011).

28. Daumke, O. & van der Laan, M. Molecular machineries shaping the mitochondrial inner membrane. *Nature reviews. Molecular cell biology* **26**, 706–724 (2025).

29. Pánek, T., Eliáš, M., Vancová, M., Lukeš, J. & Hashimi, H. Returning to the Fold for Lessons in Mitochondrial Crista Diversity and Evolution. *Current biology : CB* **30**, R575–R588 (2020).

30. Cherepanov, D. A., Feniouk, B. A., Junge, W. & Mulkidjanian, A. Y. Low dielectric permittivity of water at the membrane interface: effect on the energy coupling mechanism in biological membranes. *Biophysical journal* **85**, 1307–16 (2003).

31. Heberle, J., Riesle, J., Thiedemann, G., Oesterhelt, D. & Dencher, N. A. Proton migration along the membrane surface and retarded surface to bulk transfer. *Nature* **370**, 379–82 (1994).

32. Nilsson, T., Lundin, C. R., Nordlund, G., Ädelroth, P., von Ballmoos, C. & Brzezinski, P. Lipid-mediated Protein-protein Interactions Modulate Respiration-driven ATP Synthesis. *Scientific reports* **6**, 24113 (2016).

33. Sjöholm, J., Bergstrand, J., Nilsson, T., Šachl, R., Ballmoos, C. von, Widengren, J. & Brzezinski, P. The lateral distance between a proton pump and ATP synthase determines the ATP-synthesis rate. *Scientific reports* **7**, 2926 (2017).

34. Rieger, B., Junge, W. & Busch, K. B. Lateral pH gradient between OXPHOS complex IV and F(0)F(1) ATP-synthase in folded mitochondrial membranes. *Nature communications* **5**, 3103 (2014).

35. Toth, A., Meyrat, A., Stoldt, S., Santiago, R., Wenzel, D., Jakobs, S., von Ballmoos, C. & Ott, M. Kinetic coupling of the respiratory chain with ATP synthase, but not proton gradients, drives ATP production in cristae membranes. *Proceedings of the National Academy of Sciences of the United States of America* **117**, 2412–2421 (2020).

36. Rieger, B., Arroum, T., Borowski, M., Villalta, J. & Busch, K. B. Mitochondrial F1 FO ATP synthase determines the local proton motive force at cristae rims. *EMBO reports* **22**, e52727 (2021).

37. Wittig, I., Carrozzo, R., Santorelli, F. M. & Schägger, H. Supercomplexes and subcomplexes of mitochondrial oxidative phosphorylation. *Biochimica et biophysica acta* **1757**, 1066–72 (2006).

937 38. Nübel, E., Wittig, I., Kerscher, S., Brandt, U. & Schägger, H. Two-dimensional native
938 electrophoretic analysis of respiratory supercomplexes from Yarrowia lipolytica.
939 *Proteomics* **9**, 2408–18 (2009).
940 39. Strecker, V., Wumaier, Z., Wittig, I. & Schägger, H. Large pore gels to separate mega
941 protein complexes larger than 10 MDa by blue native electrophoresis: isolation of
942 putative respiratory strings or patches. *Proteomics* **10**, 3379–87 (2010).
943 40. Bultema, J. B., Braun, H.-P., Boekema, E. J. & Kouril, R. Megacomplex organization
944 of the oxidative phosphorylation system by structural analysis of respiratory
945 supercomplexes from potato. *Biochimica et biophysica acta* **1787**, 60–7 (2009).
946 41. Ukolova, I. V., Kondakova, M. A., Kondratov, I. G., Sidorov, A. V., Borovskii, G. B.
947 & Voinikov, V. K. New insights into the organisation of the oxidative phosphorylation
948 system in the example of pea shoot mitochondria. *Biochimica et biophysica acta.*
949 *Bioenergetics* **1861**, 148264 (2020).
950 42. Mühleip, A., Flygaard, R. K., Baradaran, R., Haapanen, O., Gruhl, T., Tobiasson, V.,
951 Maréchal, A., Sharma, V. & Amunts, A. Structural basis of mitochondrial membrane
952 bending by the I-II-III2-IV2 supercomplex. *Nature* **615**, 934–938 (2023).
953 43. Han, F., Hu, Y., Wu, M., He, Z., Tian, H. & Zhou, L. Structures of Tetrahymena
954 thermophila respiratory megacomplexes on the tubular mitochondrial cristae. *Nature*
955 *communications* **14**, 2542 (2023).
956 44. Nesterov, S., Chesnokov, Y., Kamyshinsky, R., Panteleeva, A., Lyamzaev, K.,
957 Vasilov, R. & Yaguzhinsky, L. Ordered Clusters of the Complete Oxidative
958 Phosphorylation System in Cardiac Mitochondria. *International journal of molecular*
959 *sciences* **22**, 1–10 (2021).
960 45. Klatt, S., Simpson, L., Maslov, D. A. & Konthur, Z. Leishmania tarentolae:
961 Taxonomic classification and its application as a promising biotechnological
962 expression host. *PLoS neglected tropical diseases* **13**, e0007424 (2019).
963 46. Akhoundi, M., Kuhls, K., Cannet, A., Votýpka, J., Marty, P., Delaunay, P. & Sereno,
964 D. A Historical Overview of the Classification, Evolution, and Dispersion of

Leishmania Parasites and Sandflies. *PLoS neglected tropical diseases* **10**, e0004349 (2016).

47. Gahura, O., Mühleip, A., Hierro-Yap, C., Panicucci, B., Jain, M., Hollaus, D., Slapničková, M., Zíková, A. & Amunts, A. An ancestral interaction module promotes oligomerization in divergent mitochondrial ATP synthases. *Nature communications* **13**, 5989 (2022).

48. Kaurov, I., Vancová, M., Schimanski, B., Cadena, L. R., Heller, J., Bílý, T., Potěšil, D., Eichenberger, C., Bruce, H., Oeljeklaus, S., Warscheid, B., Zdráhal, Z., Schneider, A., Lukeš, J. & Hashimi, H. The Diverged Trypanosome MICOS Complex as a Hub for Mitochondrial Cristae Shaping and Protein Import. *Current biology : CB* **28**, 3393-3407.e5 (2018).

49. Miranda-Astudillo, H. V., Yadav, K. N. S., Boekema, E. J. & Cardol, P. Supramolecular associations between atypical oxidative phosphorylation complexes of Euglena gracilis. *Journal of bioenergetics and biomembranes* (2021) doi:10.1007/s10863-021-09882-8.

50. Dudkina, N. V., Oostergetel, G. T., Lewejohann, D., Braun, H.-P. & Boekema, E. J. Row-like organization of ATP synthase in intact mitochondria determined by cryo-electron tomography. *Biochimica et biophysica acta* **1797**, 272–7 (2010).

51. Strauss, M., Hofhaus, G., Schröder, R. R. & Kühlbrandt, W. Dimer ribbons of ATP synthase shape the inner mitochondrial membrane. *The EMBO journal* **27**, 1154–60 (2008).

52. Daum, B., Walter, A., Horst, A., Osiewacz, H. D. & Kühlbrandt, W. Age-dependent dissociation of ATP synthase dimers and loss of inner-membrane cristae in mitochondria. *Proceedings of the National Academy of Sciences of the United States of America* **110**, 15301–6 (2013).

53. Blum, T. B., Davies, K. M. & Kühlbrandt, W. Subtomogram averages of mitochondrial ATP synthase dimers from plants show a conserved extra density at the peripheral stalk. *IUCrJ* **12**, 563–569 (2025).

54. Paumard, P., Vaillier, J., Coulary, B., Schaeffer, J., Soubannier, V., Mueller, D. M., Brèthes, D., di Rago, J.-P. & Velours, J. The ATP synthase is involved in generating mitochondrial cristae morphology. *The EMBO journal* **21**, 221–30 (2002).

55. Cogliati, S., Enriquez, J. A. & Scorrano, L. Mitochondrial Cristae: Where Beauty Meets Functionality. *Trends in biochemical sciences* **41**, 261–273 (2016).

56. Evans, D. A. In vitro cultivation and biological cloning of Leishmania. *Methods in molecular biology (Clifton, N.J.)* **21**, 29–41 (1993).

57. Durrieu-Gaillard, S., Sissler, M. & Hashem, Y. Purification of Mitochondrial Ribosomal Complexes from Trypanosoma cruzi and Leishmania tarentolae for Cryo-EM Analysis. *Bio-protocol* **12**, e4425 (2022).

58. de Oliveira Filho, V. A., Garcia, M. S. A., Rosa, L. B., Giorgio, S. & Miguel, D. C. An Overview of Leishmania In Vitro Cultivation and Implications for Antileishmanial Screenings against Promastigotes. *Parasitologia* **4**, 305–318 (2024).

59. Niemann, M. & Schneider, A. A Scalable Purification Method for Mitochondria from Trypanosoma brucei. *Methods in molecular biology (Clifton, N.J.)* **2116**, 611–626 (2020).

60. de Oliveira, T. A., Silva, W. da, da Rocha Torres, N., Badaró de Moraes, J. V., Senra, R. L., de Oliveira Mendes, T. A., Júnior, A. S., Bressan, G. C. & Fietto, J. L. R. Application of the LEXSY Leishmania tarentolae system as a recombinant protein expression platform: A review. *Process Biochemistry* **87**, 164–173 (2019).

61. Sugino, M. & Niimi, T. Expression of Multisubunit Proteins in Leishmania tarentolae. in *Recombinant Gene Expression* vol. 267 317–325 (Humana Press, New Jersey, 2012).

62. Kalef, D. A. Leishmania mexicana recombinant filamentous acid phosphatase as carrier for Toxoplasma gondii surface antigen 1 expression in Leishmania tarentolae. *Journal of parasitic diseases : official organ of the Indian Society for Parasitology* **45**, 1135–1144 (2021).

63. Goes, W. M., Brasil, C. R. F., Reis-Cunha, J. L., Coqueiro-Dos-Santos, A., Grazielle-

Silva, V., de Souza Reis, J., Souto, T. C., Laranjeira-Silva, M. F., Bartholomeu, D. C., Fernandes, A. P. & Teixeira, S. M. R. Complete assembly, annotation of virulence genes and CRISPR editing of the genome of Leishmania amazonensis PH8 strain. *Genomics* **115**, 110661 (2023).

64. Brischigliaro, M., Frigo, E., Fernandez-Vizarra, E., Bernardi, P. & Viscomi, C. Measurement of mitochondrial respiratory chain enzymatic activities in Drosophila melanogaster samples. *STAR protocols* **3**, 101322 (2022).

65. Miyadera, H., Shiomi, K., Ui, H., Yamaguchi, Y., Masuma, R., Tomoda, H., Miyoshi, H., Osanai, A., Kita, K. & Omura, S. Atpenins, potent and specific inhibitors of mitochondrial complex II (succinate-ubiquinone oxidoreductase). *Proceedings of the National Academy of Sciences of the United States of America* **100**, 473–7 (2003).

66. Kiianitsa, K., Solinger, J. A. & Heyer, W.-D. NADH-coupled microplate photometric assay for kinetic studies of ATP-hydrolyzing enzymes with low and high specific activities. *Analytical biochemistry* **321**, 266–71 (2003).

67. Punjani, A., Rubinstein, J. L., Fleet, D. J. & Brubaker, M. A. cryoSPARC: algorithms for rapid unsupervised cryo-EM structure determination. *Nature methods* **14**, 290–296 (2017).

68. Punjani, A., Zhang, H. & Fleet, D. J. Non-uniform refinement: adaptive regularization improves single-particle cryo-EM reconstruction. *Nature methods* **17**, 1214–1221 (2020).

69. Zivanov, J., Nakane, T. & Scheres, S. H. W. Estimation of high-order aberrations and anisotropic magnification from cryo-EM data sets in RELION-3.1. *IUCrJ* **7**, 253–267 (2020).

70. Rubinstein, J. L. & Brubaker, M. A. Alignment of cryo-EM movies of individual particles by optimization of image translations. *Journal of structural biology* **192**, 188–95 (2015).

71. Liebschner, D. *et al.* Macromolecular structure determination using X-rays, neutrons and electrons: recent developments in Phenix. *Acta crystallographica. Section D,*

Structural biology **75**, 861–877 (2019).

72. Liu, Y.-T., Fan, H., Hu, J. J. & Zhou, Z. H. Overcoming the preferred-orientation problem in cryo-EM with self-supervised deep learning. *Nature methods* **22**, 113–123 (2025).

73. Kimanius, D., Dong, L., Sharov, G., Nakane, T. & Scheres, S. H. W. New tools for automated cryo-EM single-particle analysis in RELION-4.0. *The Biochemical journal* **478**, 4169–4185 (2021).

74. Rosenthal, P. B. & Henderson, R. Optimal determination of particle orientation, absolute hand, and contrast loss in single-particle electron cryomicroscopy. *Journal of molecular biology* **333**, 721–45 (2003).

75. Emsley, P., Lohkamp, B., Scott, W. G. & Cowtan, K. Features and development of Coot. *Acta crystallographica. Section D, Biological crystallography* **66**, 486–501 (2010).

76. Goddard, T. D., Huang, C. C., Meng, E. C., Pettersen, E. F., Couch, G. S., Morris, J. H. & Ferrin, T. E. UCSF ChimeraX: Meeting modern challenges in visualization and analysis. *Protein science : a publication of the Protein Society* **27**, 14–25 (2018).

77. Pettersen, E. F., Goddard, T. D., Huang, C. C., Meng, E. C., Couch, G. S., Croll, T. I., Morris, J. H. & Ferrin, T. E. UCSF ChimeraX: Structure visualization for researchers, educators, and developers. *Protein science : a publication of the Protein Society* **30**, 70–82 (2021).

78. Meng, E. C., Goddard, T. D., Pettersen, E. F., Couch, G. S., Pearson, Z. J., Morris, J. H. & Ferrin, T. E. UCSF ChimeraX: Tools for structure building and analysis. *Protein science : a publication of the Protein Society* **32**, e4792 (2023).

79. Sun, F., Huo, X., Zhai, Y., Wang, A., Xu, J., Su, D., Bartlam, M. & Rao, Z. Crystal structure of mitochondrial respiratory membrane protein complex II. *Cell* **121**, 1043–57 (2005).

80. Ho, C.-M., Li, X., Lai, M., Terwilliger, T. C., Beck, J. R., Wohlschlegel, J., Goldberg, D. E., Fitzpatrick, A. W. P. & Zhou, Z. H. Bottom-up structural proteomics: cryoEM

of protein complexes enriched from the cellular milieu. *Nature methods* **17**, 79–85 (2020).

81. Goto, Y., Kuroki, A., Suzuki, K. & Yamagishi, J. Draft Genome Sequence of Leishmania tarentolae Parrot Tar II, Obtained by Single-Molecule Real-Time Sequencing. *Microbiology resource announcements* **9**, 4–5 (2020).

82. Shanmugasundram, A., Starns, D., Böhme, U., Amos, B., Wilkinson, P. A., Harb, O. S., Warrenfeltz, S., Kissinger, J. C., McDowell, M. A., Roos, D. S., Crouch, K. & Jones, A. R. TriTrypDB: An integrated functional genomics resource for kinetoplastida. *PLoS neglected tropical diseases* **17**, e0011058 (2023).

83. Aslett, M. *et al.* TriTrypDB: a functional genomic resource for the Trypanosomatidae. *Nucleic acids research* **38**, D457-62 (2010).

84. Afonine, P. V., Grosse-Kunstleve, R. W., Echols, N., Headd, J. J., Moriarty, N. W., Mustyakimov, M., Terwilliger, T. C., Urzhumtsev, A., Zwart, P. H. & Adams, P. D. Towards automated crystallographic structure refinement with phenix.refine. *Acta crystallographica. Section D, Biological crystallography* **68**, 352–67 (2012).

85. Afonine, P. V., Poon, B. K., Read, R. J., Sobolev, O. V., Terwilliger, T. C., Urzhumtsev, A. & Adams, P. D. Real-space refinement in PHENIX for cryo-EM and crystallography. *Acta crystallographica. Section D, Structural biology* **74**, 531–544 (2018).

86. Abramson, J. *et al.* Accurate structure prediction of biomolecular interactions with AlphaFold 3. *Nature* **630**, 493–500 (2024).

87. Williams, C. J., Headd, J. J., Moriarty, N. W., Prisant, M. G., Videau, L. L., Deis, L. N., Verma, V., Keedy, D. A., Hintze, B. J., Chen, V. B., Jain, S., Lewis, S. M., Arendall, W. B., Snoeyink, J., Adams, P. D., Lovell, S. C., Richardson, J. S. & Richardson, D. C. MolProbity: More and better reference data for improved all-atom structure validation. *Protein science : a publication of the Protein Society* **27**, 293–315 (2018).

88. Wang, C., Ma, C., Xu, Y., Chang, S., Wu, H., Yan, C., Chen, J., Wu, Y., An, S., Xu,

J., Han, Q., Jiang, Y., Jiang, Z., Chu, X., Gao, H., Zhang, X. & Chang, Y. Dynamics of the mammalian pyruvate dehydrogenase complex revealed by in-situ structural analysis. *Nature communications* **16**, 917 (2025).

89. Hagen, W. J. H., Wan, W. & Briggs, J. A. G. Implementation of a cryo-electron tomography tilt-scheme optimized for high resolution subtomogram averaging. *Journal of structural biology* **197**, 191–198 (2017).

90. Tegunov, D. & Cramer, P. Real-time cryo-electron microscopy data preprocessing with Warp. *Nature methods* **16**, 1146–1152 (2019).

91. Chen, M., Dai, W., Sun, S. Y., Jonasch, D., He, C. Y., Schmid, M. F., Chiu, W. & Ludtke, S. J. Convolutional neural networks for automated annotation of cellular cryo-electron tomograms. *Nature methods* **14**, 983–985 (2017).

92. Burt, A., Toader, B., Warshamanage, R., von Kügelgen, A., Pyle, E., Zivanov, J., Kimanius, D., Bharat, T. A. M. & Scheres, S. H. W. An image processing pipeline for electron cryo-tomography in RELION-5. *FEBS open bio* **14**, 1788–1804 (2024).

93. Chaillet, M. L., Roet, S., Veltkamp, R. C. & Förster, F. pytom-match-pick: A tophat-transform constraint for automated classification in template matching. *Journal of structural biology: X* **11**, 100125 (2025).

94. Tegunov, D., Xue, L., Dienemann, C., Cramer, P. & Mahamid, J. Multi-particle cryo-EM refinement with M visualizes ribosome-antibiotic complex at 3.5 Å in cells. *Nature methods* **18**, 186–193 (2021).

95. Roth, P., Ermel, U. H., Moser, D., Arctaedius, G., Wehrheim, M., Scheffer, M. P. & Frangakis, A. S. ArtiaX: geometric models, camera paths and image processing tools. *Journal of structural biology* **217**, 108215 (2025).

96. Lamm, L., Righetto, R. D., Wietrzynski, W., Pöge, M., Martinez-Sanchez, A., Peng, T. & Engel, B. D. MemBrain: A deep learning-aided pipeline for detection of membrane proteins in Cryo-electron tomograms. *Computer methods and programs in biomedicine* **224**, 106990 (2022).

97. Lamm, L., Zufferey, S., Zhang, H., Righetto, R. D., Waltz, F., Wietrzynski, W.,

Yamauchi, K. A., Burt, A., Liu, Y., Martinez-Sanchez, A., Ziegler, S., Isensee, F., Schnabel, J. A., Engel, B. D. & Peng, T. MemBrain v2: an end-to-end tool for the analysis of membranes in cryo-electron tomography. *BioRxiv* at https://doi.org/10.1101/2024.01.05.574336 (2024).

98. Salfer, M., Collado, J. F., Baumeister, W., Fernández-Busnadiego, R. & Martínez-Sánchez, A. Reliable estimation of membrane curvature for cryo-electron tomography. *PLoS computational biology* **16**, e1007962 (2020).

99. Barad, B. A., Medina, M., Fuentes, D., Wiseman, R. L. & Grotjahn, D. A. Quantifying organellar ultrastructure in cryo-electron tomography using a surface morphometrics pipeline. *The Journal of cell biology* **222**, (2023).

Acknowledgements: We thank Shenghai Chang, Lingyun Wu and Tingyu Liu from the Center of Cryo-Electron Microscopy (CCEM), Zhejiang University for technical support with cryo-EM grid vitrification, screening and data collection. We thank Cheng Ma and Liyan Wang from the Core Facilities, Zhejiang University School of Medicine for technical support with protein purification. We also thank Shuimu BioSciences for cryo-EM facility access and technical support with cryo-ET data collection.

Funding: This work was supported by the National Natural Science Foundation of China (32371253 to L.Z.), the National Key Research and Development Program of China (2023YFC2306800 to Y.L.), the National Special Support Program for High-Level Talents of China, Young Top-Notch Talents Program (to L.Z.), the Zhejiang Province Special Support Program for High-Level Talents, Young Talents Program (to L.Z.), the European Research Council grant (ERC805230 to A.A.).

Author contributions: Conceptualization, L.Z.; Methodology: Y.L., L.Z. Investigation, M.W., Z.L., Z.H., H.T., R.Z., F.H., Y.H., J.Z., S.L., A.A., Y.L., L.Z. Writing-original draft, M.W., L.Z. Writing-review and editing, M.W., A.A., Y.L., L.Z. Visualization, M.W., Z.H.,

Y.H., A.A., Y.L., L.Z. Funding acquisition, A.A., Y.L., L.Z. Resources, A.A., Y.L., L.Z. Supervision, L.Z. Project administration, L.Z.

Competing interests: The authors declare no competing interests.

Correspondence and requests for materials should be addressed to Long Zhou.

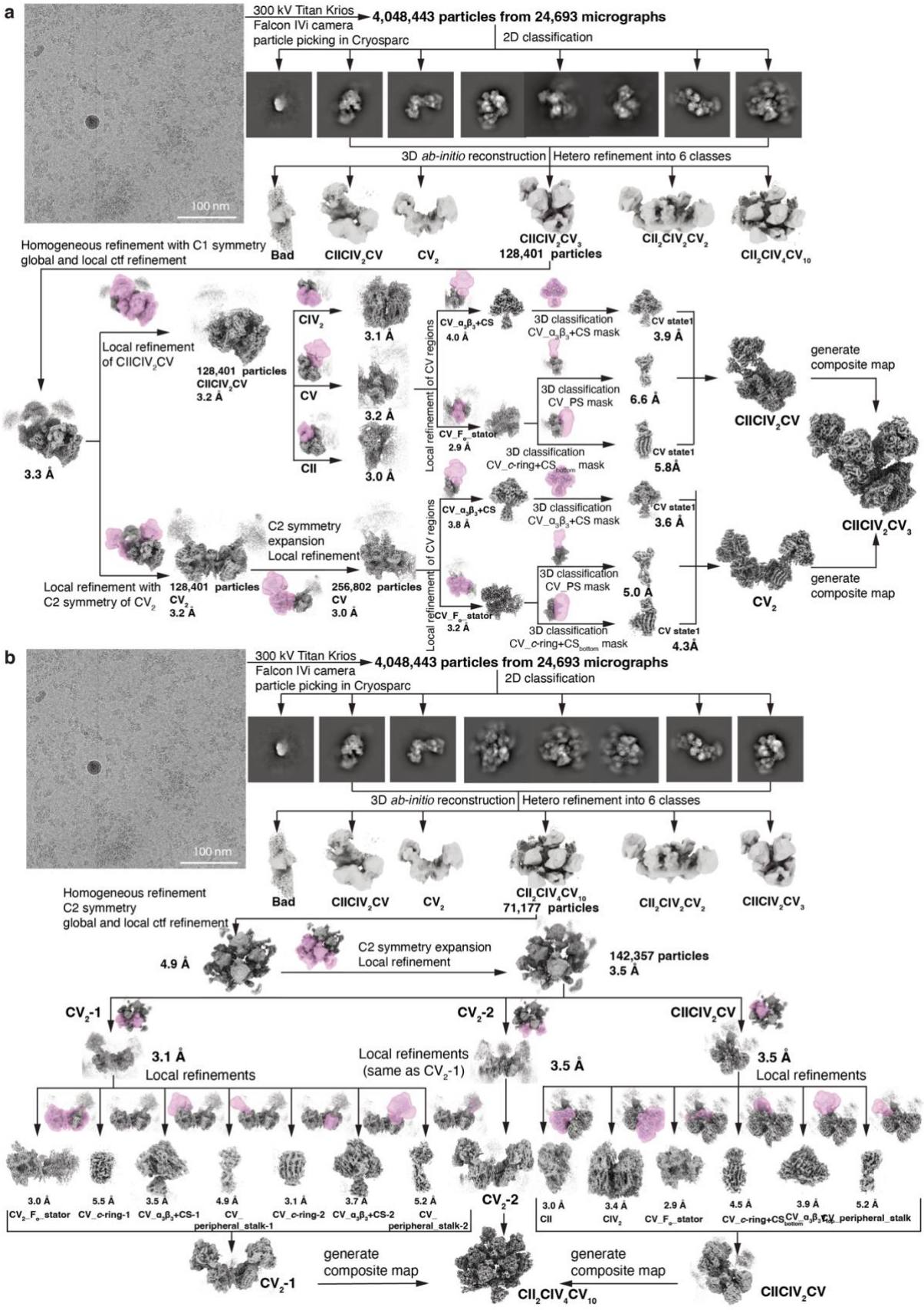

Extended Data Fig. 1 | Cryo-EM image processing of the supercomplexes $CIICIV_2CV_3$ and $CII_2CIV_4CV_{10}$. a, A total of 24,693 micrographs were collected from a 300 kV Titan

Krios microscope equipped with Falcon IVi camera, from which 4,048,443 particles were initially picked and extracted using boxsize 720. A total of 128,401 supercomplex CIICIV$_2$CV$_3$ particles were selected after 2D classification 3D *ab-initio* reconstruction and hetero refinement. Overall refinements yielded a resolution of 3.3 Å. Local refinements of the CIICIV$_2$CV and CV$_2$ regions improved the resolutions to 3.2 Å. For the CIICIV$_2$CV region, after local refinements of CII, CIV$_2$ and CV_F$_o$_stator, local 3D classifications were performed on the CV_PS, CV_α$_3$β$_3$+CS and CV_*c*-ring+CS$_{bottom}$ regions to improve their resolutions and structural features. For CV$_2$ region, initial local refinement after C2 symmetry expansion improved the resolution to 3.0 Å. Direct local refinement only achieved sub-4.0 Å resolution for the CV_F$_o$_stator (3.2 Å). For CV_PS, CV_α$_3$β$_3$+CS and CV_*c*-ring+CS$_{bottom}$, local 3D classifications were performed to improve their resolutions and structural features. Composite maps of CIICIV$_2$CV and CV$_2$ were first respectively generated, before combined into a composite map of the supercomplex CIICIV$_2$CV$_3$. **b,** A total of 24,693 micrographs were collected from a 300 kV Titan Krios microscope equipped with Falcon IVi camera, from which 4,048,443 particles were initially picked and extracted using boxsize 720. A total of 71,177 supercomplex CII$_2$CIV$_4$CV$_{10}$ particles were selected after 2D classification 3D *ab-initio* reconstruction and hetero refinement. Overall refinements yielded a resolution of 4.9 Å and initial local refinement of the asymmetric unit of CIICIV$_2$CV$_5$ after C2 symmetry expansion improved the resolution to 3.5 Å. Local refinements of CIICIV$_2$CV, CV$_2$-1 and CV$_2$-2 regions further improved resolutions to 3.5 Å, 3.1 Å and 3.5 Å, respectively. For each region, more local refinements were performed on all the different regions before composite map generation. Masks used for individual local refinements are indicated as pink transparent surfaces.

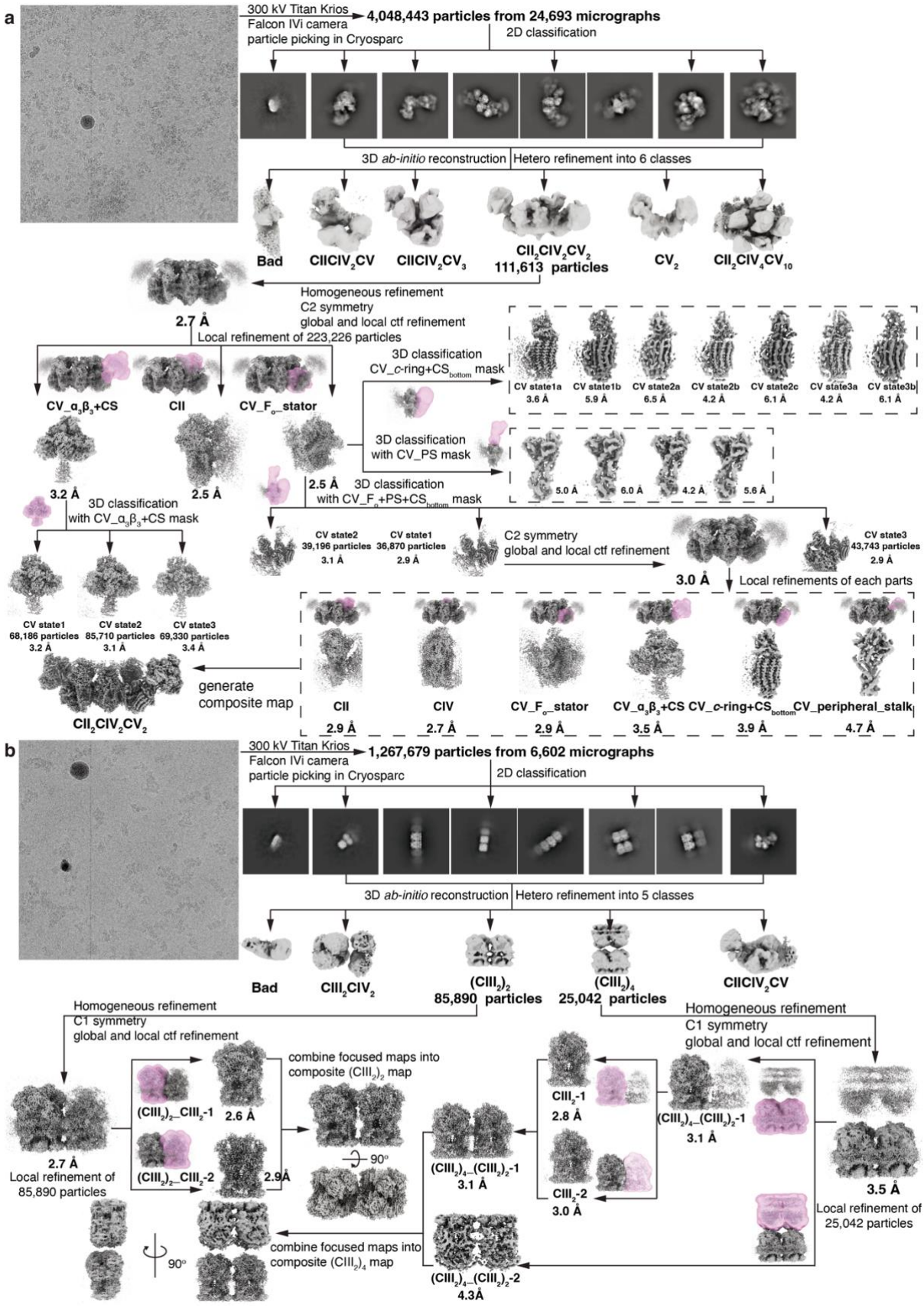

Extended Data Fig. 2 | Cryo-EM image processing of the supercomplexes $CII_2CIV_2CV_2$, $(CIII_2)_2$ and $(CIII_2)_4$. a, A total of 24,693 micrographs were collected from 300 kV Titan

Krios microscope equipped with Falcon IVi camera, from which 4,048,443 particles were initially picked and extracted using boxsize 720. A total of 111,613 supercomplex $CII_2CIV_2CV_2$ particles were selected after 2D classification, 3D *ab-initio* reconstruction and heterogeneous refinement. Overall refinements with C2 symmetry yielded a resolution of 2.7 Å. Local refinements and 3D classifications of F_1's $\alpha_3\beta_3$ and central stalk (CV_$\alpha_3\beta_3$+CS) and the membrane-embedded CV stator (CV_F_o_stator) resolved the three rotational states of CV, albeit with different particle distributions. The 36,870 state 1 particles were used for local refinements of all the different regions of the asymmetric unit of CIICIVCV, followed by composite map generation. Further local 3D classifications and local refinements were performed on the *c*-ring and PS regions to improve the resolutions of the sub-states due to rotation-induced wobbling. **b,** A total of 6,602 micrographs were collected in the $CIII_2$-containing supercomplex dataset and 1,267,679 particles were initially picked and extracted using boxsize 720. A total of 85,890 $(CIII_2)_2$ and 25,042 $(CIII_2)_4$ particles were selected after 2D classification and multi-class 3D *ab-initio* reconstruction. Overall refinements yielded resolutions of 2.7 Å and 3.5 Å for $(CIII_2)_2$ and $(CIII_2)_4$ respectively. For both classes, local refinements of all the $CIII_2$ regions were performed, before respective composite map generation. Masks used for individual local refinements are indicated as pink transparent surfaces.

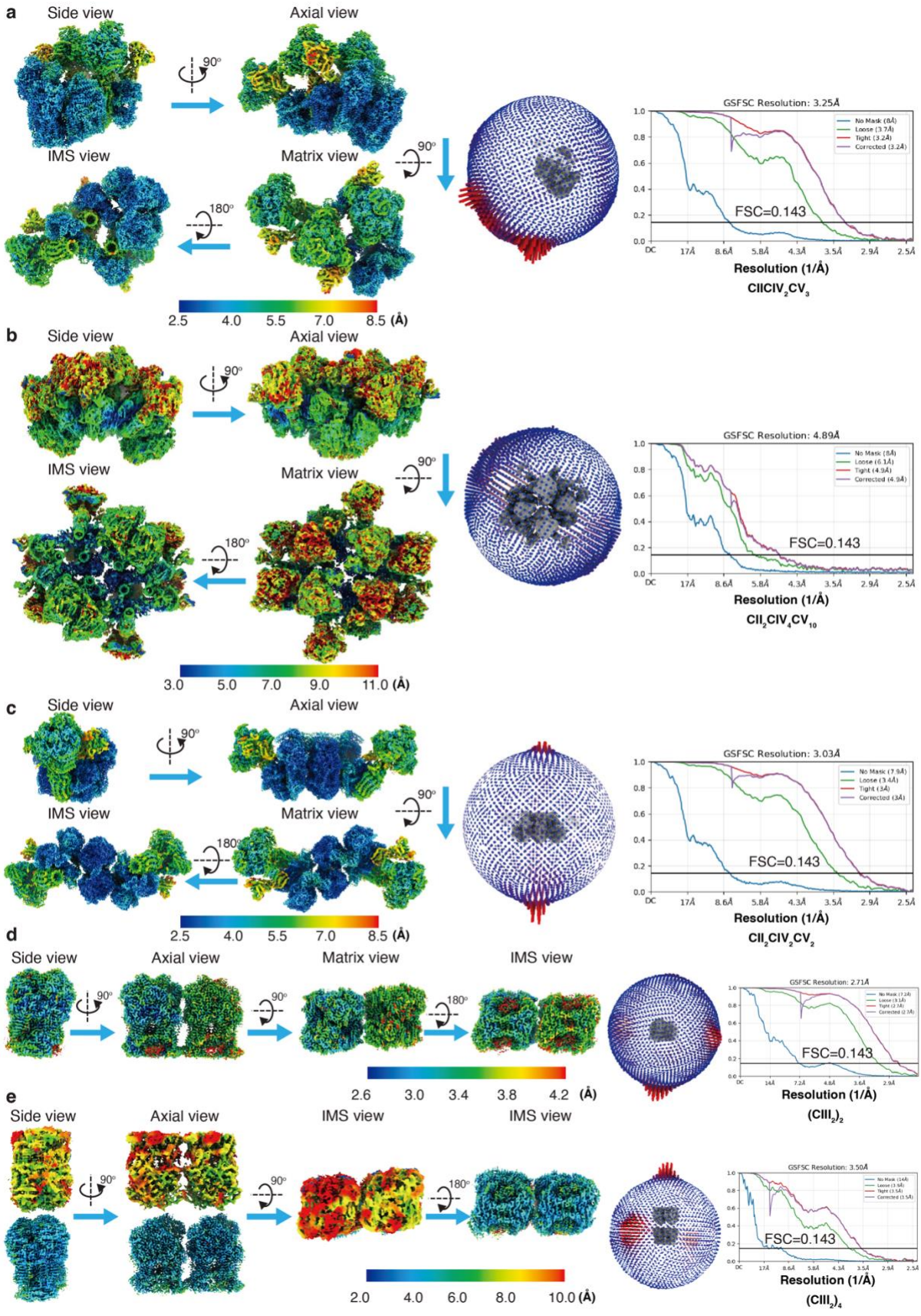

Extended Data Fig. 3 | Local resolution maps, projection orientation distributions and Fourier shell correlation (FSC) curves of $CIICIV_2CV_3$, $CII_2CIV_4CV_{10}$, $CII_2CIV_2CV_2$,

$(CIII_2)_2$ and $(CIII_2)_4$. a-e, Local resolutions are plotted on the composite maps of $CIICIV_2CV_3$ (**a**), $CII_2CIV_4CV_{10}$ (**b**), $CII_2CIV_2CV_2$ (**c**), $(CIII_2)_2$ (**d**), $(CIII_2)_4$ (**e**) in different viewing directions. Orientational distributions of particle projections are individually plotted. FSC curves (gold standard FSC=0.143 for resolution estimation) of the corresponding consensus refinements are shown.

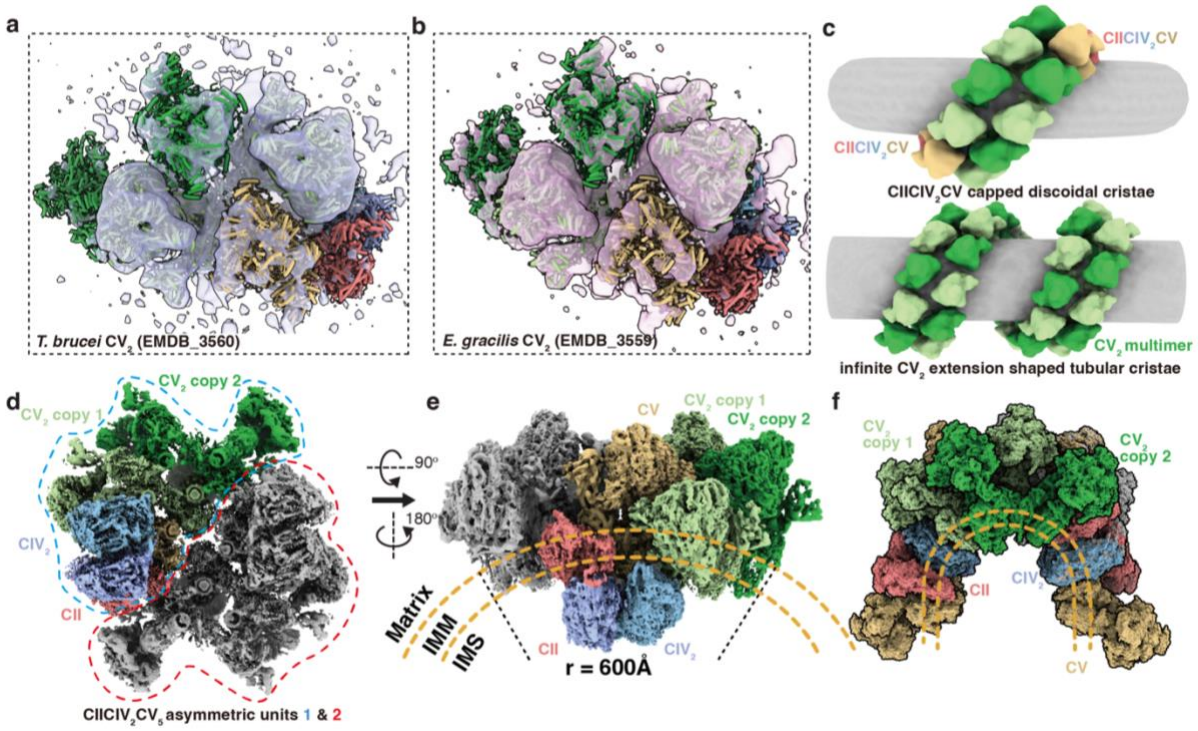

Extended Data Fig. 4 | Additional structural characteristics of *L. tarentolae* supercomplexes. a,b, Rigid body docking of the CV_4 portion of $CII_2CIV_4CV_{10}$ into the cryo-ET maps (transparent surfaces) of *T. brucei* (**a**) and *E. gracilis* (**b**) CV_2 with EMDB IDs labelled. **c,** The normal discoidal cristae shaped by $CIICIV_2CV$ endpieces capped $(CV_2)_4$ rows (top panel) and the aberrant tubular cristae shaped by CV_2 rows without the length constraints of $CIICIV_2CV$ endpieces (bottom panel). **d,** The IMS view of the cryo-EM map of $CII_2CIV_4CV_{10}$, with one asymmetric unit colored as in Fig. 1 and the other asymmetric unit colored gray. **e,** The perpendicular-to-cristae discoid view of the cryo-EM map of $CII_2CIV_4CV_{10}$. Cristae circumference and estimated radius are labelled. **f,** A putative model of the more complete *L. tarentolae* cristae edge OXPHOS architecture. Two $CII_2CIV_2CV_2$ supercomplexes are concatenated to the two $CIICIV_2CV$ endpieces to adapt to the transition to the flatter membrane at more central positions.

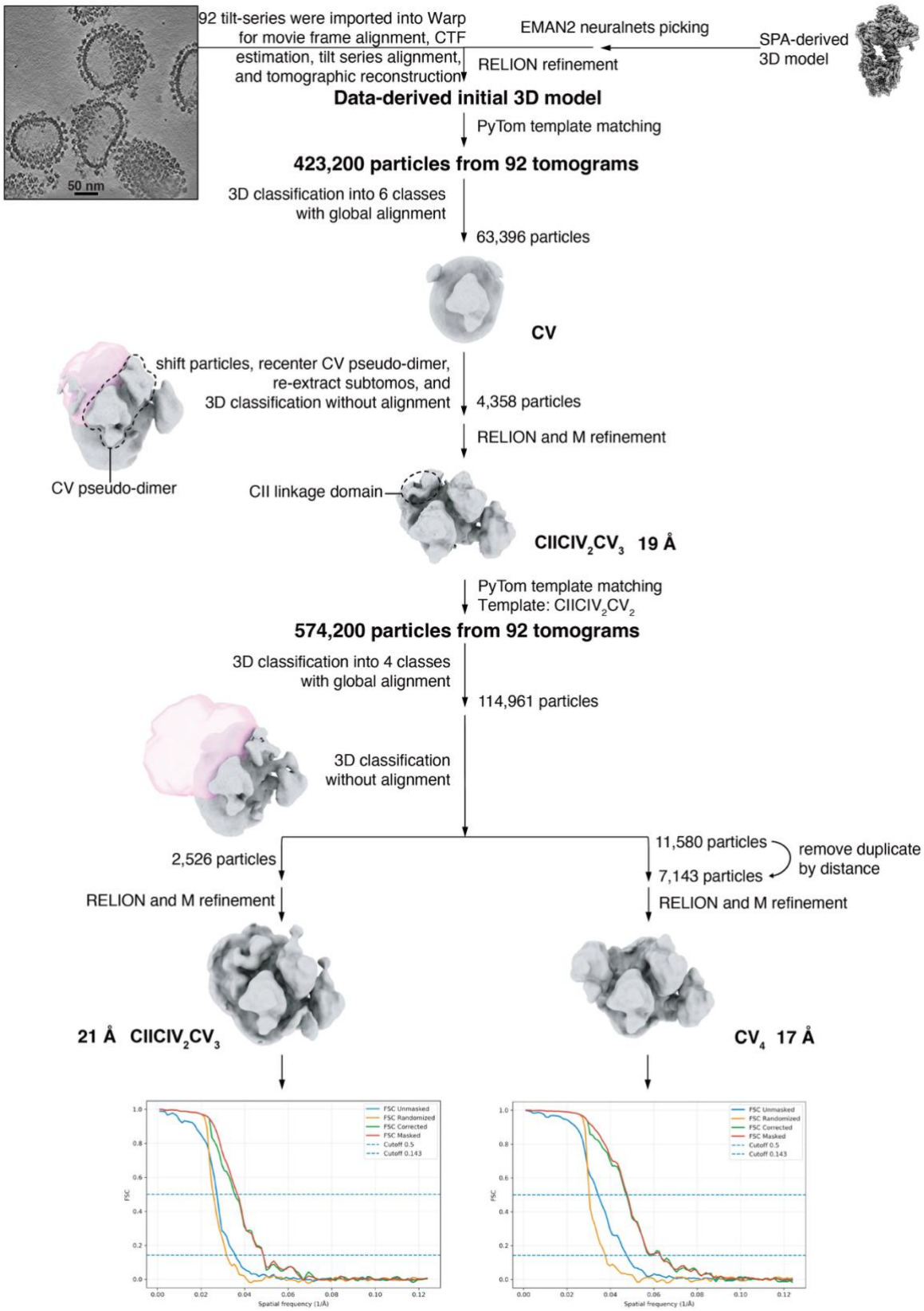

Extended Data Fig. 5 | Cryo-ET STA processing of CIICIV$_2$CV$_3$ and CV$_4$. A total of 92 tomograms were reconstructed in Warp, followed by particle picking in EMAN2 using cryo-EM SPA-derived CV model. Picked subtomograms were extracted in Warp and exported to RELION for initial CV refinement. The resulting CV STA was used as a template for

template matching-based particle picking in PyTom. The particles were again exported to RELION for 3D classification with global alignment to isolate the CV-containing particles. The subsequent refinement resulted in a CV trimer STA, the pseudo-CV dimer (dashed circle) portion of which was used as the center for particles re-extraction. 3D classification masking the proposed region of $CIICIV_2$ next to the pseudo-CV dimer isolated the $CIICIV_2CV_3$ class. A further round of refinement, template matching-based particle picking and classification cleaned this class, leading to a final $CIICIV_2CV_3$ resolution of 21 Å. The associated CV_4 class refined to a final resolution of 17 Å. Both resolutions were determined by gold-standard FSC curves. Masks used for local refinements are shown as pink transparent surfaces.

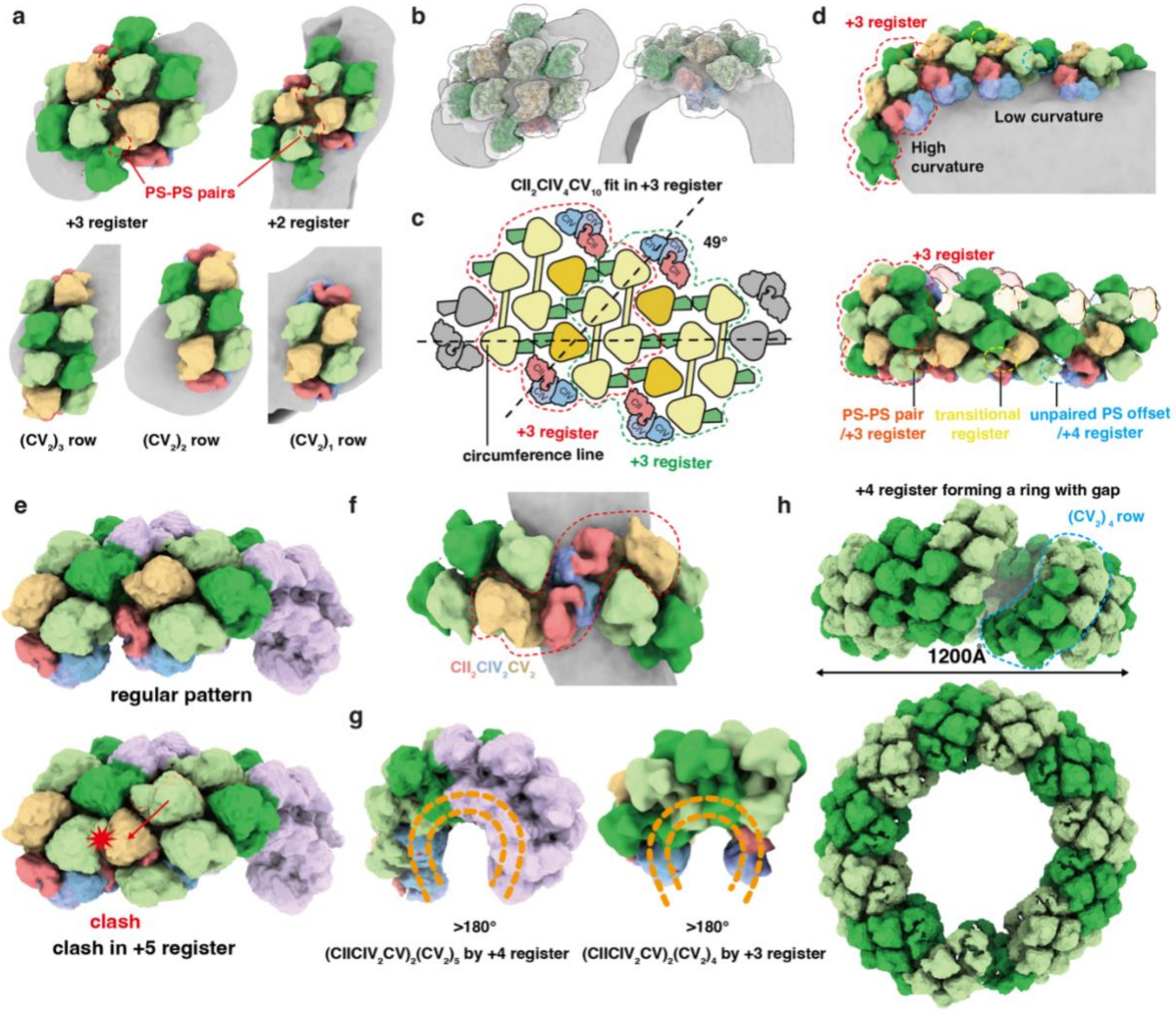

Extended Data Fig. 6 | Anomalies in *L. tarentolae*'s long range OXPHOS array. a, Examples of different copy numbers of CV_2 in $CIICIV_2CV$-capped CV_2 rows and different registers between adjacent rows. **b,** Docking of the cryo-EM structure of $CII_2CIV_4CV_{10}$ (cylindrical cartoons) into its cryo-ET map (transparent surface). **c,** Cartoon representation of the proposed +3 register with two potential $CII_2CIV_4CV_{10}$ structures circled by red and green dashes. Extrapolated complexes are shown in gray. **d,** The tomographic example of register transition from +3 (red circle) to +4, adapting to a high-to-low membrane curvature gradient. The register-defining terminal PS-PS pair (orange circle), unpaired PS offset (blue circle) and a transitional status (yellow circle) are respectively circled and labelled. Extrapolated ETC and CV complexes based on the register rule, but not observed by cryo-ET, are shown as transparent surfaces. **e,** Potential steric clash (red star) when artificially extending the $(CIICIV_2CV)_2(CV_2)_4$ assembly in its regular arrangement (top panel) to $(CIICIV_2CV)_2(CV_2)_5$ (bottom panel). **f,** The tomographic example of $CII_2CIV_2CV_2$. **g,** The over-180° edge-curving leading to biconcave-shaped cristae by aligning $(CIICIV_2CV)_2(CV_2)_5$ with +4 register (left panel) or $(CIICIV_2CV)_2(CV_2)_4$ with +3 registers (right panel). The lipid bilayer is traced by orange dashes. **h,** The shallow helical structure formed by artificially aligning $(CIICIV_2CV)_2(CV_2)_4$ by the normal +4 register to over 360°. The discoidal diameter is in line with published estimates but the OXPHOS ring cannot self-enclose.

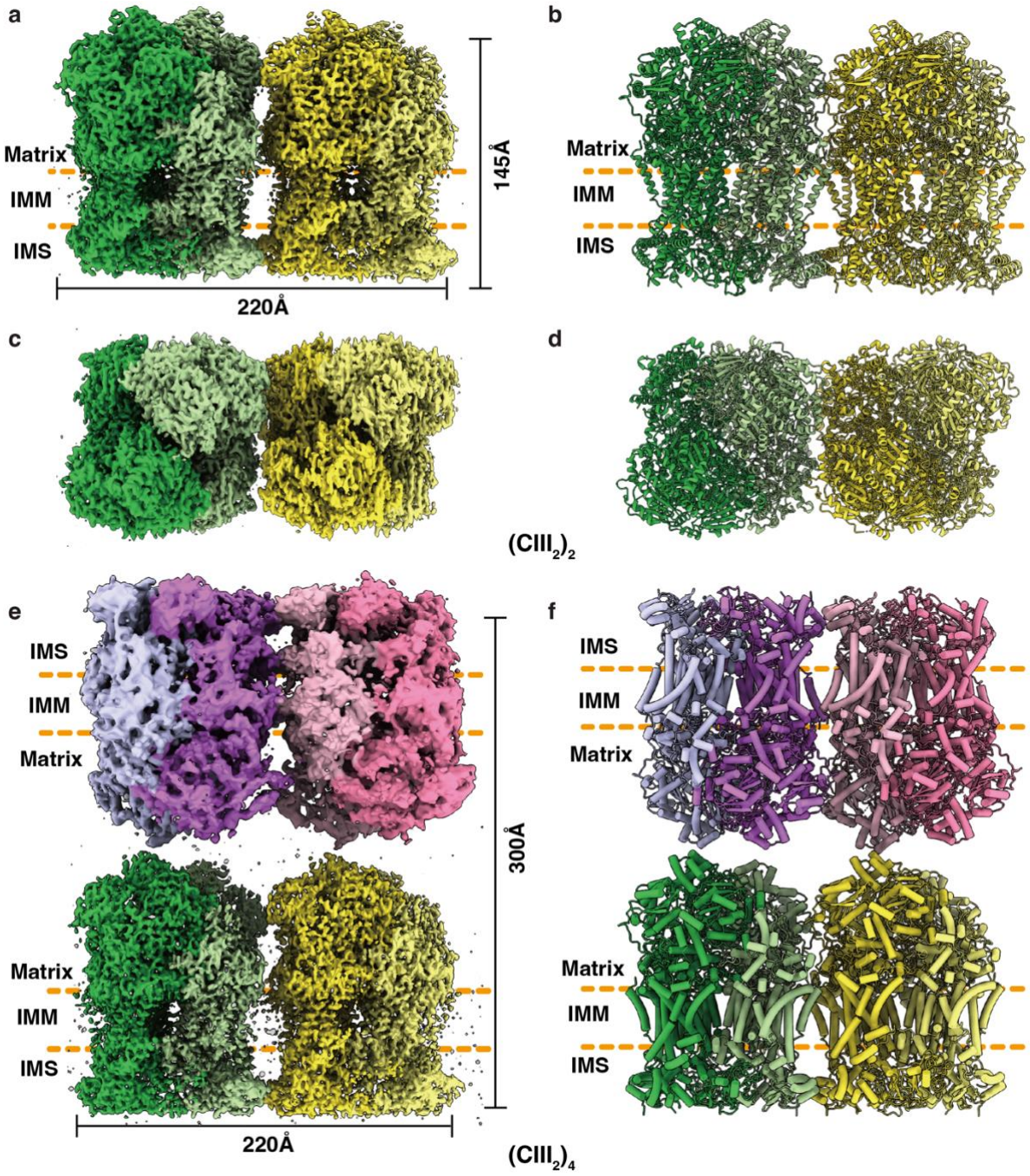

Extended Data Fig. 7 | Structures of supercomplexes $(CIII_2)_2$ and $(CIII_2)_4$. a-d, Side views (**a,b**) and matrix views (**c,d**) of $(CIII_2)_2$. **e,f,** Side views of $(CIII_2)_4$. The cryo-EM maps (**a,c,e**) and structural models (**b,d,f**) are shown with dimensions labelled.

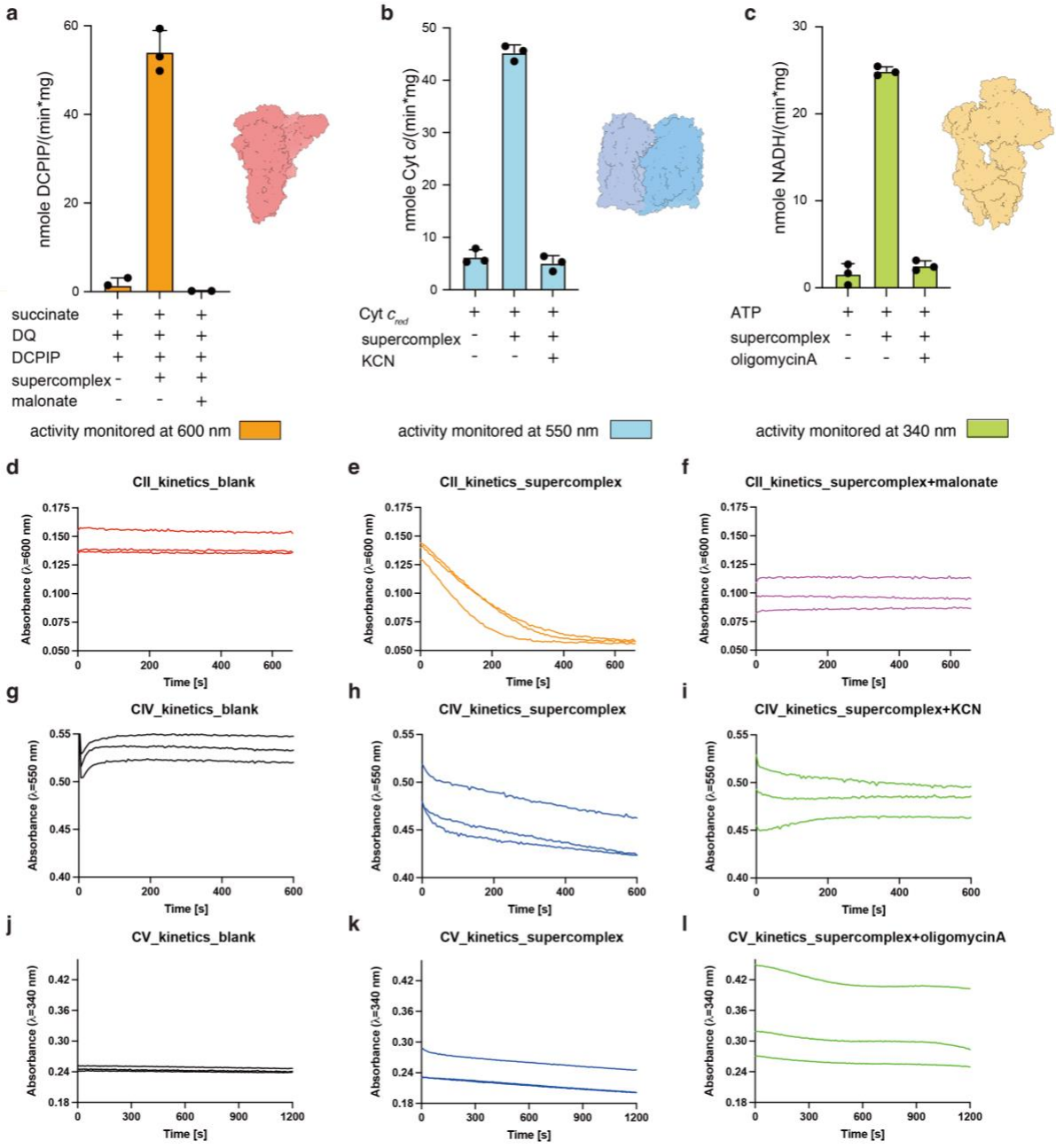

Extended Data Fig. 8 | Catalytic activities of CII, CIV and CV. a-c, Spectroscopic assays of CII (**a**), CIV (**b**) and CV (**c**) activities of the cryo-EM sample for the ETC-CV dataset. The activities were monitored by DQ reduction coupled DCPIP reduction at 600 nm for CII, reduced cyt *c* oxidation at 550 nm for CIV and ADP production coupled NADH oxidation at 340 nm for CV, in the presence of absence of respective inhibitors of malonate (CII), KCN (CIV) and oligomycin A (CV). **d-l,** The kinetic curves for CII (**d-f**), CIV (**g-i**) and CV (**j-l**) activities under blank (**d,g,j**), substrate (**e,h,k**) and inhibitor (**f,i,l**) conditions. Data in (**a-c**) are presented as mean values ± standard error of mean (SEM). Data lines in (**d-l**) represent individual replicates. n=3 biologically independent activity experiments.

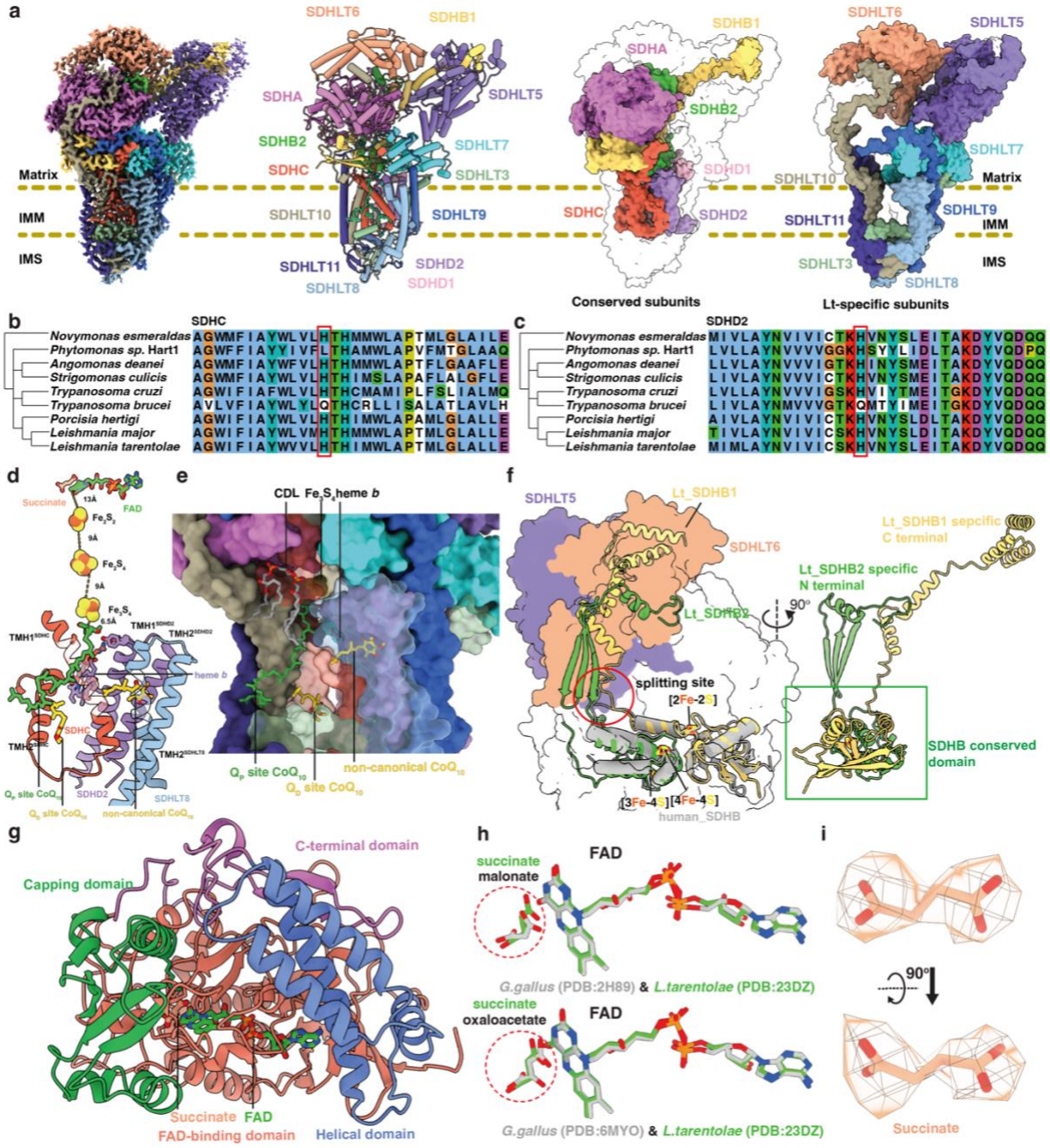

Extended Data Fig. 9 | Structural details of *L. tarentolae* CII. a, From left to right: cryo-EM map, structure (cartoons) colored by individual subunits, core and lineage-specific subunits (solid surfaces) colored individually, on top of the silhouette of complete CII. **b,c,** Sequence alignments of the SDHC's and SDHD2's trans-membrane helices 2 ($TMH2^{SDHC}$ and $TMH2^{SDHD2}$) of *L. tarentolae*, *L. major*, *P. hertigi*, *T. brucei*, *T. cruzi*, *S. culicis*, *A. deanei*, *Phytomonas.Hart1*, *N. esmeraldas*, highlighting the positions of heme-coordinating histidines (red boxes). **d,** Co-factors, key lipids and CoQ_{10} in CII. FeS clusters are shown as spheres; FAD, CoQ_{10}, bound lipids are shown as sticks and nearby TMHs are shown as cartoons. Distances between key electron transfer co-factors are labeled. **e,** The three CoQ_{10} molecules bound in CII. Trans-membrane subunits are shown as surfaces and colored individually. Some surfaces are shown in transparency to allow visualization of elements behind. **f,**

Structural superposition of *L. tarentolae* SDHB1 (yellow) and SDHB2 (green) with human SDHB (PDB: 8GS8, grey), illustrating the C-terminal and N-terminal extension of *L. tarentolae* SDHB1 and SDHB2 towards the CII linkage domain of SDHLT5 (purple) and SDHLT6 (orange). **g,** Overview of the domain organization of CII's hydrophilic SDHA subunit. The covalently bound FAD and the built succinate nearby are shown as sticks. **h,** Structural superposition of our FAD-succinate combination (green stick) with published *Gallus gallus* CII structures with malonate and oxaloacetate bound (gray stick). The substrate/inhibitor hotspot is circled (red dash). **i,** The natural substrate/inhibitor density (orange mesh), tentatively model as succinate (orange sticks), in our *L. tarentolae* CII.

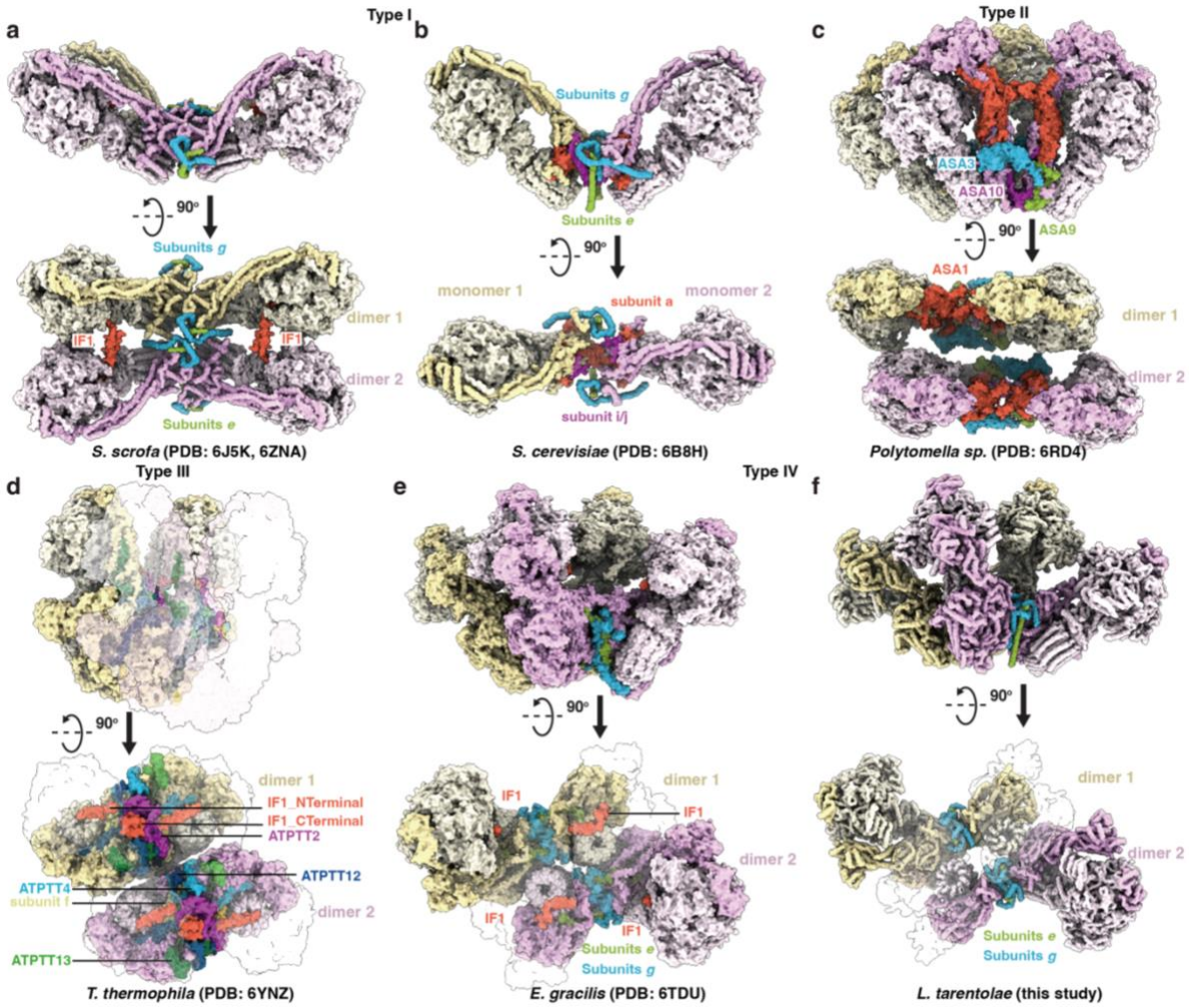

Extended Data Fig. 10 | Comparison of CV dimerization and tetramerization across species. a, Porcine, **b,** yeast, **c,** green alga, **d,** ciliate, **e,** euglenid and **f,** trypanosomatid ATP synthase dimer/tetramer side views (top panels) and top views (bottom panels). Stators of all CVs are highlighted by yellow and pink colors. Common multimerization subunits, such as the subunit *e*, *g* and IF_1 are shown in green, blue and orange-red. Other species-specific multimerization subunits are also individually colored and labelled. For (**d-f**), the front CV_2 or certain F_1 regions are shown in transparency for clarity of the structural elements below. The species and corresponding PDB IDs of the structural models used are also labelled.

Title: How respiratory complexes and ATP synthase co-assemble to build cristae

Authors: Mengchen Wu[1]†, Zhongqiu Li[2]†, Zhuru Hou[3]†, Hongtao Tian[1], Ruizhe Zhang[1], Fangzhu Han[1], Yiqi Hu[1], Jiancang Zhou[4], Shizhu Li[2], Alexey Amunts[5,6]*, Yue Liu[3]*, Long Zhou[1]*

Affiliations:

[1]Department of Biophysics and Department of Critical Care Medicine of Sir Run Run Shaw Hospital, Zhejiang University School of Medicine, Hangzhou, China.
[2]National Institute of Parasitic Diseases, Chinese Center for Disease Control and Prevention (Chinese Center for Tropical Diseases Research); NHC Key Laboratory of Parasite and Vector Biology, National Key Laboratory of Intelligent Tracking and Forecasting for Infectious Diseases, Shanghai, China.
[3]Department of Microbiology and State Key Laboratory for Diagnosis and Treatment of Infectious Diseases of the First Affiliated Hospital, Zhejiang University School of Medicine, Hangzhou, China.
[4]Department of Critical Care Medicine of Sir Run Run Shaw Hospital, Zhejiang University School of Medicine, Hangzhou, China.
[5]University of Münster, Schlossplatz 8, Münster, Germany.
[6]Institute of Bio-Architecture and Bio-Interactions, Shenzhen Medical Academy of Research and Translation, Shenzhen, Guangdong 518107, China.

*Corresponding author. Email: alexey.amunts@gmail.com, yuel@zju.edu.cn, longzhou@zju.edu.cn
†These authors contributed equally to this work.

Supplementary Information contents:

Supplementary Discussion

Structural details of L. tarentolae's divergent CII

Spectroscopic assays confirmed the presence of electron transport and ATP hydrolytic activities of individual OXPHOS complexes in our cryo-EM sample (Extended Data Fig. 8). Out of these complexes, CII is structurally most divergent as exemplified by its split core subunits SDHB and SDHD (SDHB/D1 and 2)[48] and the innovation of hydrophilic linkage domain that substantially stabilizes its association with CIV_2 (Extended Data Fig. 9a,f). Unlike CII of other protists such as *Tetrahymena thermophila*[25,49] and *Perkinsus marinus*[50], a membrane-embedded *b*-type heme is identified between subunits SDHC and SDHD2 of *L. tarentolae* CII, making it more similar to the canonical opisthokont CIIs in this regard[24,51–54] (Extended Data Fig. 9d). This heme *b*, not absolutely required for CII's redox activity[51], is not universally present among kinetoplastid species. For example, *T. brucei* has lost both heme *b* coordinating histidines as revealed by sequence alignments of subunits SDHC and SDHD2 (Extended Data Fig. 9b,c).

A total of three ubiquinone/coenzyme Q_{10} (CoQ_{10}) are identified, one at the classic redox site below the Fe_3S_4 cluster and the other two at non-canonical positions among the trans-membrane helices of subunits SDHC, SDHD2 and SDHLT8, likely representing local energy minimums *en route* of CoQ_{10} movement[49,55] (Extended Data Fig. 9d,e). In terms of electron donor, density resembling dicarboxylate molecule, tentatively modeled as succinate here, is observed next to the covalently bound FAD, a position known to be occupied by catalytic intermediate and competitive inhibitors such as malonate[53] and oxaloacetate[56,57] (Extended Data Fig. 9g-i). In general, instead of providing new catalytic functions and/or mechanisms, new structural features of *L. tarentolae* CII contribute more to its firm integration into the supercomplex $CIICIV_2CV$.

Dimerization and tetramerization of CV across species

The *L. tarentolae* CV_4 within supercomplex $CII_2CIV_4CV_{10}$ lead us to review structural

innovations used by different eukaryotes to dimerize and tetramerize CV (Extended Data Fig. 10). While the same *g*/*g* module is employed by CV_2 of the free-living discobid *E. gracilis*[58] (Extended Data Fig. 10e), in yeasts, such purpose is fulfilled by lineage-specific loops/extensions of subunits *a* and *i*/*j*[59] (Extended Data Fig. 10b). In mammals, within a CV_4, the *g*/*g* module dimerizes two diagonal CV monomers, while dimerization of the C-terminal helices of the native inhibitory factor IF_1 links two parallel dimers[60] (Extended Data Fig. 10a). In this way, although limited interactions are found within CV_2, it is stabilized by the external tetrameric scaffold. Alveolates such as the *T. thermophila* have the most elaborated dimer interface of CV, containing both homotypic and heterotypic interactions scattered throughout the matrix, intra-membrane and IMS levels[61] (Extended Data Fig. 10d). Among these, a symmetry breaking subunit ATPTT2 binds C-terminal regions of two IF_1 copies to stabilize the dimer. In green algae, an additional interaction site is found between the two bulky peripheral stalks, in the F_1 region[62,63] (Extended Data Fig. 10c). In general, the evolutionary convergence, reflected by the diverse strategies found across the eukaryotic tree of life towards the same goal of CV multimerization, underscores its critical role in maintaining the morphological and functional integrity of mitochondria.

In-situ relevance of the cryo-ET sample

While cryo-focused ion beam (cryo-FIB) milling[64,65] was not employed in our cryo-ET sample preparation, the resulting STA mapped tomograms still adequately captured the physiological landscape of OXPHOS assembly. For example, the fact that the distinct protocols of cryo-EM[25,26,49,60,66,67] and cryo-ET[25,36,68–78] converge on the same structure of supercomplex $CII_2CIV_4CV_{10}$ indicates its genuine presence on the *L. tarentolae* cristae (Fig. 1a, Extended Data Fig. 6a,b). The corresponding fragmentation of the more common +4 register, namely a $CII_2CIV_4CV_{14}$ supercomplex, does not appear in our cryo-EM dataset likely due to its sheer size and fragility under detergent conditions (Fig. 4d). This again validates the power of *in situ* structural biology in revealing long range, membrane-bound supramolecular machineries such as the OXPHOS system[63,78–81]. Moreover, no cristae

completely encircled by the $(CIICIV_2CV)_2(CV_2)_4$ assemblies with the regular +4 register is found. This is in line with the native situation that cristae are connected to the inner boundary membrane (IBM) via cristae junctions, where the mitochondrial contact site and cristae organizing system (MICOS) are hosted instead of the OXPHOS complexes[82] (Fig. 4a). Actually, instead of a perfectly planar circle, a helix with very shallow pitch is formed when trying to artificially reconstruct a self-enclosed $(CIICIV_2CV)_2(CV_2)_4$ belt, which is structurally not adaptable by the junction-linked discoidal cristae (Extended Data Fig. 6h).

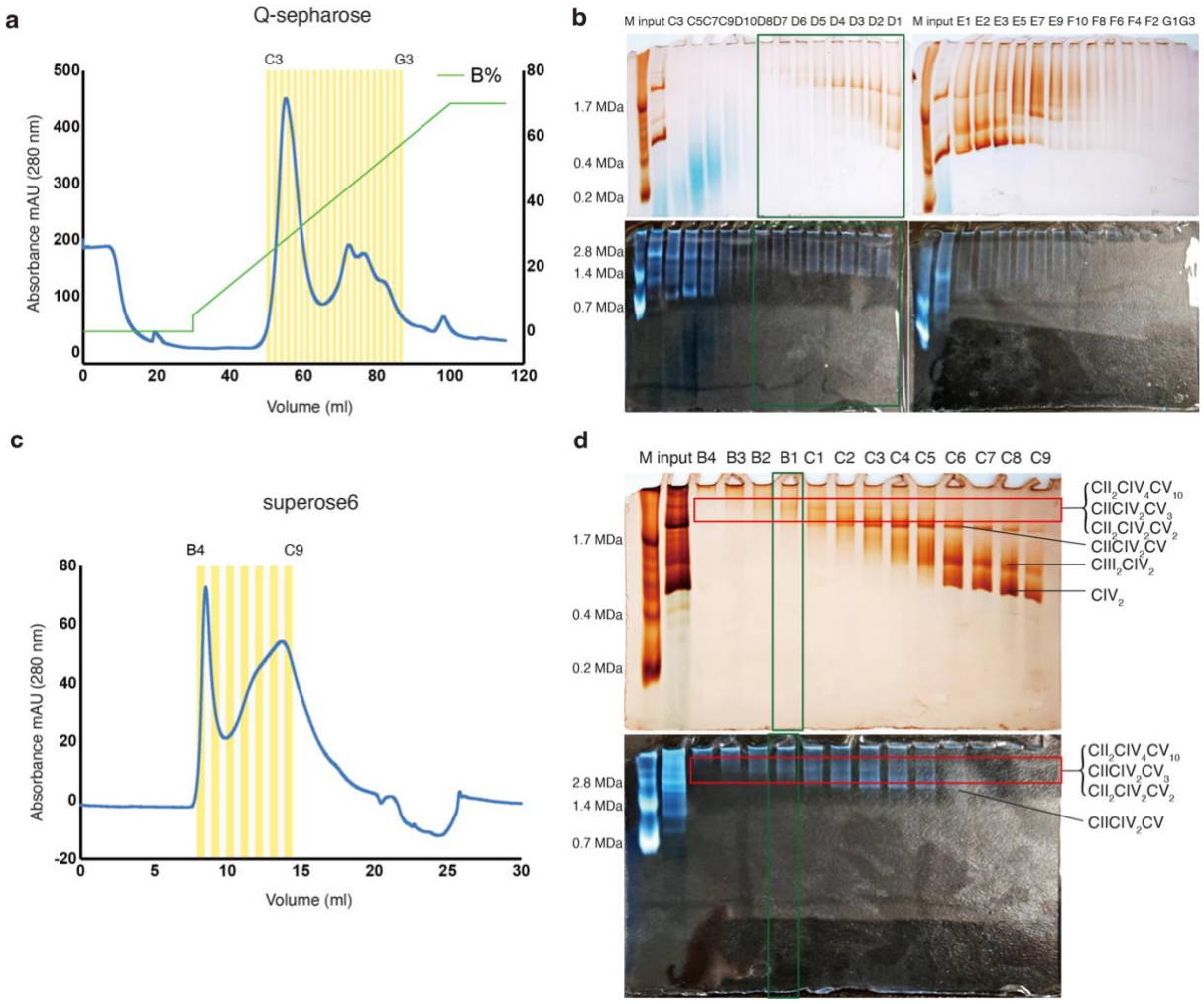

Supplementary Fig. 1 | Purification of *L. tarentolae* ETC-CV supercomplexes. a,b, Q-Sepharose ANX chromatogram (**a**) and the corresponding BN-PAGE (**b**). The CIICIV$_2$CV-containing fractions D9 to D1, indicated by the green boxes, are pooled, concentrated and used for subsequent SEC chromatography. **c,d,** Superose 6 SEC chromatogram (**d**) and the corresponding BN-PAGE (**d**), using the CIICIV$_2$CV-containing fractions from (**b**). The fraction directly used for cryo-EM grid vitrification is indicated by the green boxes. BN-PAGE gels in (**b**) and (**d**) are stained by CV (white bands) or CIV (dark orange bands) in-gel activities. The 'M' lane indicates porcine respiratory supercomplexes used as the MW marker. The 'input' lane indicates the protein samples used for ANX and SEC chromatography loading.

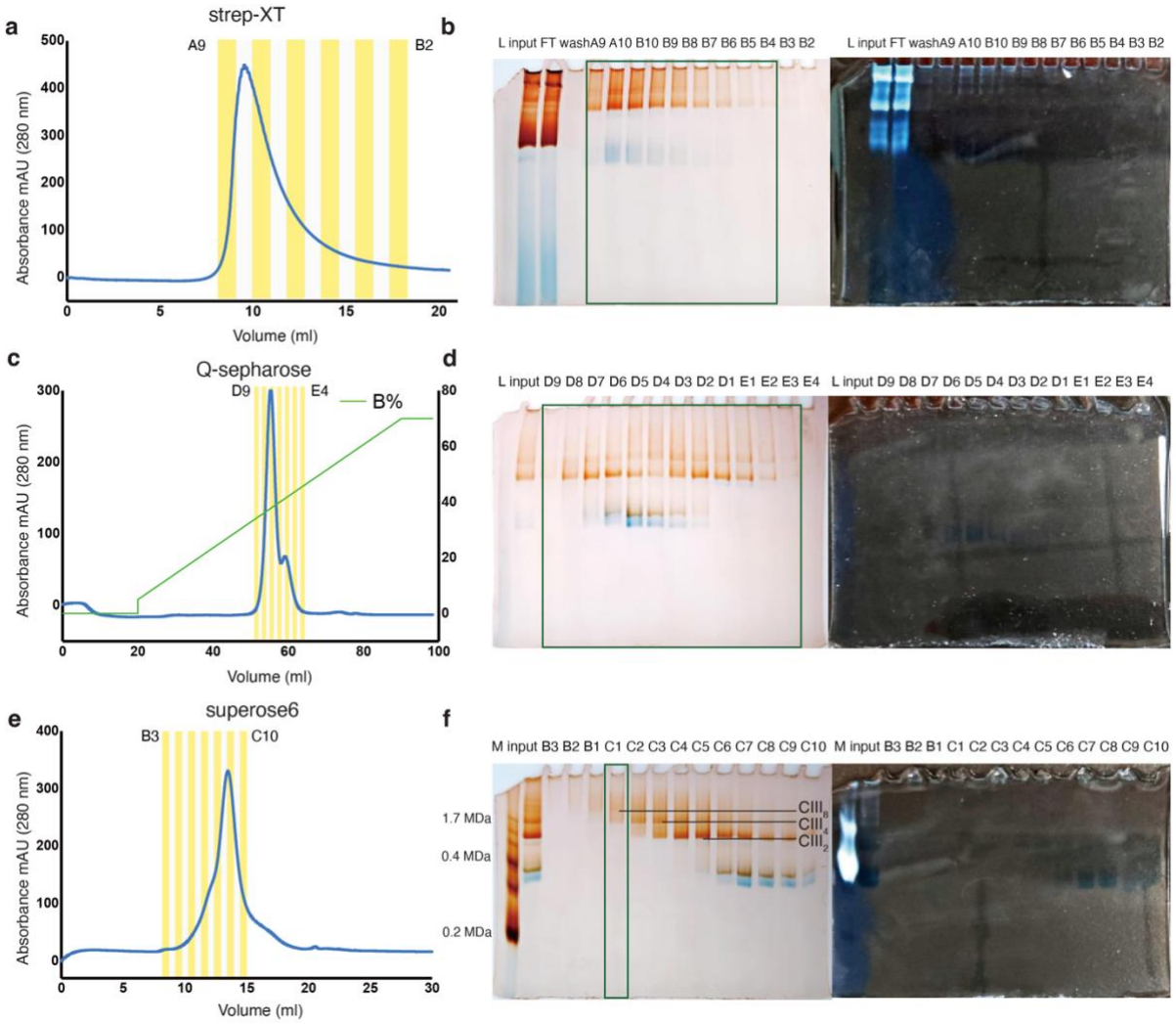

Supplementary Fig. 2 | Purification of $CIII_2$-containing supercomplexes of *L. tarentolae*. **a,b,** StrepTrap XT affinity chromatogram (**a**) and the corresponding BN-PAGE (**b**). The eluted peak fractions with CIV activity, indicated by the green boxes, are pooled, concentrated and used for subsequent ANX chromatography. **c,d,** Q-Sepharose ANX chromatogram (**c**) and the corresponding BN-PAGE (**d**). The fractions with CIV activity, indicated by the green boxes, are pooled, concentrated and used for subsequent SEC chromatography. **e,f,** Superose 6 SEC chromatogram (**e**) and the corresponding BN-PAGE (**f**), using the $CIII_2$-containing fractions D9-E3 from (**d**). The fraction directly used for cryo-EM grid vitrification is indicated by the green box. BN-PAGE gels in panels (**b**), (**d**) and (**f**) are stained by CV (white bands) or CIV (dark orange bands) in-gel activities. The 'L' lane indicates the loading buffer used for blank. The 'M' lane indicates porcine respiratory supercomplexes used as the MW marker. The 'input' lane indicates the protein samples used for affinity, ANX and SEC chromatography loading. The 'FT' and 'wash' lanes indicate the flow-through and washed off non-specific proteins from the affinity chromatography.

Supplementary Tables

Supplementary Table 1 | Cryo-EM data collection, image processing and model validation of supercomplexes $CII_2CIV_2CV_2$, $CIICIV_2CV_3$ and $CII_2CIV_4CV_{10}$

	$CII_2CIV_2CV_2$ (EMDB-67545) (PDB 21BE)		$CIICIV_2CV_3$ (EMDB-67546) (PDB 21BF)		$CII_2CIV_4CV_{10}$ (EMDB-67544) (PDB 21BD)	
Magnification	105,000					
Voltage (kV)	300					
Electron exposure ($e^-/Å^2$)	45.00					
Defocus range (μm)	-0.8 to -2.0					
Pixel size (Å)	1.20					
Symmetry imposed	C2		C1		C2	
Micrographs No.	24,693					
Initial particle No.	4,048,443					
Final particle No.	111,613		128,401		71,177	
Map resolutions (Å)	CII	2.9	CII	3.0	CII	3.0
FSC threshold 0.143	CIV	2.7	CIV_2	3.1	CIV_2	3.4
	CV_F_o_stator	2.9	CV_F_o_stator	2.9	CV_F_o_stator	2.9
	CV_$\alpha_3\beta_3$+CS	3.5	CV_$\alpha_3\beta_3$+CS	3.9	CV_$\alpha_3\beta_3\gamma_{top}$	3.9
	CV_*c*-ring+CS_{bottom}	3.9	CV_*c*-ring+CS_{bottom}	5.8	CV_*c*-ring+CS_{bottom}	4.5
	CV_PS	4.7	CV_PS	6.6	CV_PS	5.2
			CV_2_F_o_stator	3.2	CV_2_F_o_stator	3.0
			CV_2_$\alpha_3\beta_3$+CS	3.6	CV_2_$\alpha_3\beta_3$+CS-1	3.5
			CV_2_*c*-ring+CS_{bottom}	4.3	CV_2_*c*-ring-1	5.5
			CV_2_PS	5.0	CV_2_PS-1	4.9
					CV_2_$\alpha_3\beta_3$+CS-2	3.7
					CV_2_*c*-ring-2	3.1
					CV_2_PS-2	5.2
Initial models used	8APA		8APA		8APA	
Model resolution (Å)	3.0		3.3		3.5	
FSC threshold 0.5						
Map sharpening *B* factor ($Å^2$)	CII	44.6	CII	68	CII	40.8
	CIV	40.3	CIV_2	65.7	CIV_2	44.8
	CV_F_o_stator	43.6	CV_F_o_stator	67.4	CV_F_o_stator	42.6
	CV_$\alpha_3\beta_3$+CS	37.6	CV_$\alpha_3\beta_3$+CS	49.7	CV_$\alpha_3\beta_3\gamma_{top}$	61.7
	CV_*c*-ring+CS_{bottom}	67.2	CV_*c*-ring+CS_{bottom}	365.5	CV_*c*-ring+CS_{bottom}	124.5
	CV_PS	177.3	CV_PS	621.2	CV_PS	347.1
			CV_2_F_o_stator	49.5	CV_2_F_o_stator	43.5
			CV_2_$\alpha_3\beta_3$+CS	55.9	CV_2_$\alpha_3\beta_3$+CS-1	55.1
			CV_2_*c*-ring+CS_{bottom}	103.1	CV_2_*c*-ring-1	375.6
			CV_2_PS	251.8	CV_2_PS-1	284.9
					CV_2_$\alpha_3\beta_3$+CS-2	60
					CV_2_*c*-ring-2	65.5
					CV_2_PS-2	310.1
Model composition						
Non-hydrogen atoms	226455		263928		491392	
Protein residues	27573		32245		94978	
Ligands	140		149		404	
B factors ($Å^2$)						
Protein	103.06		274.14		283.29	
Ligand	55.20		54.86		63.09	
R.m.s. deviations						
Bond lengths (Å)	0.003		0.004		0.002	
Bond angles (°)	0.546		0.523		0.498	
Validation						
MolProbity score	1.71		1.75		1.68	
Clashscore	5.20		5.88		4.39	
Poor rotamers (%)	1.06		0.67		0.00	
Ramachandran plot						
Favored (%)	93.84		93.39		92.63	
Allowed (%)	6.16		6.61		7.37	
Disallowed (%)	0.00		0.00		0.02	

Supplementary Table 2 | Cryo-EM data collection, image processing and model validation of supercomplexes $(CIII_2)_2$, $(CIII_2)_4$ and CII

	$(CIII_2)_2$ (EMDB-67547) (PDB 21BG)	$(CIII_2)_4$ (EMDB-69165) (PDB 23QD)	CII (EMDB-68897) (PDB 23DZ)
Magnification	105,000		
Voltage (kV)	300		
Electron exposure (e–/Å^2)	45.00		
Defocus range (μm)	-0.8 to -2.0		
Pixel size (Å)	1.20		
Symmetry imposed	C1		
Micrographs No.	6,602		24,693
Initial particle No.	1,267,679		4,048,443
Final particle No.	85,890	25,042	223,226
Map resolutions (Å)	$CIII_2$ 2.6	$CIII_2$ 2.8	CII 2.5
FSC threshold 0.143	$CIII_2$ 2.9	$CIII_2$ 3.0	
		$(CIII_2)_2$ 4.3	
Initial models used			
Model resolution (Å)	2.7	3.5	2.5
FSC threshold 0.5			
Map sharpening *B* factor (Å^2)	$CIII_2$ 43.2	$CIII_2$ 21.1	CII 56.2
	$CIII_2$ 38.5	$CIII_2$ 19.1	
		$(CIII_2)_2$ 1.8	
Model composition			
Non-hydrogen atoms	86204	141025	22530
Protein residues	10005	20010	2778
Ligands	84	168	16
B factors (Å^2)			
Protein	43.27	76.58	52.72
Ligand	10.88	18.44	30.58
R.m.s. deviations			
Bond lengths (Å)	0.003	0.004	0.004
Bond angles (°)	0.535	0.583	0.612
Validation			
MolProbity score	1.60	1.93	1.59
Clashscore	4.65	9.92	5.47
Poor rotamers (%)	0.68	0.77	0.80
Ramachandran plot			
Favored (%)	94.76	93.74	95.75
Allowed (%)	5.24	6.24	4.25
Disallowed (%)	0.01	0.02	0.00

Supplementary Table 3 | Model summary of *L. tarentolae* supercomplex CIICIV$_2$CV$_3$

Subunit Name	Uniprot /Gene ID	Annotation	Chain ID	Total residues	Residues built	% built	TMH	Ligands	Lipids
CII									
SDHA	A0A640KIH4	succinate dehydrogenase flavoprotein, putative	SA	607	11-607	98.35%	0	1 × FAD	
SDHB1	A0A640KID5	hypothetical protein, conserved	B1	247	29-245	87.85%	0	1 × Fe_2S_2	
SDHB2	A0A640KIH8	hypothetical protein, conserved	B2	230	48-223	96.52%	0	1 × Fe_3S_4 1 × Fe_4S_4	
SDHC	A0A640KC73	hypothetical protein, conserved	SC	148	50-146	65.54%	3	2 × CoQ_{10}	1 × PC
SDHD1	A0A640KIY5	hypothetical protein, conserved	D1	91	24-91	74.73%	1		
SDHD2	A0A640KQ33	hypothetical protein, conserved	D2	147	60-147	59.86%	2	1 ×HEM	1 × PC
SDHLT3	A0A640KNR8	hypothetical protein, conserved	SE	104	2-104	99.04%	1		1 × PC
SDHLT5	A0A640KMV8	hypothetical protein, conserved	SF	491	11-491	97.96%	0		
SDHLT6	A0A640KEB4	hypothetical protein, conserved	SG	328	38-324	87.50%	0		
SDHLT7	CP119854.1 371026-371775	hypothetical protein, conserved	SH	250	36-250	86.00%	0		
SDHLT8	A0A640KJW8	hypothetical protein, conserved	SI	148	11-144	90.54%	2	1 × CoQ_{10}	
SDHLT9	A0A640KUZ8	hypothetical protein, conserved	SJ	134	10-134	93.28%	1		1 × PC 1 × PE
SDHLT10	A0A640K976	hypothetical protein, conserved	SK	145	33-145	77.93%	1		1 × PC 1 × CDL
SDHLT11	A0A640K8V8	unspecified product	SL	86	10-86	89.53%	1		
CIV$_2$									
COX1	P14544	Cytochrome c oxidase subunit 1	C1, c1	549	1-549	100%	12	1 × heme a 1 × heme a_3 1 × Cu_B 1 × Mg^{2+} 1 × Na^+	2 × PC 1 × CDL

COX2	P14545	Cytochrome c oxidase subunit 2	C2, c2	210	1-210	100%	2	2 × Cu_A	
COX3	Q34935	cytochrome oxidase (kinetoplast)	C3, c3	287	1-285	99.30%	7		3 × PC 2 × PE
COX4	A0A640KP32	cytochrome c oxidase VII, putative	C4, c4	345	182-345	47.54%	1		1 × CDL
COX5B	A0A640KV26	hypothetical protein, conserved	5B, 5b	225	27-225	88.44%	0	1 × FES	
COX5C	A0A640K7Y4	hypothetical protein, conserved	5C, 5c	200	1-200	100%	1		
COX6A	A0A640K9E6	hypothetical protein, conserved	6A, 6a	107	2-107	99.07%	1		1 × PC
COX6B	A0A640KLX8	cytochrome C oxidase subunit VI, putative	6B, 6b	157	2-155	98.09%	0		
COX7A	A0A640KN71	cytochrome c oxidase VIII, putative	7A, 7a	279	151-279	46.24%	1		1 × CDL 1 × PC
COX7C	A0A640K8B8	hypothetical protein, conserved	7C, 7c	147	23-146	84.35%	1		1 × CDL 1 × PE
NDUFA4	A0A640KQ24	hypothetical protein, unknown function	A4, a4	401	159-383	56.11%	1		1 × PC 1 × CDL
COXEG7	A0A640KB61	cytochrome c oxidase subunit IV	4G, 4g	343	33-343	90.67%	0		1 × PC
COXEG8	A0A640KIZ0	cytochrome c oxidase subunit V, putative	4H, 4h	196	18-196	91.33%	0		
COXLT1	A0A640KG51	hypothetical protein, conserved	4A, 4a	118	23-118	81.36%	0		
COXLT2	A0A640KQD4	hypothetical protein, conserved	4B, 4b	116	23-115	80.17%	1		
COXLT3	A0A640KUH3	hypothetical protein, conserved	4C, 4c	106	26-106	76.42%	1		1 × PC
COXLT4	A0A640KXE6	cytochrome c oxidase subunit I	4D, 4d	150	39-147	72.67%	1		
CV									
α	A0A640K8A1	ATPase alpha subunit	VA, vA, 3A	574	34-138/151-428/436-574	90.94%	0	1 × ATP	
	A0A640K8A1	ATPase alpha subunit	VB, vB, 3B	574	34-138/151-428/436-574	90.94%	0	1 × ATP	
	A0A640K8A1	ATPase alpha subunit	VC, vC, 3C	574	34-138/151-428/436-574	90.94%	0	1 × ATP	

β	A0A640KJH9/ A0A640KHL9	ATPase beta subunit, putative	VD, vD, 3D	529	36-520	91.68%	0		
	A0A640KJH9/ A0A640KHL9	ATPase beta subunit, putative	VE, vE, 3E	529	36-520	91.68%	0		
	A0A640KJH9/ A0A640KHL9	ATPase beta subunit, putative	VF, vF, 3F	529	36-520	91.68%	0		
p18	Q25423	Protein P18, mitochondrial	VJ, vJ, 3J	187	22-187	88.77%	0		
	Q25423	Protein P18, mitochondrial	VK, vK, 3K	187	22-187	88.77%	0		
	Q25423	Protein P18, mitochondrial	VN, vN, 3N	187	22-187	88.77%	0		
γ	A0A640KHE2	ATP synthase F1 subunit gamma protein	VG, vG, 3G	303	2-58/65-299	96.37%	0		
δ/ε	A0A640KPL8	ATP synthase, epsilon chain, putative	VH, vH, 3H	181	21-181	88.95%	0		
ε	A0A640KTP4	hypothetical protein, conserved	VI, vI, 3I	73	10-73	87.67%	0		
OSCP/δ	A0A640L1X1	hypothetical protein, conserved	V1, v1, 31	258	18-206/216-258	89.92%	0		
d	CP119832.1 378447-379538	Leishmania tarentolae isolate M2 chromosome 8	Vd, vd, 3d	364	17-319/332-349	88.19%	0		
b	A0A640KSG2	hypothetical protein, conserved	Vp, vp, 3p	104	25-104	76.92%	1		1 × PC 1 × CDL
a	Q33561	MURF4 (kinetoplast)	Va, va, 3a	232	1-232	100%	0		2 × PC 1 × CDL
c/sub 9	CP119848.1 215634-215951	Leishmania tarentolae isolate M2 chromosome 24 Sequence	VO, vO, 3O	106	29-106	73.58%	2		
	CP119848.1 215634-215951	Leishmania tarentolae isolate M2 chromosome 24 Sequence	VP, vP, 3P	106	29-106	73.58%	2		
	CP119848.1 215634-215951	Leishmania tarentolae isolate M2 chromosome 24 Sequence	VQ, vQ, 3Q	106	29-106	73.58%	2		
	CP119848.1 215634-215951	Leishmania tarentolae isolate M2 chromosome 24 Sequence	VR, vR, 3R	106	29-106	73.58%	2		
	CP119848.1 215634-215951	Leishmania tarentolae isolate M2 chromosome 24 Sequence	VS, vS, 3S	106	29-106	73.58%	2		
	CP119848.1 215634-215951	Leishmania tarentolae isolate M2 chromosome 24 Sequence	VT, vT, 3T	106	29-106	73.58%	2		
	CP119848.1 215634-215951	Leishmania tarentolae isolate M2 chromosome 24 Sequence	VU, vU, 3U	106	29-106	73.58%	2		
	CP119848.1 215634-215951	Leishmania tarentolae isolate M2 chromosome 24 Sequence	VV, vV, 3V	106	29-106	73.58%	2		

	CP119848.1 215634-215951	Leishmania tarentolae isolate M2 chromosome 24 Sequence	VW, vW, 3W	106	29-106	73.58%	2		
	CP119848.1 215634-215951	Leishmania tarentolae isolate M2 chromosome 24 Sequence	VX, vX, 3X	106	29-106	73.58%	2		
8/A6L	A0A640KSU1	hypothetical protein, conserved	Vc, vc, 3c	121	38-121	69.42%	1		1 × PC
f	A0A640KHR7	hypothetical protein, conserved	Vf, vf, 3f	145	2-136	93.10%	1		2 × CDL 1 × PC 1 × PE
i/j/6.8pl	A0A640K7R8	hypothetical protein, conserved	Vi, vi, 3i	104	2-104	99.04%	1		1 × PC
k/DAPIT	A0A640KJQ9	hypothetical protein, conserved	Vk, vk, 3k	200	94-200	53.50%	1		1 × CDL
e	A0A640KHE9	hypothetical protein, conserved	3l	147	59-103	30.61%	1		1 × CDL
	A0A640KHE9	hypothetical protein, conserved	VL, vL, 3L	147	58-114	38.78%	1		1 × CDL
g	A0A640KX01	hypothetical protein, conserved	VY, vY	152	25-152	84.21%	1		
g’	A0A640K890	hypothetical protein, conserved	Vm	173	8-159	87.86%	1		1 × PC 1 × PE
g”	A0A640KWP2	hypothetical protein, conserved	VM	273	145-248	38.10%	1		
ATPEG3	A0A640KG00	hypothetical protein, conserved	Vq, vq, 3q	145	62-145	57.93%	0		1 × CDL
ATPEG4	CP119851.1 657310-657490	Leishmania tarentolae isolate M2 chromosome 27Sequence	Vr, vr, 3r	62	1-62	100%	1		1 × PC
ATPLT1	A0A640KLU7	hypothetical protein, conserved	Ve, ve, 3e	398	1-383	96.23%	0		4 × CDL 1 × PC
ATPLT3	A0A640KG49	hypothetical protein, conserved	Vg, vg, 3g	349	83-349	76.50%	0		
ATPLT4	A0A640KVH9	hypothetical protein, conserved	Vh, vh, 3h	160	25-160	85.00%	0		
ATPLT6	A0A640KJ33	hypothetical protein, conserved	Vj, vj, 3j	202	36-201	82.18%	2		1 × PC 1 × CDL
ATPLT11	A0A640KHW7	hypothetical protein, conserved	Vn, vn, 3n	156	18-156	89.10%	1		1 × PC
ATPLT12	A0A640KES0	hypothetical protein, conserved	Vo, vo, 3o	99	6-95	90.91%	0		

Supplementary Table 4 | Model summary of *L. tarentolae* supercomplex ($CIII_2$)$_2$

Subunit Name	Uniprot /Gene ID	Annotation	Chain ID	Total residues	Residues built	% built	TMH	Ligands	Lipids
$CIII_2$									
MPP-alpha	A0A640KGT7	mitochondrial processing peptidase alpha subunit, putative	QB, Qb, qB, qb	527	20-40/56-155/179-383/388-527	88.43%	0		
MPP-beta	A0A640KTP0	mitochondrial processing peptide beta subunit, putative	QA, Qa, qA, qa	490	2-490	99.80%	0		2 × PC 1 × CDL
COB	P14548	Cytochrome b	QC, Qc, qC, qc	371	1-370	99.73%	8	1 × heme b_L 1 × heme b_H 1 × CoQ_{10}	2 × PC 2 × CDL 1 × PE
CYC1	A0A640KA58	cytochrome c1, heme protein, mitochondrial precursor, putative	QD, Qd, qD, qd	258	4-258	98.84%	1	1 × heme c	1 × PE
UQCRFS1	A0A640KYQ2	rieske iron-sulfur protein precursor, putative	QE, Qe, qE, qe	297	18-297	94.28%	1	1 × Fe_2S_2	2 × PC 1 × PE
UQCRH	A0A640KNT3	ubiquinol-cytochrome-c reductase-like protein	QF, Qf, qF, qf	70	4-70	95.71%	0		
UQCRB	A0A640KSC9	hypothetical protein, conserved	QG, Qg, qG, qg	202	10-202	95.54%	0		
UQCRQ	A0A640KRZ1	hypothetical protein, conserved	QH, Qh, qH, qh	119	11-119	91.60%	1		2 × PC
UQCR9	A0A640KF59	hypothetical protein, conserved	QI, Qi, qI, qi	67	3-66	96.97%	1		
UQCR10	A0A640KPN1	hypothetical protein, conserved	QJ, Qj, qJ, qj	147	2-146	98.64%	1		2 × PE
UQCREG1	A0A640KKU7	hypothetical protein, conserved	QK, Qk, qK, qk	85	12-85	87.06%	1		
UQCRLT1	*(Poly-UNK)*	-	QL, Ql, qL, ql	-	-	-	1		
UQCRLT2	*(Poly-UNK)*	-	QM, Qm, qM, qm	-	-	-	0		

Supplementary Table 5 | Cryo-ET data collection and STA processing of $CIICIV_2CV_3$ and CV_4

	$CIICIV_2CV_3$ (EMDB-68795)	CV_4 (EMDB-68796)
Magnification	64,000	
Voltage (kV)	300	
Electron exposure ($e^-/Å^2$)	3.5	
Tilt range	-51° - 51°	
Angular increments	3°	
Tilts per series	35	
Defocus range (μm)	-2.0 to -4.0	
Pixel size (Å)	1.972	
Symmetry imposed	C1	
Tilt series No.	92	
Initial particle No.	114,961	
Final particle No.	2,526	7,143
Map resolutions (Å) FSC threshold 0.143	21	17
Initial models used	SPA-derived 3D model of CV monomer (for template matching)	
Model-map correlations Local CC	0.93	0.91

Supplementary Table 6 | Primers used in this study

Primer name	Sequence
ssu forward primer F3001	GATCTGGTTGATTCTGCCAGTAG
aprt reverse primer A1715	TATTCGTTGTCAGATGGCGCAC
ssu reverse primer F3002	CTGCAGGTTCACCTACAGCTAC
hyg forward primer A3804	CCGATGGCTGTGTAGAAGTACTCG
Insert sequencing forward primer P1442	CCGACTGCAACAAGGTGTAG
Insert sequencing reverse primer A242	CATCTATAGAGAAGTACACGTAAAAG
pLEXSY-EGFP-F	TGCCTTGCCACCAGATCTGCCACCATGGTGAGC
pLEXSY-EGFP-R	GTGATGGTGGTGGGTACCTTACTTGTACAGCTC
swai_F	AAATTGGATAACTTGGCGAA
swai_R	AAATATCGGTGAACTTTCGG

Primers used for the generation and verification of the pLEXSY cell line.

Supplementary Videos

Supplementary Video 1 Cryo-EM SPA maps and models of $CII_2CIV_4CV_{10}$, $CIICIV_2CV_3$ and $CII_2CIV_2CV_2$.

Supplementary Video 2 Cryo-EM SPA maps and models of $(CIII_2)_2$ and $(CIII_2)_4$.

Supplementary Video 3 Cryo-ET tomogram reconstruction and map-backs of subtomogram averages.

Supplementary Video 4 Subtomogram averages and docking of the cryo-EM structures.

References

1. Evans, D. A. In vitro cultivation and biological cloning of Leishmania. *Methods in molecular biology (Clifton, N.J.)* **21**, 29–41 (1993).
2. Durrieu-Gaillard, S., Sissler, M. & Hashem, Y. Purification of Mitochondrial Ribosomal Complexes from Trypanosoma cruzi and Leishmania tarentolae for Cryo-EM Analysis. *Bio-protocol* **12**, e4425 (2022).
3. de Oliveira Filho, V. A., Garcia, M. S. A., Rosa, L. B., Giorgio, S. & Miguel, D. C. An Overview of Leishmania In Vitro Cultivation and Implications for Antileishmanial Screenings against Promastigotes. *Parasitologia* **4**, 305–318 (2024).
4. Niemann, M. & Schneider, A. A Scalable Purification Method for Mitochondria from Trypanosoma brucei. *Methods in molecular biology (Clifton, N.J.)* **2116**, 611–626 (2020).
5. de Oliveira, T. A., Silva, W. da, da Rocha Torres, N., Badaró de Moraes, J. V., Senra, R. L., de Oliveira Mendes, T. A., Júnior, A. S., Bressan, G. C. & Fietto, J. L. R. Application of the LEXSY Leishmania tarentolae system as a recombinant protein expression platform: A review. *Process Biochemistry* **87**, 164–173 (2019).
6. Sugino, M. & Niimi, T. Expression of Multisubunit Proteins in Leishmania tarentolae. in *Recombinant Gene Expression* vol. 267 317–325 (Humana Press, New Jersey, 2012).
7. Kalef, D. A. Leishmania mexicana recombinant filamentous acid phosphatase as carrier for Toxoplasma gondii surface antigen 1 expression in Leishmania tarentolae. *Journal of parasitic diseases : official organ of the Indian Society for Parasitology* **45**, 1135–1144 (2021).
8. Goes, W. M., Brasil, C. R. F., Reis-Cunha, J. L., Coqueiro-Dos-Santos, A., Grazielle-Silva, V., de Souza Reis, J., Souto, T. C., Laranjeira-Silva, M. F., Bartholomeu, D. C., Fernandes, A. P. & Teixeira, S. M. R. Complete assembly, annotation of virulence genes and CRISPR editing of the genome of Leishmania amazonensis PH8 strain. *Genomics* **115**, 110661 (2023).
9. Brischigliaro, M., Frigo, E., Fernandez-Vizarra, E., Bernardi, P. & Viscomi, C. Measurement of mitochondrial respiratory chain enzymatic activities in Drosophila melanogaster samples. *STAR protocols* **3**, 101322 (2022).

10. Miyadera, H., Shiomi, K., Ui, H., Yamaguchi, Y., Masuma, R., Tomoda, H., Miyoshi, H., Osanai, A., Kita, K. & Omura, S. Atpenins, potent and specific inhibitors of mitochondrial complex II (succinate-ubiquinone oxidoreductase). *Proceedings of the National Academy of Sciences of the United States of America* **100**, 473–7 (2003).
11. Kiianitsa, K., Solinger, J. A. & Heyer, W.-D. NADH-coupled microplate photometric assay for kinetic studies of ATP-hydrolyzing enzymes with low and high specific activities. *Analytical biochemistry* **321**, 266–71 (2003).
12. Punjani, A., Rubinstein, J. L., Fleet, D. J. & Brubaker, M. A. cryoSPARC: algorithms for rapid unsupervised cryo-EM structure determination. *Nature methods* **14**, 290–296 (2017).
13. Punjani, A., Zhang, H. & Fleet, D. J. Non-uniform refinement: adaptive regularization improves single-particle cryo-EM reconstruction. *Nature methods* **17**, 1214–1221 (2020).
14. Zivanov, J., Nakane, T. & Scheres, S. H. W. Estimation of high-order aberrations and anisotropic magnification from cryo-EM data sets in RELION-3.1. *IUCrJ* **7**, 253–267 (2020).
15. Rubinstein, J. L. & Brubaker, M. A. Alignment of cryo-EM movies of individual particles by optimization of image translations. *Journal of structural biology* **192**, 188–95 (2015).
16. Liebschner, D. *et al.* Macromolecular structure determination using X-rays, neutrons and electrons: recent developments in Phenix. *Acta crystallographica. Section D, Structural biology* **75**, 861–877 (2019).
17. Liu, Y.-T., Fan, H., Hu, J. J. & Zhou, Z. H. Overcoming the preferred-orientation problem in cryo-EM with self-supervised deep learning. *Nature methods* **22**, 113–123 (2025).
18. Kimanius, D., Dong, L., Sharov, G., Nakane, T. & Scheres, S. H. W. New tools for automated cryo-EM single-particle analysis in RELION-4.0. *The Biochemical journal* **478**, 4169–4185 (2021).
19. Rosenthal, P. B. & Henderson, R. Optimal determination of particle orientation, absolute hand, and contrast loss in single-particle electron cryomicroscopy. *Journal of molecular*

biology **333**, 721–45 (2003).

20. Emsley, P., Lohkamp, B., Scott, W. G. & Cowtan, K. Features and development of Coot. *Acta crystallographica. Section D, Biological crystallography* **66**, 486–501 (2010).

21. Goddard, T. D., Huang, C. C., Meng, E. C., Pettersen, E. F., Couch, G. S., Morris, J. H. & Ferrin, T. E. UCSF ChimeraX: Meeting modern challenges in visualization and analysis. *Protein science : a publication of the Protein Society* **27**, 14–25 (2018).

22. Pettersen, E. F., Goddard, T. D., Huang, C. C., Meng, E. C., Couch, G. S., Croll, T. I., Morris, J. H. & Ferrin, T. E. UCSF ChimeraX: Structure visualization for researchers, educators, and developers. *Protein science : a publication of the Protein Society* **30**, 70–82 (2021).

23. Meng, E. C., Goddard, T. D., Pettersen, E. F., Couch, G. S., Pearson, Z. J., Morris, J. H. & Ferrin, T. E. UCSF ChimeraX: Tools for structure building and analysis. *Protein science : a publication of the Protein Society* **32**, e4792 (2023).

24. Sun, F., Huo, X., Zhai, Y., Wang, A., Xu, J., Su, D., Bartlam, M. & Rao, Z. Crystal structure of mitochondrial respiratory membrane protein complex II. *Cell* **121**, 1043–57 (2005).

25. Mühleip, A., Flygaard, R. K., Baradaran, R., Haapanen, O., Gruhl, T., Tobiasson, V., Maréchal, A., Sharma, V. & Amunts, A. Structural basis of mitochondrial membrane bending by the I-II-III2-IV2 supercomplex. *Nature* **615**, 934–938 (2023).

26. He, Z., Wu, M., Tian, H., Wang, L., Hu, Y., Han, F., Zhou, J., Wang, Y. & Zhou, L. Euglena's atypical respiratory chain adapts to the discoidal cristae and flexible metabolism. *Nature communications* **15**, 1628 (2024).

27. Gahura, O., Mühleip, A., Hierro-Yap, C., Panicucci, B., Jain, M., Hollaus, D., Slapničková, M., Zíková, A. & Amunts, A. An ancestral interaction module promotes oligomerization in divergent mitochondrial ATP synthases. *Nature communications* **13**, 5989 (2022).

28. Ho, C.-M., Li, X., Lai, M., Terwilliger, T. C., Beck, J. R., Wohlschlegel, J., Goldberg, D. E., Fitzpatrick, A. W. P. & Zhou, Z. H. Bottom-up structural proteomics: cryoEM of protein complexes enriched from the cellular milieu. *Nature methods* **17**, 79–85 (2020).

29. Goto, Y., Kuroki, A., Suzuki, K. & Yamagishi, J. Draft Genome Sequence of Leishmania

tarentolae Parrot Tar II, Obtained by Single-Molecule Real-Time Sequencing. *Microbiology resource announcements* **9**, 4–5 (2020).

30. Shanmugasundram, A., Starns, D., Böhme, U., Amos, B., Wilkinson, P. A., Harb, O. S., Warrenfeltz, S., Kissinger, J. C., McDowell, M. A., Roos, D. S., Crouch, K. & Jones, A. R. TriTrypDB: An integrated functional genomics resource for kinetoplastida. *PLoS neglected tropical diseases* **17**, e0011058 (2023).

31. Aslett, M. *et al.* TriTrypDB: a functional genomic resource for the Trypanosomatidae. *Nucleic acids research* **38**, D457-62 (2010).

32. Afonine, P. V., Grosse-Kunstleve, R. W., Echols, N., Headd, J. J., Moriarty, N. W., Mustyakimov, M., Terwilliger, T. C., Urzhumtsev, A., Zwart, P. H. & Adams, P. D. Towards automated crystallographic structure refinement with phenix.refine. *Acta crystallographica. Section D, Biological crystallography* **68**, 352–67 (2012).

33. Afonine, P. V., Poon, B. K., Read, R. J., Sobolev, O. V., Terwilliger, T. C., Urzhumtsev, A. & Adams, P. D. Real-space refinement in PHENIX for cryo-EM and crystallography. *Acta crystallographica. Section D, Structural biology* **74**, 531–544 (2018).

34. Abramson, J. *et al.* Accurate structure prediction of biomolecular interactions with AlphaFold 3. *Nature* **630**, 493–500 (2024).

35. Williams, C. J., Headd, J. J., Moriarty, N. W., Prisant, M. G., Videau, L. L., Deis, L. N., Verma, V., Keedy, D. A., Hintze, B. J., Chen, V. B., Jain, S., Lewis, S. M., Arendall, W. B., Snoeyink, J., Adams, P. D., Lovell, S. C., Richardson, J. S. & Richardson, D. C. MolProbity: More and better reference data for improved all-atom structure validation. *Protein science : a publication of the Protein Society* **27**, 293–315 (2018).

36. Wang, C., Ma, C., Xu, Y., Chang, S., Wu, H., Yan, C., Chen, J., Wu, Y., An, S., Xu, J., Han, Q., Jiang, Y., Jiang, Z., Chu, X., Gao, H., Zhang, X. & Chang, Y. Dynamics of the mammalian pyruvate dehydrogenase complex revealed by in-situ structural analysis. *Nature communications* **16**, 917 (2025).

37. Hagen, W. J. H., Wan, W. & Briggs, J. A. G. Implementation of a cryo-electron tomography tilt-scheme optimized for high resolution subtomogram averaging. *Journal of structural biology* **197**, 191–198 (2017).

38. Tegunov, D. & Cramer, P. Real-time cryo-electron microscopy data preprocessing with

Warp. *Nature methods* **16**, 1146–1152 (2019).

39. Chen, M., Dai, W., Sun, S. Y., Jonasch, D., He, C. Y., Schmid, M. F., Chiu, W. & Ludtke, S. J. Convolutional neural networks for automated annotation of cellular cryo-electron tomograms. *Nature methods* **14**, 983–985 (2017).

40. Burt, A., Toader, B., Warshamanage, R., von Kügelgen, A., Pyle, E., Zivanov, J., Kimanius, D., Bharat, T. A. M. & Scheres, S. H. W. An image processing pipeline for electron cryo-tomography in RELION-5. *FEBS open bio* **14**, 1788–1804 (2024).

41. Chaillet, M. L., Roet, S., Veltkamp, R. C. & Förster, F. pytom-match-pick: A tophat-transform constraint for automated classification in template matching. *Journal of structural biology: X* **11**, 100125 (2025).

42. Tegunov, D., Xue, L., Dienemann, C., Cramer, P. & Mahamid, J. Multi-particle cryo-EM refinement with M visualizes ribosome-antibiotic complex at 3.5 Å in cells. *Nature methods* **18**, 186–193 (2021).

43. Roth, P., Ermel, U. H., Moser, D., Arctaedius, G., Wehrheim, M., Scheffer, M. P. & Frangakis, A. S. ArtiaX: geometric models, camera paths and image processing tools. *Journal of structural biology* **217**, 108215 (2025).

44. Lamm, L., Righetto, R. D., Wietrzynski, W., Pöge, M., Martinez-Sanchez, A., Peng, T. & Engel, B. D. MemBrain: A deep learning-aided pipeline for detection of membrane proteins in Cryo-electron tomograms. *Computer methods and programs in biomedicine* **224**, 106990 (2022).

45. Lamm, L., Zufferey, S., Zhang, H., Righetto, R. D., Waltz, F., Wietrzynski, W., Yamauchi, K. A., Burt, A., Liu, Y., Martinez-Sanchez, A., Ziegler, S., Isensee, F., Schnabel, J. A., Engel, B. D. & Peng, T. MemBrain v2: an end-to-end tool for the analysis of membranes in cryo-electron tomography. *BioRxiv* at https://doi.org/10.1101/2024.01.05.574336 (2024).

46. Salfer, M., Collado, J. F., Baumeister, W., Fernández-Busnadiego, R. & Martínez-Sánchez, A. Reliable estimation of membrane curvature for cryo-electron tomography. *PLoS computational biology* **16**, e1007962 (2020).

47. Barad, B. A., Medina, M., Fuentes, D., Wiseman, R. L. & Grotjahn, D. A. Quantifying organellar ultrastructure in cryo-electron tomography using a surface morphometrics

pipeline. *The Journal of cell biology* **222**, (2023).

48. Morales, J., Mogi, T., Mineki, S., Takashima, E., Mineki, R., Hirawake, H., Sakamoto, K., Omura, S. & Kita, K. Novel mitochondrial complex II isolated from Trypanosoma cruzi is composed of 12 peptides including a heterodimeric Ip subunit. *The Journal of biological chemistry* **284**, 7255–63 (2009).

49. Han, F., Hu, Y., Wu, M., He, Z., Tian, H. & Zhou, L. Structures of Tetrahymena thermophila respiratory megacomplexes on the tubular mitochondrial cristae. *Nature communications* **14**, 2542 (2023).

50. Wú, F., Mühleip, A., Gruhl, T., Sheiner, L., Maréchal, A. & Amunts, A. Structure of the II2-III2-IV2 mitochondrial supercomplex from the parasite Perkinsus marinus. at https://doi.org/10.1101/2024.05.25.595893 (2024).

51. Du, Z. *et al.* Structure of the human respiratory complex II. *Proceedings of the National Academy of Sciences of the United States of America* **120**, e2216713120 (2023).

52. Huang, L., Sun, G., Cobessi, D., Wang, A. C., Shen, J. T., Tung, E. Y., Anderson, V. E. & Berry, E. A. 3-nitropropionic acid is a suicide inhibitor of mitochondrial respiration that, upon oxidation by complex II, forms a covalent adduct with a catalytic base arginine in the active site of the enzyme. *The Journal of biological chemistry* **281**, 5965–72 (2006).

53. Huang, L., Shen, J. T., Wang, A. C. & Berry, E. A. Crystallographic studies of the binding of ligands to the dicarboxylate site of Complex II, and the identity of the ligand in the 'oxaloacetate-inhibited' state. *Biochimica et biophysica acta* **1757**, 1073–83 (2006).

54. Li, Z.-W., Huang, Y.-H., Wei, G., Lu, Z.-W., Wang, Y.-X., Cui, G.-R., Wang, J.-Y., Yu, X.-H., Fu, Y.-X., Fan, E.-D., Wu, Q.-Y., Zhu, X.-L., Ye, Y. & Yang, G.-F. Cryo-EM structure of the yeast Saccharomyces cerevisiae SDH provides a template for eco-friendly fungicide discovery. *Nature communications* **16**, 8936 (2025).

55. Haapanen, O., Djurabekova, A. & Sharma, V. Role of Second Quinone Binding Site in Proton Pumping by Respiratory Complex I. *Frontiers in chemistry* **7**, 221 (2019).

56. Zhou, Q., Zhai, Y., Lou, J., Liu, M., Pang, X. & Sun, F. Thiabendazole inhibits ubiquinone reduction activity of mitochondrial respiratory complex II via a water molecule mediated binding feature. *Protein & cell* **2**, 531–42 (2011).

57. Huang, L.-S., Lümmen, P. & Berry, E. A. Crystallographic investigation of the ubiquinone binding site of respiratory Complex II and its inhibitors. *Biochimica et biophysica acta. Proteins and proteomics* **1869**, 140679 (2021).

58. Mühleip, A., McComas, S. E. & Amunts, A. Structure of a mitochondrial ATP synthase with bound native cardiolipin. *eLife* **8**, 1–23 (2019).

59. Guo, H., Bueler, S. A. & Rubinstein, J. L. Atomic model for the dimeric FO region of mitochondrial ATP synthase. *Science* **358**, 936–940 (2017).

60. Gu, J., Zhang, L., Zong, S., Guo, R., Liu, T., Yi, J., Wang, P., Zhuo, W. & Yang, M. Cryo-EM structure of the mammalian ATP synthase tetramer bound with inhibitory protein IF1. *Science (New York, N.Y.)* **364**, 1068–1075 (2019).

61. Flygaard, R. K., Mühleip, A., Tobiasson, V. & Amunts, A. Type III ATP synthase is a symmetry-deviated dimer that induces membrane curvature through tetramerization. *Nature communications* **11**, 5342 (2020).

62. Murphy, B. J., Klusch, N., Langer, J., Mills, D. J., Yildiz, Ö. & Kühlbrandt, W. Rotary substates of mitochondrial ATP synthase reveal the basis of flexible F1-Fo coupling. *Science (New York, N.Y.)* **364**, 543108 (2019).

63. Dietrich, L., Agip, A.-N. A., Kunz, C., Schwarz, A. & Kühlbrandt, W. In situ structure and rotary states of mitochondrial ATP synthase in whole Polytomella cells. *Science (New York, N.Y.)* **385**, 1086–1090 (2024).

64. Marko, M., Hsieh, C., Schalek, R., Frank, J. & Mannella, C. Focused-ion-beam thinning of frozen-hydrated biological specimens for cryo-electron microscopy. *Nature methods* **4**, 215–7 (2007).

65. Rigort, A., Bäuerlein, F. J. B., Villa, E., Eibauer, M., Laugks, T., Baumeister, W. & Plitzko, J. M. Focused ion beam micromachining of eukaryotic cells for cryoelectron tomography. *Proceedings of the National Academy of Sciences of the United States of America* **109**, 4449–54 (2012).

66. Zhang, L., Guo, R., Xiao, C., Li, J., Gu, J. & Yang, M. Structural basis for the regulatory mechanism of mammalian mitochondrial respiratory chain megacomplex-I2III2IV2. *hLife* **2**, 189–200 (2024).

67. Guo, R., Zong, S., Wu, M., Gu, J. & Yang, M. Architecture of Human Mitochondrial

Respiratory Megacomplex I2III2IV2. *Cell* **170**, 1247-1257.e12 (2017).

68. Blum, T. B., Davies, K. M. & Kühlbrandt, W. Subtomogram averages of mitochondrial ATP synthase dimers from plants show a conserved extra density at the peripheral stalk. *IUCrJ* **12**, 563–569 (2025).

69. Mühleip, A., Kock Flygaard, R., Ovciarikova, J., Lacombe, A., Fernandes, P., Sheiner, L. & Amunts, A. ATP synthase hexamer assemblies shape cristae of Toxoplasma mitochondria. *Nature communications* **12**, 120 (2021).

70. MacLean, A. E., Shikha, S., Ferreira Silva, M., Gramelspacher, M. J., Nilsen, A., Liebman, K. M., Pou, S., Winter, R. W., Meir, A., Riscoe, M. K., Doggett, J. S., Sheiner, L. & Mühleip, A. Structure, assembly and inhibition of the Toxoplasma gondii respiratory chain supercomplex. *Nature structural & molecular biology* **32**, 1424–1433 (2025).

71. Davies, K. M., Daum, B., Gold, V. A. M., Mühleip, A. W., Brandt, T., Blum, T. B., Mills, D. J. & Kühlbrandt, W. Visualization of ATP synthase dimers in mitochondria by electron cryo-tomography. *Journal of visualized experiments : JoVE* 51228 (2014) doi:10.3791/51228.

72. Strauss, M., Hofhaus, G., Schröder, R. R. & Kühlbrandt, W. Dimer ribbons of ATP synthase shape the inner mitochondrial membrane. *The EMBO journal* **27**, 1154–60 (2008).

73. Davies, K. M., Strauss, M., Daum, B., Kief, J. H., Osiewacz, H. D., Rycovska, A., Zickermann, V. & Kühlbrandt, W. Macromolecular organization of ATP synthase and complex I in whole mitochondria. *Proceedings of the National Academy of Sciences of the United States of America* **108**, 14121–6 (2011).

74. Davies, K. M., Anselmi, C., Wittig, I., Faraldo-Gómez, J. D. & Kühlbrandt, W. Structure of the yeast F1Fo-ATP synthase dimer and its role in shaping the mitochondrial cristae. *Proceedings of the National Academy of Sciences of the United States of America* **109**, 13602–7 (2012).

75. Mühleip, A. W., Joos, F., Wigge, C., Frangakis, A. S., Kühlbrandt, W. & Davies, K. M. Helical arrays of U-shaped ATP synthase dimers form tubular cristae in ciliate mitochondria. *Proceedings of the National Academy of Sciences of the United States of*

America **113**, 8442–7 (2016).

76. Mühleip, A. W., Dewar, C. E., Schnaufer, A., Kühlbrandt, W. & Davies, K. M. In situ structure of trypanosomal ATP synthase dimer reveals a unique arrangement of catalytic subunits. *Proceedings of the National Academy of Sciences of the United States of America* **114**, 992–997 (2017).

77. Blum, T. B., Hahn, A., Meier, T., Davies, K. M. & Kühlbrandt, W. Dimers of mitochondrial ATP synthase induce membrane curvature and self-assemble into rows. *Proceedings of the National Academy of Sciences of the United States of America* **116**, 4250–4255 (2019).

78. Zheng, W., Chai, P., Zhu, J. & Zhang, K. High-resolution in situ structures of mammalian respiratory supercomplexes. *Nature* **631**, 232–239 (2024).

79. Waltz, F., Righetto, R. D., Lamm, L., Salinas-Giegé, T., Kelley, R., Zhang, X., Obr, M., Khavnekar, S., Kotecha, A. & Engel, B. D. In-cell architecture of the mitochondrial respiratory chain. *Science (New York, N.Y.)* **387**, 1296–1301 (2025).

80. Nakano, A., Masuya, T., Akisada, S., Ishikawa-Fukuda, M., Mitsuoka, K., Miyoshi, H., Murai, M. & Yokoyama, K. In situ structure determination of Respiratory Supercomplexes and ATP synthase oligomers in mammalian mitochondrial inner membrane. *biorixv* at https://doi.org/10.1101/2025.09.19.677273 (2025).

81. Nesterov, S., Chesnokov, Y., Kamyshinsky, R., Panteleeva, A., Lyamzaev, K., Vasilov, R. & Yaguzhinsky, L. Ordered Clusters of the Complete Oxidative Phosphorylation System in Cardiac Mitochondria. *International journal of molecular sciences* **22**, 1–10 (2021).

82. Pánek, T., Eliáš, M., Vancová, M., Lukeš, J. & Hashimi, H. Returning to the Fold for Lessons in Mitochondrial Crista Diversity and Evolution. *Current biology : CB* **30**, R575–R588 (2020).